9-2012

Dynamics and Kinetics of Model Biological Systems

Stephen William Mirigian
University of Massachusetts Amherst, mirigian@mail.pse.umass.edu

DYNAMICS AND KINETICS OF MODEL BIOLOGICAL SYSTEMS

A Dissertation Presented

by

STEPHEN MIRIGIAN

Submitted to the Graduate School of the
University of Massachusetts Amherst in partial fulfillment
of the requirements for the degree of

DOCTOR OF PHILOSOPHY

September 2012

Polymer Science and Engineering

DYNAMICS AND KINETICS OF MODEL BIOLOGICAL SYSTEMS

A Dissertation Presented

by

STEPHEN MIRIGIAN

Approved as to style and content by:

Murugappan Muthukumar, Chair

V. Adrian Parsegian, Member

Gregory Grason, Member

David Hoagland, Department Chair

Polymer Science and Engineering

to Mom

ACKNOWLEDGMENTS

I would begin by extended my heartfelt thanks to my advisor, Murugappan Muthukumar, for his tremendous support of me throughout the creation of this work. His enthusiasm and depth of knowledge are infectious and inspiring and it is only with his help that this work was possible. I count attending his lectures on the theory of polymer physics as some of the greatest pleasures of my time here in Amherst. I would also like to extend thanks to Professor V. Adrian Parsegian and Professor Greg Grason for their valuable criticism and time spent serving on my thesis committee. It has been a pleasure to know them personally as well as to work under them. I am especially grateful to all the members of my committe for their unflagging faith in my ability to do good science, even when I was doubtful of myself. Their encouragement and insistence on excellence has been their most valuable service to me.

This section would not be complete without acknowledging the many friends I have made during my time spent in the Polymer Science department. Specifically I would like to name many group members, both past an present. Jo Pool, who first

introduced me to Dr. Muthukumar and brought me into the department. Rajeev Kumar and Arindam Kundagrami for helpful discussions in working through many detailed technical points when I was just starting out. Mithun Mitra and Buddho Chakrabarti for many stimulating intellectual discussions. Ben Mohr for his wonderful friendship and willingness to ponder the big questions in life. Sveta Morozova for ensuring I was well fed, rested, and cared for during the writing of this thesis. There are many others as well, whom space prevents me from personally ackowledging.

My time in Amherst has been blessed beyond any reasonable expectation by my church family at Mercyhouse. There are too many of you to name and I will surely leave some out, but I thank specifically Robert and Mel, Nate and Sarah, Martin, Rob, Patrick, Lois, Bill and Val, Tom and Jennifer, Josh and Felicia, Abbie, Amanda, Cindy, Dan and Sarah, Patrick, Austin and Sarah, John, Matt, Brett and Jenna, Josh, Tommy, Jenny and Cory, and many others.

Finally I want to thank my family for their love and encouragement. My parents, for teaching me who Jesus is and that we can know him. My mother for the quiet and calming presence she gave me. My father, for making me who I am in nearly every conceivable way, and my brother for always being my closest ally.

I feel tremendously blessed to have the opportunity to study physics and play in the creation that God has made. It is a thing of great beauty and wonder.

ABSTRACT

DYNAMICS AND KINETICS OF MODEL BIOLOGICAL SYSTEMS

SEPTEMBER 2012

STEPHEN MIRIGIAN

B.S., UNIVERSITY OF MASSACHUSETTS - AMHERST

Ph.D., UNIVERSITY OF MASSACHUSETTS AMHERST

Directed by: Professor Murugappan Muthukumar

In this work we study three systems of biological interest: the translocation of a heterogeneously charged polymer through an infinitely thin pore, the wrapped of a rigid particle by a soft vesicle and the modification of the dynamical properties of a gel due to the presence of rigid inclusions.

We study the kinetics of translocation for a heterogeneously charged polyelectrolyte through an infinitely narrow pore using the Fokker-Planck formalism to com-

pute mean first passage times, the probability of successful translocation, and the mean successful translocation time for a diblock copolymer. We find, in contrast to the homopolymer result, that details of the boundary conditions lead to qualitatively different behavior. Under experimentally relevant conditions for a diblock copolymer we find that there is a threshold length of the charged block, beyond which the probability of successful translocation is independent of charge fraction. Additionally, we find that mean successful translocation time exhibits non-monotonic behavior with increasing length of the charged fraction; there is an optimum length of the charged block where the mean successful translocation time is slowest and there can be a substantial range of charge fraction where it is slower than a minimally charged chain. For a fixed total charge on the chain, we find that finer distributions of the charge along the chain leads to a significant reduction in mean translocation time compared to the diblock distribution.

Endocytosis is modeled using a simple geometrical model from the literature. We map the process of wrapping a rigid spherical bead onto a one-dimensional stochastic process described by the Fokker-Planck equation to compute uptake rates as a function of membrane properties and system geometry. We find that simple geometrical

considerations pick an optimal particle size for uptake and a corresponding maximal uptake rate, which can be controlled by altering the material properties of the membrane.

Finally, we use a mean field approximation, neglecting correlations among the embedded particles, to examine the effect of inclusions in a viscoelastic medium on the effective macroscopic properties of the gel. We find an essentially linear dependence of both components of the complex shear modulus up to arbitrary volume fractions of the inclusions, in contradiction to experimental observations. We conclude that the incorporation of correlations among the particles is needed in order to explain experiments, in analogy with the elastic case.

TABLE OF CONTENTS

Page

LIST OF TABLES

Table **Page**

LIST OF FIGURES

Figure **Page**

CHAPTER 1

TRANSLOCATION OF A HETEROGENEOUS POLYMER

1.1 Introduction

The movement of a linear, flexible polymer through a small channel is a phenomenon of fundamental interest in biology as well as having significant potential for technological applications. Experimental work by Kasianowicz and coworkers[2] and Bezrukov and coworkers[3] demonstrated the feasibility of monitoring single molecule translocation with ionic currents. Subsequent work has refined this technique in the context of both biological[4, 5, 6, 7, 8, 9, 10] and synthetic nanopores[11, 12, 13, 14, 15, 16, 17], revealing a rich dependence of translocation behavior on many factors such as the tertiary structures of the polymer[18, 19, 20, 8, 21, 17], salt concentration[22, 23], field strength[16], and pH[24, 10]. The experimental literature in this field continues to expand rapidly[25].

The complex phenomenology of polymer translocation has attracted significant theoretical work[25, 26, 27, 28, 29, 30, 31, 32, 33, 34, 35, 36, 37, 38, 39, 40, 41, 42]. By assuming that the ends of the chain are in equilibrium throughout the translocation process, the large number of degrees of freedom of the polymer can be captured by a one dimensional free energy landscape, thereby mapping the process of translocation to a one dimensional diffusion process along the length of the chain[26, 27, 28]. The local nature of the interaction between the chain and the pore is usually accounted for by a kinetic parameter[28, 29] in order to correctly capture experimentally observed scaling behavior. The basic assumption in this free energy landscape picture is that the translocation time is long enough to allow equilibration of chain conformations at all stages of the translocation process. If this condition is not satisfied, nonlinear effects on the translocation kinetics set in[30, 31].

In efforts to address nonuniversal features of polymer translocation, subsequent computational and theoretical work has sought to capture the effects of details of the pore geometry[32, 33], interactions between the chain and pore/membrane[32, 34, 35], and heterogeneities along the chain[36, 37, 38]. Such heterogeneous systems have been studied using a variety of computational techniques, notably via 2-D Langevin

dynamics simulation by Luo and coworkers[39] and via Monte Carlo and numerical methods by Gauthier and Slater[40, 41, 42] and Slutsky and coworkers[34]. Interest in heterogeneous chains has been intensified due to interest in methods to obtain additional control over the process of translocation[43, 44, 45, 46] by a variety of means. One possibility of particular interest in this paper is to manipulate the kinetics of translocation of a charged molecule via the addition of an uncharged tag[47, 43] or a tag with differing chemical potential driving force across the pore[48, 49]. The resulting system is then modeled as the translocation of a partially charged diblock copolymer across the entropic barrier of the pore. Here we use exact analytic methods based on the theory of Muthukumar[28, 50] within the model pictured in Fig. 1.1, to study the kinetics and success rates of translocation for a heterogeneously charged polymer. We also use these theoretical techniques to explore the kinetic behavior of the sequences shown in Fig. 1.2.

Previous theoretical calculations[50, 36] of the translocation kinetics for a homopolymer have predicted qualitatively similar behavior whether, once having overcome the nucleation barrier, the chain is allowed to retract unsuccessfully back to the *cis* chamber or whether such a motion is forbidden. Theoretical studies of hetero-

geneous systems by Muthukumar[32] and Mohan and coworkers[37] have made the assumption that the chain is forbidden from retracting back into the *cis* chamber. We find that for non-uniformly charged chains such considerations lead to significantly different qualitative predictions of the translocation behavior as a function of the total charge on the chain. As discussed below, in the theory there are two conditions corresponding to absorbing/absorbing boundary conditions and reflecting/absorbing boundary conditions on the chain. The words "reflecting" and "absorbing" refer to the behavior of the monomers on either end of the chain. If the end monomer is able to pass through the pore it is "absorbed" by the pore; if it cannot pass through the pore but is pushed back into the chamber where it came from, it is "reflected" by the pore. Absorbing/absorbing boundary conditions are physically natural in both experiment and simulation. A reflecting/absorbing boundary condition often allows for computational convenience in theoretical calculation as well as allowing for more efficient simulation. The effects of differing boundary conditions will be studied primarily for a diblock copolymer consisting of one block of charged monomers and a second block of uncharged monomers.

The role of charge distribution along the chain backbone is studied by fixing the total charge and varying the placement of charged monomers according to figure 1.2. The sequences have been ordered according to the total number of blocked monomers along the backbone. Thus, sequence 1 is a diblock with 2 blocks of monomers, one charged block and one uncharged block. Similarly, sequence 11 is a multiblock with seven blocks of monomers, four charged blocks and three uncharged blocks.

We have organized the remainder of the chapter as follows: in section 1.2 we define our theoretical model, giving relevant parameter values and assumptions. In section 2.3 we give results for these models, with comparison between theory and simulation. Simulation data is due to Wang[1]. In light of the issues outlined above, we organize our results according to the relevant boundary conditions. Thus, we first discuss translocation for systems experiencing with a reflecting/absorbing boundary condition. Within this context we explore the effect of charge distribution along the backbone. We then impose the more physically natural absorbing/absorbing boundary conditions and focus on a simple diblock copolymer with one leading block of charged monomers and a second block of uncharged monomers. We calculate the probability of successful translocation, the average time for successful translocation,

and the average dwell time of such a chain in the pore as functions of field strength and length of the charged block. Unexpectedly, we find that there is an finite optimum length of the charged block where the mean translocation time will be slowest. Finally, we close with brief concluding remarks in section 1.4.

1.2 Model

1.2.0.1 Free Energy Landscape

Theoretically, we consider a long heterogeneous polymer of length N moving through an infinitely thin pore as shown in figure 1.1. The polymer is driven through the pore by an electrochemical gradient, which the m^{th} monomer experiences as $\mu_m = \mu'_{m,trans} - \mu'_{m,cis}$. Uncharged monomers will have $\mu_m = 0$. Borrowing standard results from the theory of random walks[51], a chain of n segments in a half space will have $Z_n = e^{-\mu n} n^{\gamma-1}$ possible configurations, where γ is a critical exponent describing the quality of the solvent. For theta solvent, $\gamma = 0.5$; electrolyte solutions give $\gamma \approx 0.69$ at high salt and $\gamma = 1$ at low salt. We may use this result to write the free energy of one section of the chain in one compartment as

$$\frac{F_n}{k_B T} = (1-\gamma)\ln n + \sum_i \mu'_i \,, \tag{1.1}$$

where μ_i' is the chemical potential of the monomer in the solution. Considering figure 1.1, it is clear that when m monomers are in the *trans* chamber the free energy of the entire chain is given by the sum of the two half chains on either side of the pore[28]

$$F_m = (1 - \gamma_{trans}) \ln m + (1 - \gamma_{cis}) \ln(N - m) + \sum_i^m \mu_i \,. \tag{1.2}$$

Free energy and chemical potential are in units of $k_B T$. Here μ_i has the meaning of a chemical potential *difference* for the i^{th} monomer moving from the *cis* to the *trans* chamber as defined above. The logarithmic terms in equation (1.2) give rise to an entropic barrier for translocation such that a critical number of monomers, m^*, must nucleate into the *trans* chamber before translocation becomes a downhill process. The number of monomers corresponding to the nucleation barrier is given by $\partial_m F_m = 0$. Even for modest driving potentials of $1 k_B T (\sim 25 mV)$, this gives m^* on the order of a single monomer. Therefore, the kinetics in overcoming this barrier are not significantly affected by the distribution of charges along the chain, provided that the initial monomer into the pore is charged. We refer the reader to previous work[50] regarding the homopolymer problem for details.

Using the free energy landscape of equation (1.2) we make a familiar mapping of the translocation process onto a one-dimensional random walk problem[28], controlled by the Fokker-Planck equation

$$\frac{\partial}{\partial t}W_m(t) = \frac{\partial}{\partial m}\left[\frac{k_m}{k_BT}\frac{\partial F_m}{\partial m}W_m(t) + \frac{\partial}{\partial m}k_m W_m(t)\right]. \tag{1.3}$$

In making this mapping, we assume that the translocation kinetics are slow enough that the chain is in equilibrium throughout the process. Here $W_m(t)$ is the probability of m monomers being in the *trans* chamber at time t, related to a general transition probability(which satisfies a similar Fokker-Planck equation) by $W_m(t) \equiv P(m,t;m_0,0)$ through the initial condition $W_m(t_0) = P(m,t_0;m_0,t_0) = \delta(m-m_0)$. This relation shows the dependence of $W_m(t)$ on the initial monomer, m_0. k_m is a frictional coefficient encapsulating the local interaction of the m^{th} monomer and the pore due to, e.g., hydrodynamics or details of charge interactions. In making comparisons with simulation and experimental results, it is important to recognize that k_m is a parameter which must be fitted to the data within this model.

We wish to draw attention to the fact that the driving electrochemical potential drop μ_i for a given monomer is modeled to occur only across the pore. The free

energy landscape is a function only of the number of monomers in the *trans* chamber, and assumes that anchored chain on either side of the membrane freely assume all available conformations. This picture is closely analogous to the field configuration E_1 discussed above in the simulations. The equilibrium assumption will be a good one so long as the relaxation time for the chain tails in the *cis* and *trans* chamber are shorter than the typical dwell time for a single monomer in the pore.

A primary quantity of interest will be the mean dwell time given by

$$\tau(m_0) = \int_0^N dm \int_0^\infty dt\, t\dot{W}_m(t)\,. \tag{1.4}$$

It can be shown to obey a differential equation(related to the Backward Fokker-Planck equation[52])

$$\frac{k_{m_0}}{k_B T}\frac{\partial F_{m_0}}{\partial m_0}\frac{\partial}{\partial m_0}\tau(m_0) + k_{m_0}\frac{\partial^2}{\partial m^2}\tau(m_0) = -1\,. \tag{1.5}$$

Imposing appropriate boundary conditions equations (1.3) and (1.5) can be solved for various quantities of physical interest. Here we simply quote results and refer the reader to the Appendix B as well as references by Muthukumar[25] and Gardiner[52] for details of the solutions.

1.2.0.2 Reflecting Chain

A polymer which is physically prohibited from exiting the pore into the *cis* chamber is described using a reflecting boundary condition at the first monomer through the pore and an absorbing boundary condition at the N^{th} monomer to solve equation (1.3). This type of process can be created artificially in experiments[53, 21, 17], as under these conditions all translocation attempts are ultimately successful. The primary quantity of interest is the mean first passage time, which is identical to the dwell time of the polymer in the pore. From equation (1.5) it can be shown[25] for reflecting-absorbing boundaries that

$$\tau(m_0) = \int_{m_0}^{N} dy \, \frac{1}{\psi(y)} \int_0^y dz \, \frac{\psi(z)}{k_z} \,, \tag{1.6}$$

with

$$\psi(y) = \exp\left[-\frac{1}{k_B T} \int_0^y dx \; \left. \frac{\partial F_m}{\partial m} \right|_x \right] . \tag{1.7}$$

We assume the polymer has already overcome the nucleation barrier discussed above and begins with m_0 monomers threaded through the pore. In the case of a reflecting boundary condition all translocation attempts are successful and m_0 may be as small as we wish. A system of particular interest experimentally[43] is that of a charged

block affixed to an uncharged "drag tag" used to manipulate the kinetics of the composite molecule. Taking a diblock polymer with charged block 1 of length f which experiences a chemical potential difference μ_1 across the pore and an uncharged block 2 of length $N-f$ we assign frictional coefficients k_1 and k_2, take $m_0 \to 0$ and obtain

$$\tau = \frac{1}{\mu_1 k_1}\left[f - \frac{1}{\mu_1}\left(1 - e^{-\mu_1 f}\right)\right] + \frac{1}{\mu_1 k_1}(N-f)\left(1 - e^{-\mu_1 f}\right) + \frac{1}{2k_2}(N-f)^2 . \quad (1.8)$$

This has an intuitive physical interpretation: the first and third terms represent the mean first passage times for the first, charged, block and for the second, uncharged, block to pass through the pore, respectively. In the limit of a completely charged chain, $f \to N$, we recover drift dominated behavior such that $\tau \sim N$ while in the limit of no driving force(either $f \to 0$ or $\mu \to 0$), we recover a diffusion dominated process where $\tau \sim N^2$. The total passage time is the first moment of the convolution of the underlying distribution of times to translocate over each block. The second term in equation (1.8) is a cross-term arising from this convolution of underlying distributions. It is insufficient to simply add mean first passage times of different stages of the translocation process in order to arrive at a time for the entire process.

Using equations (1.6) and (1.7) exact expressions for the mean first passage time have been computed for arbitrary distributions of charge along the chain. These full expressions are given in Appendix A and are used to compute expected mean first passage times for the sequences shown in figure 1.2.

1.2.0.3 Absorbing Chain

If the chain is allowed to escape from the pore in either direction then we must impose absorbing-absorbing boundary conditions on equations (1.3) and (1.5). The probability that the chain will "successfully" translocate into the *trans* chamber, given that m_0 monomers are initially nucleated through the pore is[25]

$$\pi_+(m_0) = \frac{\Psi(0, m_0)}{\Psi(0, N)}\,, \tag{1.9}$$

with

$$\Psi(x, y) = \int_x^y dz\, \frac{1}{\psi(z)}\,, \tag{1.10}$$

where $\psi(z)$ captures information about the free energy landscape and is given by equation (1.7). For a diblock copolymer with one block of length f charged and the remaining $N - f$ monomers uncharged, we obtain

$$\pi_+(m_0) = \begin{cases} \frac{\left(1-e^{-\mu_1 m_0}\right)}{\left(1-e^{-\mu_1 f}\right)+\frac{\mu_1}{\mu_2}e^{\mu_1 f}\left(1-e^{-\mu_2(N-f)}\right)} & \text{f} > \text{m}_0, \\ \\ \frac{\left(1-e^{-\mu_1 f}\right)+\frac{\mu_1}{\mu_2}e^{-\mu_1 f}\left(1-e^{\mu_2(m_0-f)}\right)}{\left(1-e^{-\mu_1 f}\right)+\frac{\mu_1}{\mu_2}e^{-\mu_1 f}\left(1-e^{-\mu_2(N-f)}\right)} & \text{f} < \text{m}_0. \end{cases} \tag{1.11}$$

The mean time taken for the chain to complete a successful translocation, where events in which the chain exits back into the *cis* chamber are not counted, is given by[25]

$$\tau_+(m_0) = \frac{\Psi(0,m_0)\phi_+(m_0,N) - \phi_+(0,m_0)\Psi(m_0,N)}{\Psi(0,m_0)\Psi(0,N)}, \tag{1.12}$$

with $\Psi(x,y)$ given in equation (1.10) and $\phi_+(x,y)$ given by

$$\phi_+(x,y) = \int_x^y dp\, \frac{1}{\psi(p)} \int_0^p dq\, \frac{\psi(q)\Psi(0,q)}{k_q}. \tag{1.13}$$

The expressions for $\Psi(x,y)$ and $\phi_+(x,y)$ yield a final expression for $\tau_+(m_0,f)$, which is omitted here as its exact form is unwieldy. The relevant expressions are included in Appendix A for completeness.

Also of interest is the mean first passage time, defined as the mean time for the chain to exit the pore in either direction, which is given by[25]

$$\tau(m_0) = \frac{\int_{m_0}^N dy\, \frac{1}{\psi(y)} \int_0^{m_0} dy'\, \frac{H(y')}{\psi(y')} - \int_0^{m_0} dy \frac{1}{\psi(y)} \int_{m_0}^N dy'\, \frac{H(y')}{\psi(y')}}{\int_0^N dy\, \frac{1}{\psi(y)}}, \tag{1.14}$$

where $\psi(y)$ is given in equation (1.7) and the function $H(x)$ is given by

$$H(x) = -\int_0^x dy \frac{\psi(y)}{k_y}. \tag{1.15}$$

We have again computed exact analytical expressions and they are included in Appendix A.

1.3 Results and Discussion

1.3.1 Reflecting/Absorbing Boundary Conditions

1.3.1.0.1 Field across the pore We show in figure 2.2 histograms for a simple diblock copolymer using field configuration E_1. The chain is composed of one block of f charged monomers which passes through the pore first and a second block of $N - f$ uncharged monomers, with $N = 60$ the total length of the chain. We assume that the friction coefficient is constant within each block and assign the values k_1 to monomers in the charged block and k_2 to those in the uncharged block. By fitting the first moment of the distribution of passage times for a completely charged chain shown in figure 2.2a to the theoretical expression given in equation (B.14) we obtain in reduced LJ units $k_1 = 0.023$. Similarly we find $k_2 = 0.043$ using the distribution

shown in figure 2.2d for the completely uncharged chain. We note that translocation of a completely uncharged chain is meaningful only because of the reflecting boundary condition, which forces the chain to translocate through the entire pore. The translocation is simply a diffusive random walk near a wall in this case. Using the values of k_1 and k_2 obtained through this procedure, theoretical expectations for the distribution of translocation times for different lengths of the charged block have been computed and are shown overlaid on the simulation data in figure 2.2.

From distributions like those shown in figure 2.2 we extract the first moment, which is the mean translocation time. These mean times are plotted in figure 2.3 as a function of the length of the charged block and compared to theoretically computed values from equation (1.8). By the definition of k_1 and k_2 discussed above the times for the homopolymer cases at $f = 0$ and $f = 60$ are identically equal. The theoretical values for intermediate values of f involve no additional fitting. We find good agreement between simulation and theoretical expectations. Our results are in keeping with the physically intuitive expectation that an increase in the amount of charge along the backbone decreases translocation time monotonically.

We find that charge distribution along the chain can have a large effect on the mean translocation time. In order to explore the effect of different distributions of charge along the backbone we fix the total number of charged monomers to be $f = 45$ for a chain of total length $N = 60$. These charges are distributed along the backbone according to the schematic shown in figure 1.2. The mean translocation times for each sequence are shown in figure 2.4 in comparison with theoretical predictions from equation (A.1). The sequence labels along the x-axis correspond to labels in figure 1.2 and are grouped first according to the total number of blocks of similar monomers in the sequence and secondarily arranged according to the number of uncharged blocks in the sequence. Thus, sequence 1 has two total blocks, one charged and one uncharged. Sequences 2, 3, 4, 5, and 6 have three blocks of monomers. Sequences 7 and 8 have four blocks while sequences 9 and 10 have five blocks and sequence 11 has seven blocks. Within these groupings, we have further ordered the individual sequences according to the number of uncharged blocks. As an example, within the grouping of sequences comprised of three total blocks, sequences 2 and 3 have one uncharged block while sequences 4, 5, and 6 have two uncharged blocks.

This ordering makes evident that a finer distribution of charge leads to faster translocation, in good agreement with theory. This effect can be quite significant, as a comparison of the slowest average translocation time for sequence 1 to the fastest for sequence 11 shows an almost 80% reduction due to a finer distribution of charge. Some sequences additionally show a significant effect from the direction of translocation, as in the case of sequences 1, 4, and 5. This asymmetry appears to be correlated to the chain having uncharged endcaps. Nonetheless, the effect is muted for sequences 6 and 10. This effect is not predicted by the theory, and its origin is unclear at present. However, we note that the translocation of a chain with an uncharged initial monomer in the pore relies on an artificially imposed reflecting boundary condition, and will be difficult to realize experimentally. We have included these configurations to make the overall trend of faster translocation with finer charge distributions evident. When only experimentally relevant sequences are considered the agreement between theory and simulation is excellent.

This trend can be intuitively understood by considering that a block of monomers with no charge of length n will have a mean translocation time proportional to n^2, as alluded to briefly in the discussion of equation (1.8). The total number of un-

charged monomers for all sequences in figure 1.2 is 15. Thus for the diblock, sequence 1, the contribution to the mean translocation time of the uncharged block will be proportional to $15^2 = 225$. In contrast, sequence 11 presents three blocks of five uncharged monomers, which contribute to the mean translocation time proportional to $5^2 + 5^2 + 5^2 = 75$. Clearly, the cross-term of equation (1.8)(or the equivalent terms in equation (A.1)) complicates this picture. However, this simple intuitive argument captures the general trend.

1.3.2 Absorbing/Absorbing Boundary Conditions

In order to make contact with realistic experimental and biological systems we must allow the chain to escape from the pore in either direction, whether back into the *cis* chamber or forward into the *trans* chamber. This physical situation is described theoretically by imposing absorbing/absorbing boundary conditions on equations (1.3) and (1.5). Here, it is important to note that the mean first passage time is the mean time taken for the chain to exit the pore *in either direction* and is more accurately thought of as a "dwell" time for the chain in the pore. A calculation of the mean first passage time will therefore include both "successful" and "unsuccessful" events(where unsuccessful means exit into the *cis* chamber and successful means exit

into the *trans* chamber). We will therefore refer to this time, τ, as the mean dwell time. Further, because the chain can exit the pore in either direction, we wish to know the probability of "successful" translocation, which we define as the quantity π_+. Finally, we wish to know the mean first passage time in the event of a successful translocation. We define this quantity to be τ_+, which is the average dwell time for the chain in the pore given that the chain exits into the *trans* chamber. We will refer to this time as the successful translocation time. In this section we will limit ourselves to the case of a simple diblock copolymer, composed of f charged monomers, which thread through the pore first, followed by $N - f$ uncharged monomers. We assume that the chain has already nucleated m_0 monomers into the *trans* chamber.

1.3.2.0.1 Probability of successful translocation Given this initial threading, we can compute the probability of successful translocation, using equation (1.9). In figure 2.6a we show the probability of successful translocation for a diblock copolymer against the length of the charged fraction of the chain for various values of the initially nucleated length. We find that the probability of successful translocation exhibits a distinct shoulder when plotted against the length of the charged block, shown in figure 2.6. As exemplified for a driving force of $\mu = 0.7k_BT$, the probability of

successful translocation of a chain which is $\sim 25\%$ charged is nearly equal to that of a fully charged homopolymer. Increasing the length of the charged block beyond $\sim 25\%$ of the chain length does not significantly increase the probability of successful translocation. Further, the value of f at which the probability saturates is shown in figure 2.6a to be independent of the details of the initial nucleation into the *trans* chamber as the location of the shoulder in the probability remains unchanged with changing values of m_0/N. As expected, the probability of successful translocation increases along with the initially nucleated length, shown by the upward shift of the curves in figure 2.6a with increasing m_0/N.

We have also marked a point on each curve in figure 2.6a at a value of f we define to be f^*. As will be discussed below, this corresponds to a maximum in the average successful translocation time. For the present discussion we note that f^* corresponds closely with the value of f at which additional charge along the backbone has a decreasing effect on the probability of successful translocation.

In figure 2.6b we have plotted the probability of successful translocation against the charged fraction of the chain for various values of the driving potential. Clearly, the saturation value of f does depend on the strength of the driving potential. At a

driving potential of $2k_BT$, the probability saturates at only 10% of the chain being charged. At room temperature this corresponds to a driving voltage of $50mV$, the lower range of experimental voltages reported in the literature. Thus, we expect this saturation in the probability of successful translocation(and the corresponding maximum in successful translocation time, discussed below) to be evident at low experimental voltages and short lengths of the charged block relative to the overall length of the chain. In the limit of an infinite driving force we recover the reflecting case, where $\pi_+ = 1$ identically for all lengths of the charged block.

1.3.2.0.2 Average successful translocation time Given that the chain successfully translocates through the pore, the average translocation time is plotted in figure 2.7a. Theoretical curves are plotted from explicit analytical formulas given in Appendix A and data from simulations are shown for comparison. We find good agreement. We note that no fitting has been done between simulation and theory, values of k_1 and k_2 in the theoretical formula have been taken from those measured in homopolymer simulations with reflecting boundary conditions, as described above. The black dashed line is to guide the eye and represents the mean successful translocation time for an uncharged chain. For absorbing/absorbing boundary conditions,

this quantity is a purely theoretical construct and is not experimentally accessible. In a more practical sense, it may be thought of as the mean time for a minimally charged chain. As the simulation data show, even a chain with 3% of the backbone length being charged will experience successful translocation events. We have included this black dashed line to show that the mean translocation time for a diblock is larger than that of a minimally charged(or, theoretically, an uncharged) chain up to a significant fraction of the chain being charged. As an example, for a driving potential of $2k_BT(\approx 50mV)$, the chain on average will be slower than a minimally charged chain for fractions of the charged block up to nearly 50% of the chain.

We find a maximum in the successful translocation time with increasing length of the charged block length, f, evident from figure 2.7a. We define the location of this maximum to be f^*. The existence of a maximum implies the counterintuitive fact that at small lengths of the charged fraction of the chain, $f < f^*$, increasing the amount of charge along the backbone(and therefore increasing the fraction of the chain that feels a driving force across the pore) leads to an *increase* in the average time taken for a successful translocation. The location of this maximum is controlled by the strength of the driving potential across the pore, shown in figure 2.7b. f^* is inversely related to

the driving potential. At very large values of the driving potential, f^* approaches 0. In such a case, essentially all translocation events will be successful and we recover a reflecting-like boundary on the charged end of the chain as the energy barrier required to retract even one monomer unsuccessfully into the *cis* chamber becomes very large. In the limit of an infinite μ, the mean successful translocation time becomes identical to the mean dwell time as with a reflecting boundary condition. In this limit the plots shown in figure 2.7a become identical to that shown in figure 2.3, corresponding to $f^* \to 0$. The presence of the maximum in the mean successful translocation time will be most evident experimentally for low driving voltages or short lengths of the charged block.

The existence of this maximum in figure 2.7a implies that at a short, fixed length of the charged fraction an increase in the driving potential leads to an increase in the mean successful translocation time. This behavior is illustrated in figure 1.7c where we plot the mean successful translocation time against the driving potential for various lengths of the charged block. At a high enough driving voltage, all chains approach a saturation value for τ_+, where further increases in the driving potential no longer appreciably change the successful translocation time. The time taken to translocate

over the length of the uncharged block is unaffected by changes in the driving potential so that its length entirely dominates τ_+ at these high driving potentials, where the contribution from the charged block to successful translocation time is minimized. For short lengths of the charged block, e.g. $f/N = .05$ and $f/N = .1$, Fig 1.7c shows that increasing the driving potential leads to a monotonic *increase* in the mean translocation time up to a maximum translocation time. For a longer values of the charged block, $f/N = .25$ and $f/N = .5$, a maximum is evident with increasing driving potential. For driving potentials below the location of this maximum, an increase in potential "captures" translocation events that would have quickly exited the pore unsuccessfully into the *cis* chamber, forcing them instead to translocate over their entire length through the pore, a much longer time process. We also note that as the length of the charged block is increased, the position of this maximum moves to lower driving potentials until it vanishes for the homopolymer, $f/N = 1$. This conversion of short time translocation events into longer time events is discussed below with regard to the maximum in successful translocation time with increasing f/N shown in figure 2.7a. The discussions are entirely parallel, and we could replace

the definition of f^* with a value of the driving potential, μ^* instead. We choose to focus here on alteration of f and simply note the parallel.

In order to understand the origin of this counterintuitive maxima in successful translocation time, we have marked the position of f^* in figure 2.6a with a dot on each π_+ curve to show the relationship between f^* and the value of f at which the probability of successful translocation saturates. As discussed above, addition of charge along the backbone when $f < f^*$ leads to an increase in the probability of successful translocation. This increase in the probability of success means that additional charged length captures translocation events that would otherwise retract unsuccessfully into the *cis* chamber for a shorter length of the charged block. This effect is illustrated more clearly in figure 2.8a which shows the theoretically computed unnormalized distributions of successful translocation time. The total area under the histogram is the probability of successful translocation plotted in figure 2.6a. For $f < f^*$, the lengthening of the charged block leads to an increase in the total area under the curve in going from, e.g., $f/N = 0.05$ to $f/N = 0.15$. This increase in the total area under the curve occurs disproportionately in the tail of the distribution, as events which otherwise would have quickly exited the pore in the unsuccessful

direction are "captured" by the additional length of the charged block and then diffuse over the entire length of the chain. This capturing of additional long time events leads to the first moment of the distribution being pulled towards longer times.

When $f > f^*$, a competing effect emerges. Above f^*, the probability shown in figure 2.6a does not change, implying that the total area under the histogram in figure 2.8a is conserved and that addition of charged length does not capture additional events. Instead, the length of the uncharged block is decreased with additional charged length. Thus monomers which experience no driving force across the pore are exchanged for monomers which experience a potential drop across the pore. Long time events in the tails of the distribution are reduced and take less time because they experience a drift force over more of their length, leading to thinner tails in the distribution and pushing the first moment back towards shorter times. This dynamic is evident in going from, e.g. $f/N = 0.15$ to $f/N = 0.25$. figure 2.8b compares the theoretically predicted histogram to that computed in a simulation for a half charged chain of length $N = 60$, $f = 20$. We find good agreement, as expected.

1.3.2.0.3 Mean dwell time Even for a chain which is initially threaded into the pore, some translocation events will end with the chain retracting unsuccessfully into

the *cis* chamber. The average time the chain is in the pore before exiting in either direction, defined to be the mean dwell time τ, is given in Fig 1.9a as a function of the length of the charged block.

The mean dwell time of a completely charged chain is only slightly longer than that of a minimally charged chain. Partially charged chains have average dwell times longer than either the minimally charged chain or the fully charged chain.

The mean dwell time also exhibits a maximum value at a certain value of f. Examination of the histograms in figure 1.9b shows that its origin is similar to that discussed above for τ_+, but is more pronounced. At small values of f, increasing the length of the charged block, e.g. in going from $f/N = .01$ to $f/N = .05$, captures events that would quickly exit the pore into the *cis* chamber and converts them to successful events. Because a successful event requires the entire chain to pass through the pore, these events are longer time events and increase the weight of the long-time tails of the distribution, pulling the first moment towards longer times. At $f/N = .15$, two distinct peaks are evident, one at $\tau \approx 0$ representing unsuccessful events which very quickly withdraw from the pore into the *cis* chamber while the second, broader peak has a very long time tail representing successful translocation events. Above

the value of f where the peak in τ occurs, the shortening length of the uncharged block begins to compensate for this capturing of additional successful events, so that events which are successful experience a drift force over a long enough section of chain that the time taken for translocation does not increase the width of the tails of the distribution. In figure 1.9c we show a simulation histogram of dwell times for $f/N = 0.5$, $\mu = 0.7k_BT$, and $m_0/N = 0.05$ and find good agreement.

1.4 Conclusion

We have investigated the translocation of a sequenced linear polymer through a narrow pore using theoretical tools and Langevin dynamics simulation. Imposing a reflecting boundary condition at one end of the chain, such that retraction into the *cis* chamber is forbidden, we have explored the translocation kinetics of a partially charged diblock and have found good agreement between theoretical predictions for event time distributions and mean first passage times. At a constant charged fraction of the chain, a finer distribution of charge leads to lower mean translocation times. This has an intuitive basis in the $\tau \sim N^2$ scaling law for free translocation, as we have discussed in the text. We note that the theory presented here is based on the key

assumption that the chain conformations are equilibrated throughout the process of translocation, thus allowing the use of the free energy landscape in the calculation of various features of the kinetics. The agreement we find between theory and simulation results gives confidence that this assumption is well founded for the chain lengths and field strengths we have investigated.

Removal of the reflecting boundary condition leads to qualitatively different predictions for a partially charged diblock copolymer, which are born out by simulation. We find that the probability of successful translocation saturates at a threshold length of the charged block independent of nucleation details and well below the length of the entire chain. Below this length of the charged block, additional charge leads to an *increase* in the mean successful translocation time and probability of successful translocation. Above this threshold length of the charged block, additional charge leads to a decrease in the mean time for successful translocation, but does not increase the probability of successful translocation. This maximum in the mean translocation time with increasing length of the charged block can also be understood by considering a diblock with a fixed length of charge and fixed overall length. If the ratio of the length of the charged block is below the saturation value in the probability, an

increase in the driving potential will lead to an increase in the mean translocation time. Both of these effects have their origin in the saturation of the probability. Below the saturation value of f, increasing f at fixed μ(or vice versa) "captures" events that would otherwise quickly exit the pore and converts them into long time events which must slowly diffuse over the entire length of the chain, thus pulling the average time upward while also increasing the probability of successful translocation.

We are at present not aware of a systematic experimental study of the effect of the length of the charged fraction on the translocation of a diblock copolymer and hope that the present work will stimulate further experimental investigation. We note that these effects will be most evident at low driving strengths and short lengths of the charged block.

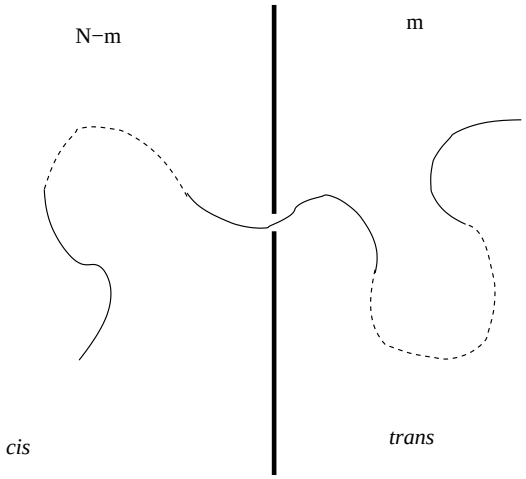

Figure 1.1: Theoretical model of translocation through infinitely thin pore.

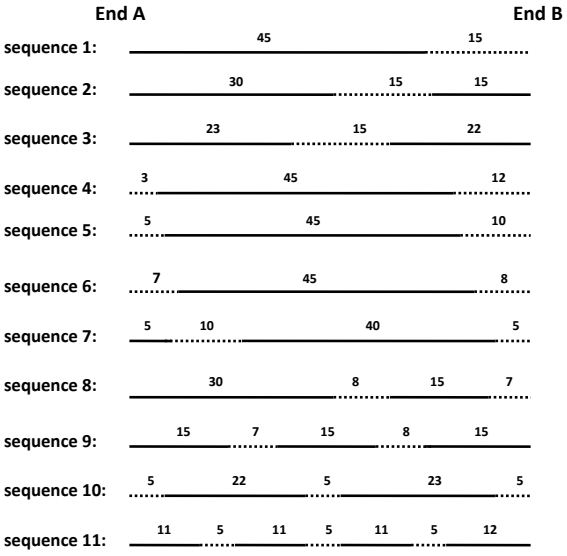

Figure 1.2: Distributions of charge. All chains have f = 45 charged monomers.

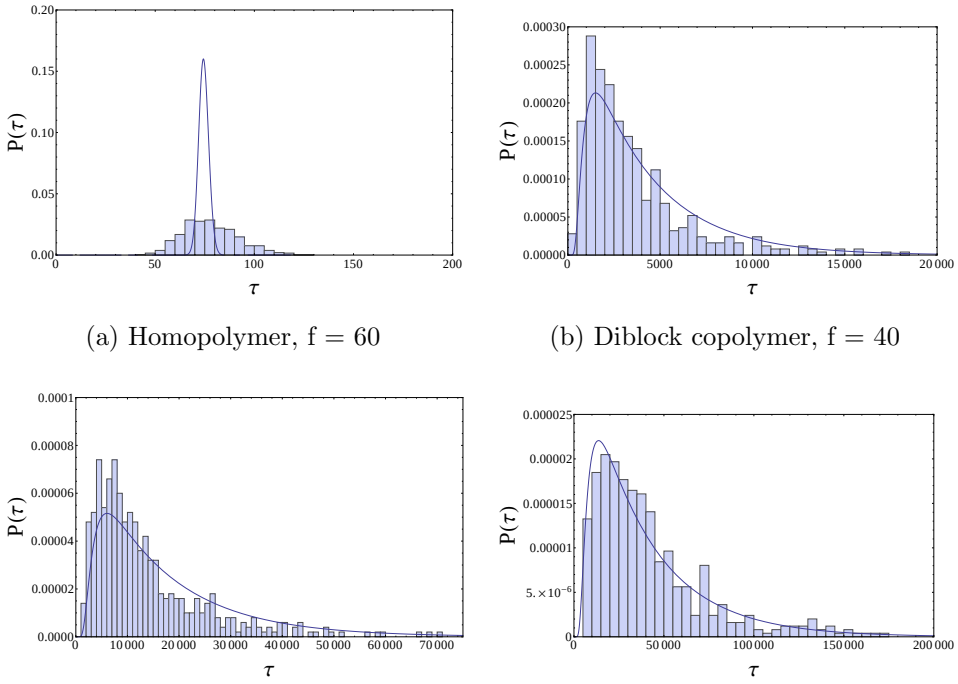

(a) Homopolymer, f = 60

(b) Diblock copolymer, f = 40

(c) Diblock copolymer, f = 20

(d) Homopolymer, f = 0

Figure 1.3: Histograms of normalized number of translocation events with passage time τ for diblock copolymers with various lengths of the charged block f, compared against theoretical prediction. Total length of the chain, $N = 60$. Simulation data with thanks to Yanbo Wang[1].

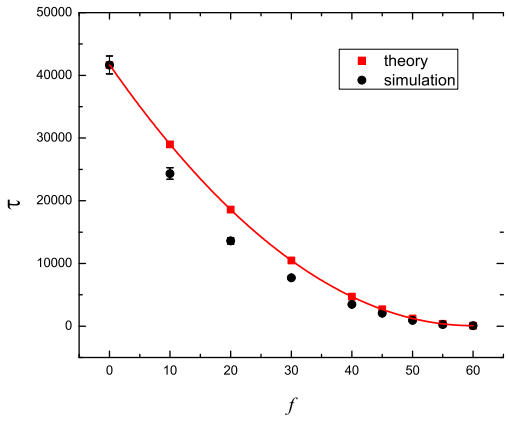

Figure 1.4: Mean first passage time of a diblock copolymer for various lengths of the charged block. $N = 60$. Simulation data with thanks to Yanbo Wang[1].

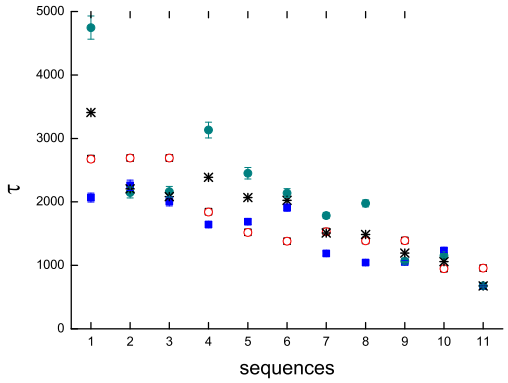

Figure 1.5: Mean first passage times for a fixed total charge $f = 45$ distributed according to sequences shown in figure 1.2. Open symbols are theoretical predictions, closed symbols are simulation results. Squares represent translocation from end A to end B, circles from end B to end A, stars are the average of the simulated times. Simulation data with thanks to Yanbo Wang[1].

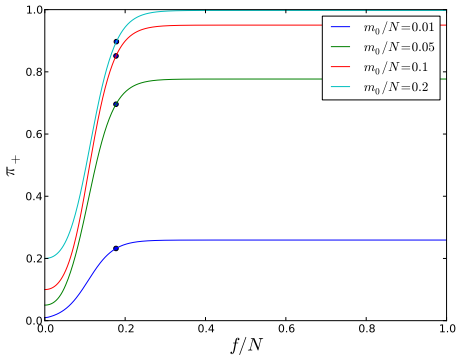

(a) Probability of successful translocation for various initially nucleated lengths. $\mu = .7k_BT$

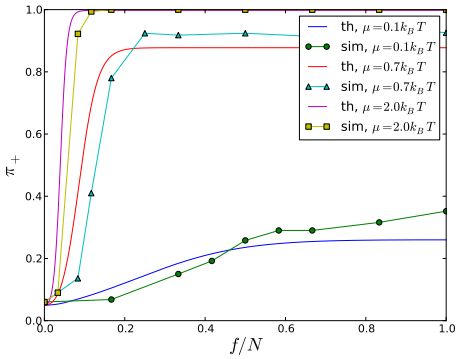

(b) Probability of successful translocation for various driving potentials across the pore. Connected dots are simulation data, solid lines are theoretical curves. $m_0/N = .05$

Figure 1.6: Probability of successful translocation for a diblock with various lengths of the charged fraction. Simulation data with thanks to Yanbo Wang[1].

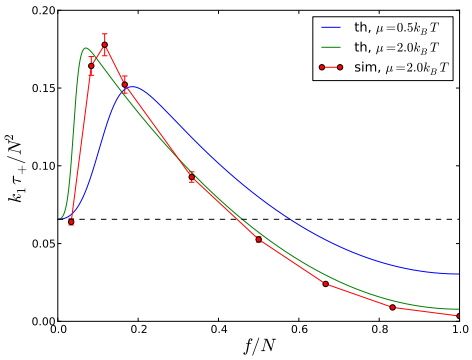

(a) τ_+ vs f for various values of the driving potential. Connected dots are simulation data, solid lines are theoretical curves. $m_0/N = .05$.

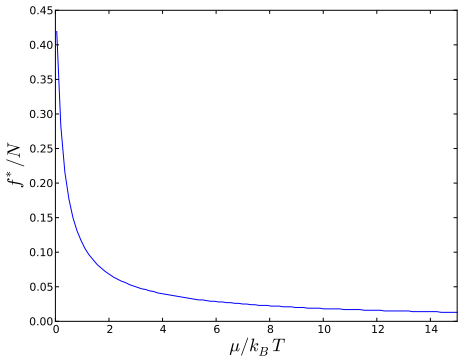

(b) f^*/N vs driving potential. $m_0/N = .05$

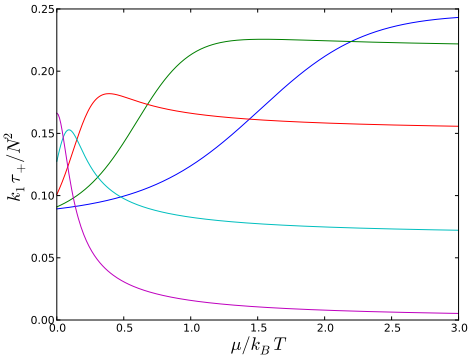

(c) τ_+ vs driving potential μ for various lengths of the charged block. $f/N = .05(\text{blue}), .1(\text{green}), .25(\text{red}), .5(\text{aqua}), 1(\text{purple})$. $m_0/N = .05$

Figure 1.7: Mean successful translocation time. Simulation data with thanks to Yanbo Wang[1].

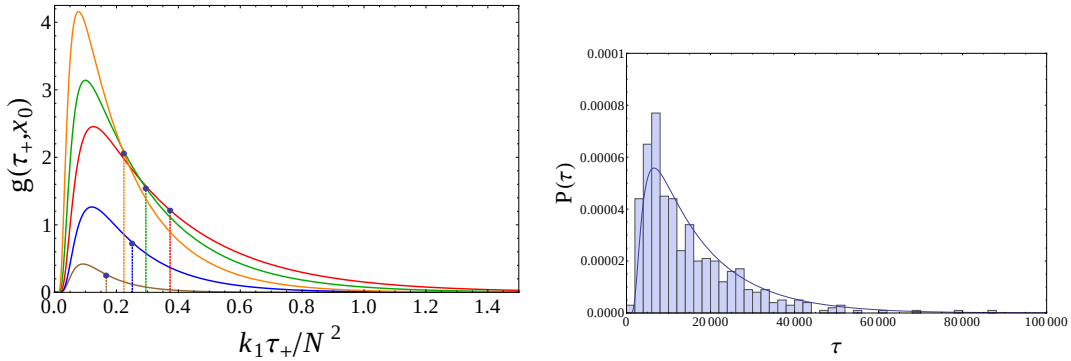

(a) Expected histograms of successful translocation time for f/N = .01(brown), .05(blue), .15(red), .25(green), .35(orange).
$\mu = .7k_BT$, $m_0/N = .05$. Vertical lines mark the first moment of the distribution

(b) Comparison of theoretically predicted normalized histogram with simulation data

Figure 1.8: Histograms for mean successful translocation times. Simulation data with thanks to Yanbo Wang[1].

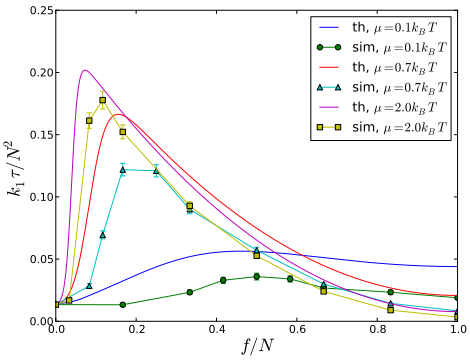

(a) Mean dwell time against length of the charged block for various driving potentials. Connected dots are simulation data, solid lines are theoretically computed.

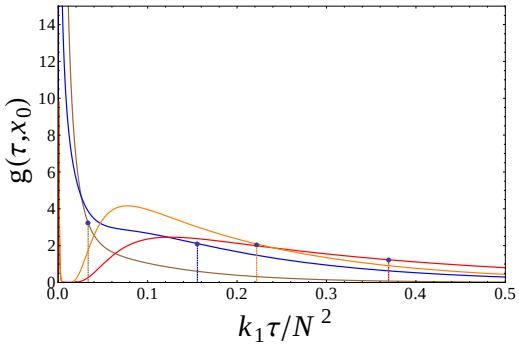

(b) Expected histograms of successful translocation time for $f/N = .01$(brown), $.05$(blue), $.15$(red), $.35$(orange). $\mu = .7k_BT$, $m_0/N = .05$. Vertical lines mark the first moment of the distribution.

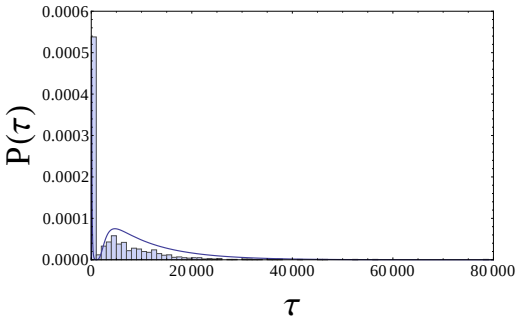

(c) Comparison of theoretically predicted normalized histogram with simulation data

Figure 1.9: Mean dwell time and associated histograms. Simulation data with thanks to Yanbo Wang[1].

CHAPTER 2

KINETICS OF PARTICLE WRAPPING

2.1 Introduction

Endocytosis is a ubiquitous process in biological systems and over a century of research, dating from the Nobel prize winning work of Metchnikoff[54], has given birth to a richly detailed picture of this cellular function [55, 56, 57, 58, 59]. In addition to its intrinsic importance as a fundamental biological process, interest in the mechanics[60, 61, 62, 63, 64] and kinetics[65, 66, 67] of the wrapping process has intensified in light of technological applications in drug delivery[64, 66, 68, 69, 70, 71, 72, 73, 74], gene delivery[75, 76] and the design of nanoreactors[77, 78, 79, 80, 81, 82, 83, 84, 85, 86] which would allow for highly controllable reaction conditions.

While a variety of biochemical mechanisms and pathways fall under the heading of "endocytosis"[55], certain generic physical features of the process are inescapable. Dietrich and coworkers[65] made steps towards elucidating these features by studying

the adhesion of latex spheres to "giant lipid vesicles" with sizes in the range of 10 to 100 microns. Using light microscopy they observed through time four steps in the passive engulfment of the latex bead: adhesion, ingestion, explusion and recapture. They were able to qualitatively model the observed behavior with a simple, single parameter, geometric model that accounted only for the interplay between membrane tension and the adhesion energy between the vesicle and bead. Deserno and Gelbart[60] subsequently extended this model with the addition of a second parameter, considering the balance of membrane curvature, tension and adhesion. This allowed them to predict the behavior of smaller bead sizes, an inadequacy of the earlier theory. Using this model they constructed a phase diagram in terms of the relative size of the vesicle and the particle. A key finding was the importance of a softened "shoulder" in the neighborhood of the adhered particle allowing for the passage of much smaller beads than in the earlier model of Dietrich, et al.

Previous work has shown an optimal particle size for wrapping in biological, receptor mediated endocytosis on the basis of a competition between the entropy loss from diffusion of receptors on the membrane surface to the particle and the adhesion energy gain in wrapping the particle[64]. We show here that such an optimal particle

size is a generic feature even of a single particle wrapping and generic particle/vesicle interaction, due only to the competition of bending and stretching energies with the attractive energy of the particle, without regard to the dynamics of receptors. Recent experimental[87, 67] and simulational[77] work has focused on the mechanics of wrapping at the single particle level, and our work will be relevent to the kinetics of such processes.

Additionally, Wang and Muthukumar have recently computed the free energy for a polyelectrolyte chain inside a rigid spherical cavity[88]. They have found that for sufficiently large attractive energies between the chain and the confining membrane there exists an optimal size of the vesicle dictated by the balance between chain confinement and attractive interactions. When the attractive energy is lowered, this energy dominated regime crosses over to an entropy dominated regime, wherein the optimal size of the confining cavity becomes infinite.

We consider here the inverse problem to that of Wang and Muthukumar: the wrapping of a rigid particle by a flexible vesicle. We consider the vesicle to possess a bending and stretching modulus and to wrap the particle at constant volume. We find that the bending and stretching moduli of the membrane dictate a range of particle

sizes over which wrapping will occur, with an intermediate particle size at which the rate of wrapping is maximized. The ability to design synthetic vesicles able to uptake soft particles such as a polymer will rely on the ability to match the energy and length scales of the vesicle to those of the particle.

In the remainder of the chapter we compute the kinetics of passage rate using a simple geometrical ansatz for the vesicle shape. In the next section we give a geometrical model for the vesicle shape as the particle is wrapped, originally introduced by Deserno and Gelbart[60]. Following their work, we use this geometric ansatz to compute free energy landscapes for the process of encapsulation. Deserno and Gelbart previously used these free energy landscapes to compute thermodynamic phase diagrams for encapsulation. We extend their work by considering the process of wrapping as a stochastic process over these free energy landscapes, controlled by the Fokker-Planck equation. In the third section we show example free energy landscapes and their associated passage rates. We find that even the simplified model presented here predicts that the vesicle preferentially chooses an optimal particle size and dictates a maximum passage rate as a function of the relative size of the vesicle and bead and

as a function of vesicle material properties. Finally we close with brief concluding remarks in the final section.

2.2 Model

2.2.1 Geometry

During the process of encapsulation of a rigid spherical bead by a closed vesicle, as in figure 2.1, the resistance of the vesicle membrane to bending and stretching changes must be overcome by the free energy gain in the system due to adhesion of the bead to the membrane. The free energy penalty of these factors can be imposed by means of Lagrange multipliers conserving global curvature and area[89].

$$\Delta F = -wA_{contact} + \frac{\kappa}{2}\int_{\Omega}(2H - c_0)^2 + \lambda\frac{\Delta A^2}{2A_0} \tag{2.1}$$

The meanings of the moduli w, κ, and λ are: the energy penalty (or gain) for contact, bending and stretching, respectively. In typical physical systems the time scale of volume change is much larger than that for bending and stretching of the membrane so that we take the volume to be constant in our model. The second term is the well

known Helfrich free energy[90], including a spontaneous curvature for the membrane, c_0. H is the local mean curvature of the membrane.

At any point in the process of encapsulation, we assume the membrane will have three sections: the contact region, the shoulder region, and the bulk region. We show a cross section of such an axisymmetric complex in figure 2.1. Following Deserno and Gelbart[60], we model the contact region as a spherical cap, shoulder as a toroidal section, and the bulk region as a partial sphere. A well known result from the geometry of surfaces states that a sphere encloses a maximum volume with the minimum possible surface area[91]. This result suggests a definition of the excess area of a closed vesicle in the following way[60]. Define a radius, R_0 which is proscribed by the volume enclosed in the vesicle according $V_0 = 4/3\pi R_0^3$. The lipids(or other material) making up the vesicle will, in equilibrium, span an area A_1. The excess area will be given by the difference between this area and the area of a sphere with radius R_0: $\Delta A = A_1 - 4\pi R_0^2$. If $\Delta A > 0$ the relaxed membrane will have more area than necessary to enclose its volume and will therefore be flaccid. In this regime, the deviation from our model geometry is large and the full shape equations[61, 92] must be solved numerically to arrive at an accurate understanding of the complexation. However, if

$\Delta A < 0$ then the membrane will be under tension and take a spherical shape. It is in this regime that our model will be most useful.

Using the ansatz shown in figure 2.1 for the geometry of the complex we can write down analytic expressions for each term in the free energy of equation (2.1). It is assumed that in the contact region the membrane shape will conform to the bead with radius a, while the bulk region will remain in the shape of a sphere with radius R. To allow for analytical calculation, the shoulder region is assumed to be in the shape of a torus. With these assumptions, the shape of the complex is completely determined by three parameters: ϕ, the wrapping angle, b, the inner radius of the toroidal shoulder, and R, the radius of the bulk region of the vesicle, as illustrated in figure 2.1. R is determined in terms of b and ϕ by assuming that the enclosed volume of the vesicle is conserved. As the bead is encapsulated by the vesicle ϕ will take on values from 0, signifying that the bead is just tangentially in contact with the vesicle, to some final value where the free energy is minimized. In the case of full encapsulation, the global free energy minimum will occur when ϕ is π. The model does not incorporate the rupture of the vesicle wall as the final stage.

Within this model the adhesion energy will be simply proportional to the area of the contact region between the vesicle and the bead. This can be calculated in a straight forward way as

$$\begin{aligned} F_{ad}^{cont} &= -w \int dA^{cont} = -2\pi \int_0^{\phi} d\psi a^2 \sin\psi \\ &= -2\pi w a^2 (1 - \cos\phi) \end{aligned} \tag{2.2}$$

It is easily shown that the mean curvature of a sphere is the inverse of the radius. We may plug this into the Helfrich free energy to obtain the bending contribution to the free energy due to bending in the contact region

$$\begin{aligned} F_b^{cont} &= \kappa \int dA^{cont} (H - c_0)^2 \\ &= 2\pi\kappa a^2 (1 - \cos\phi)(\frac{1}{a} - c_0)^2 \end{aligned} \tag{2.3}$$

where we have used $H = 1/a$ for a sphere of radius a and c_0 is a spontaneous curvature.

The bending penalty for the toroidal region is

$$\begin{aligned} F_b^{tor} =& \kappa \int dA^{tor} (2H - c_0)^2 \\ & \frac{\pi}{2}\kappa b \int_{-\phi}^{\theta} d\psi \frac{\sin^2\psi}{(a+b)\sin\phi - b\sin\psi} - 2(\cos\theta + \cos\phi)\left(\frac{1}{b}\right) \\ & + [(a+b)(\theta+\phi) + b(\cos\theta + \cos\phi)]\left(\frac{1}{b} + c_0\right)^2 \end{aligned} \tag{2.4}$$

The bending energy of the bulk region is

$$F_b^{bulk} = 2\pi\kappa R^2 \left(\frac{1}{R} - c_0\right)^2 (1 + \cos\theta) \tag{2.5}$$

The stretching energy penalty at a given wrapping angle is taken to be harmonic in the change of area:

$$F_{stretch} = \lambda \frac{[A - A_0]^2}{2A_0} \tag{2.6}$$

The area of the vesicle geometry is the sum of the areas of the contact, toroidal, and bulk region and can be computed using differential geometry. For the contact, toroidal, and bulk regions we obtain.

$$A^{cont} = 2\pi a^2(1 - \cos\phi) \tag{2.7a}$$

$$A^{tor} = 2\pi b[(a + b)\sin\phi(\theta + \phi) + b(\cos(\theta) + \cos(\phi))] \tag{2.7b}$$

$$A^{bulk} = 2\pi R^2(1 + \cos(\theta)) \tag{2.7c}$$

Inserting these expressions giving the geometry of the complex into equation (2.1) we arrive at an expression for the free energy of the complex as a function of the wrapping angle, inner radius of the toroidal shoulder, and radius of the bulk region.

$$
\begin{aligned}
F(\phi,b) = & -2\pi w a^2\,(1-\cos\phi) + 2\pi\kappa a^2(1-\cos\phi)(\frac{1}{a}-c_0)^2 \\
& + \pi\kappa\left\{\frac{b}{2}\int_{-\theta}^{\phi} d\psi \frac{\sin^2\psi}{(a+b)\sin\phi - b\sin\psi} + b\left(\frac{1}{b}+c_0\right)(\cos\theta-\cos\phi)\right. \\
& \qquad + \frac{b}{2}\left(\frac{1}{b}+c_0\right)^2\left[(\theta+\phi)\,(a+b)\sin\phi + b\,(\cos\theta-\cos\phi)\right] \\
& \qquad \left. + 2R^2\left(\frac{1}{R}-c_0\right)^2(1+\cos\theta) - 4\right\} \\
& + 2\pi\lambda\left\{a^2\,(1-\cos\phi) + b\left[\,(a+b)\sin\phi\,(\theta+\phi)\right.\right. \\
& \qquad \left.\left. + b\,(\cos\phi-\cos\theta)\right] + R^2\,(1+\cos\theta) - 2R_0^2\right\}^2/(2R_0)^2
\end{aligned}
\tag{2.8}
$$

Here, θ is not independent, but is related to R, b, a, and ϕ by the relation $(a+b)\sin\phi = (R-b)\sin\theta$.

R is determined by the fixed volume constraint

$$
\begin{aligned}
\Delta V = & \frac{4}{3}\pi R_0^3 - \{\frac{2}{3}\pi R^3(1+\cos\theta) - \frac{2}{3}\pi a^3(1-\cos\phi) \\
& \qquad + \frac{1}{3}\pi(a+b)^2\sin^2\phi\big[(R-b)\cos\theta + (a+b)\cos\phi\big] \\
& \qquad + \pi b^2\big[(\theta+\phi)(1+b)\sin\phi + \frac{2}{3}b(\cos\phi-\cos\theta)\big]\} \\
= & \quad 0
\end{aligned}
\tag{2.9}
$$

Using this equality, R can be eliminated from equation (2.8) so that the free energy of the complex is a function only of ϕ and b. By then minimizing this free energy with respect to b at each value of ϕ, we construct a free energy landscape over ϕ for an

equilibrium process of encapsulation, following Dietrich and Angelova[65] and Deserno and Gelbart[60]. The equation is physically transparent in light of equation (2.1). Each term in brackets contains geometrical information about the configuration of the complex and is then multiplied by the appropriate modulus. As was originally pointed out by Dietrich and Angelova[65], for large particle sizes, the bending contribution can be neglected and the toroidal shoulder reduces to a sharp kink, so that the process of encapsulation is purely a competition between adhesion energy and the stretching energy. The relative strengths of these contributions are characterized by the ratio of their moduli, $\zeta = w/\lambda$.

Further physical insight into the free energy can be had by examining the limit of full wrapping, where $\phi \to \pi$, following Deserno and Gelbart. Taking this limit it can be shown that the free energy reduces to[60]

$$\frac{F}{k_B T} = 2\pi\lambda R_0 \left\{ \left[\left(1 + \frac{a}{R_0}^3 \right)^{2/3} + \left(\frac{a}{R_0} \right)^2 - 1 \right]^2 - 2\zeta \left(\frac{a}{R_0} \right)^2 + 4.603\zeta \frac{\kappa}{w} \frac{1}{R_0^2} \right\} \tag{2.10}$$

The first term of this equation arises due to membrane stretching and the second term from the adhesion energy contribution. The last term of this equation contains a prefactor 4.603, which comes from taking the limit of $\phi \to \pi$ in the toroidal shoulder.

There is also a multiplying factor $\frac{\kappa}{w}$ in the last term, which suggests the definition of a length scale $l_c = \sqrt{\kappa/w}$. Its significance can be understood by expanding this limiting equation for small particle radii. Doing this, Deserno and Gelbart argued that the minimal vesicle size to wrap a particle of radius a is given by[60]

$$R_0\sqrt{\zeta}/l_c = \frac{a/l_c}{\sqrt{2 - 4.603(l_c/a)^2}} \tag{2.11}$$

They point out that this expression diverges when $a \approx 1.52 l_c$; that is, the minimum vesicle size to wrap such a particle becomes infinite, so that there is no vesicle size which can wrap particles smaller than this radius. The value of this minimum radius is controlled entirely by $l_c = \sqrt{\kappa/w}$ depending on the adhesion strength and bending modulus and being insensitive to the stretching modulus. Further, they suggest that the wrapping of large particles is controlled primarily by stretch in the membrane, characterized by the dimensionless parameter $\sqrt{\zeta}$ from equation (2.11), while the wrapping of small particles is controlled by bending, characterized relative to the adhesion energy by the length scale l_c. Thus, at small particle sizes, wrapping behavior is dictated by bending of the membrane, while at large particle sizes wrapping is dictated by stretching of the membrane.

2.2.2 Kinetics

At a given wrapping angle, we consider thermal fluctuations of the membrane will cause the area of contact to change in a stochastic way, so that ϕ can be treated as a stochastic variable moving from 0 to π with some drift due to the free energy gradient in equation (2.8). Drawing an analogy with nucleation theory[93], we define the probability of the membrane being wrapped to angle ϕ at time t to be $W(\phi, t)$. At any given time, the probability that the wrapping angle will transition to some different wrapping angle at $\phi \pm d\phi$ will obey a master equation,

$$\frac{\partial}{\partial t}W(\phi,t) = k_{\phi-d\phi}W(\phi-d\phi,t) - k'_{\phi}W(\phi,t) - k_{\phi}W(\phi,t) + k'_{\phi+d\phi}W(\phi+d\phi,t) \quad (2.12)$$

Here k_ϕ is the transition rate between a wrapping angle ϕ to an incrementally larger wrapping angle $\phi + d\phi$ while k'_ϕ is the transition rate in the other direction, from ϕ to $\phi - d\phi$. Invoking detailed balance $k'_{\phi+d\phi}$ can be written in terms of k_ϕ so that in the continuous limit we obtain[28]

$$\frac{\partial}{\partial t}W(\phi,t) = \frac{\partial}{\partial \phi}\left[\frac{k}{k_B T}\frac{\partial F(\phi)}{\partial \phi}W(\phi,t) + k\frac{\partial}{\partial \phi}W(\phi,t)\right] \quad (2.13)$$

where we have additionally assumed that the transition rate $k_\phi \equiv k$ is constant throughout the wrapping process. k sets a fundamental time scale for the stochastic process of wrapping and is determined by nonuniversal features of the membrane such as hydrodynamic interactions with the particle, the relaxation of the small lipids, and other microscopic details of the wrapping. The mapping of the wrapping process to the Fokker-Planck equation makes the important assumption that the encapsulation process is slow compared to the relaxation of the small lipid molecules within the membrane, so that the vesicle equilibrates fully at each wrapping angle. If this assumption does not hold, memory effects in the membrane will become important and our approach will be invalid.

Viewing the wrapping angle as a stochastic variable means that the encapsulation of the particle will occur over a distribution of times, related to the full probability distribution, $W(\phi, t)$[52]. The average time at which the wrapping angle first equals π (full encapsulation) is defined to be the mean first passage time and is given by

$$\tau = \int_0^\infty dt\ t\dot{W}(\phi, t) \tag{2.14}$$

The mean first passage time can be shown to obey the equation(related to the backward Fokker-Planck equation)[52]

$$\frac{k}{k_B T}\frac{\partial F_{m_0}}{\partial \phi_0}\frac{\partial}{\partial \phi_0}\tau(\phi_0) + k\frac{\partial^2}{\partial \phi_0^2}\tau(\phi_0) = -1 \tag{2.15}$$

Assuming the particle does not disengage the vesicle complex during the process of ecapsulation, this equation can be solved to give an expression for the mean first passage time of the particle into the vesicle.

$$\tau = \frac{1}{k}\int_0^{2\pi} d\phi_1 \int_0^{\phi_1} d\phi_2 e^{[F(\phi_1)-F(\phi_2)]/k_B T} \tag{2.16}$$

Our primary quantity of interest will be the uptake rate of the particle which we define to be the inverse of the mean first passage time, $1/\tau$. We wish to understand how the adhesion between the particle and the vesicle, the bending and stretching moduli of the vesicle, and particle and vesicle sizes affect this quantity.

2.3 Results

2.3.1 Free Energy Landscapes

A typical set of free energy landscapes over ϕ are shown in figures 2.2 and 2.3. All plots in figure 2.2 show a typical set of free energy landscapes for a small particle,

$a = 10nm$, while all plots in figure 2.3 are for a large particle with $a = 75nm$. The size of the vesicle in these figures is taken to be $1\mu m$. Within each figure, the subfigures have been arranged for easy comparison between them, so that, e.g. figure 2.2a is comparable to figure 2.3a save for a different bead size and so on for each figure. Our findings here are in keeping with previous results of Deserno and Gelbart[60], although here we have presented explicit free energy landscapes. We have done this to elucidate several features of the free energy landscape.

In both figures 2.2a and 2.3a we see that for small attractive energies w, between the vesicle and particle, the free energy is a minimum at $\phi = 0$, indicating the particle will remain completely unwrapped. As the attractive energy is increased, the fully wrapped $\phi = \pi$ state becomes the equilibrium configuration. At intermediate strengths of the attractive interaction the global minimum occurs at an intermediate value of ϕ, indicating that a partially wrapped state is the equilibrium configuration. The depth of this intermediate minimum is much shallower for the small particle shown in figure 2.2a, in keeping with expression (2.2), which shows that the attractive energy is a function not only of the adhesion strength but also of the area of contact.

A larger bead presents a larger area of contact, resulting in the deeper minimum in figure 2.3a.

Figures 2.2b and 2.3b show the effect of changes in the bending modulus on the free energy landscape for small (figure 2.2b) and large (figure 2.3b) particles. In contrast to changes in the adhesion energy, which effected a transition from unwrapped to fully wrapped equilibrium states for both particle sizes, changes in the bending modulus of the membrane have only a muted effect on the free energy landscape for large particle sizes and a typical range of experimental bending moduli[94], shown in figure 2.3b. For the small particle size, shown in figure 2.2b, decreasing the bending modulus results in a transition from an equilibrium unwrapped state(e.g., for $\kappa = 35k_BT$) to an equilibrium wrapped state(e.g., for $\kappa = 5k_BT$). The marked difference in the effect of changing the bending modulus for different particle sizes is in keeping with the previous discussion of the length scale l_c, which arises in the limit of small particles. When $a >> l_c$, κ does not significantly affct the free energy. This can be further intuitively justified by considering that equations (2.3) and (2.5) are (when $c_0 = 0$) independent of the bead size, while equation (2.4) goes like a. Thus, the bending contribution to the free energy only increases linearly with increasing particle size.

Equations (2.2) and (2.6) show that the adhesion and stretching energies increase with particle size like a^2. Thus, for small particle size, the bending contribution to the free energy is significant, and therefore changing the bending modulus has a significant effect on the free energy landscape. For large particle sizes bending is still present, but the adhesion and stretching contributions dominate the bending contribution.

The converse of this behavior due to the bending contribution is demonstrated in figures 2.2c and 2.2d compared to figures 2.3c and 2.3d. These figures show the effects of changing the stretching modulus and initial vesicle size. These variables are analogous to one another in controlling the stretching contribution to the free energy landscape. For small particle sizes, the overall stretching penalty is small, and changing the initial vesicle size or the stretching modulus has only a small effect on the overall free energy landscape, as can be seen in figures 2.2c and 2.2d. In contrast, the stretching needed to engulf a large particle while maintaining a constant volume is large so that changes to the stretching contribution leads to very different free energy landscapes. In figures 2.3c and 2.3d we see that an increase in the stretching modulus is analogous to shrinking the initial size of the vesicle. As the stretching modulus is increased, the equilibrium state of the complex changes from a full wrapped to

partially wrapped state. Stretching of the membrane is very small at small wrapping angles, and partial wrapping is forbidden only in the limit of an infinitely stiff vesicle. An increase in the stretching contribution to the free energy, whether via a decrease of the initial particle size or an increase in the stretching modulus, will never completely forbid at least some minimal partial wrapping for suitable values of the adhesion energy and particle size.

This change in the profile of the free energy in going from small particles to larger particle sizes is illustrated explicitly in figure 2.4 where we have plotted the free energy as a function of ϕ for various particle sizes ranging from $a = 10nm$ to $a = 100nm$, holding all other features of the system constant. As we have just discussed, at small particle sizes, increasing the particle size increases the area of contact between the particle and vesicle, increasing the contact energy between them. For a $1\mu m$ vesicle with $w = .25k_BT/nm^2$, $\kappa = 20k_BT$, and $\lambda = 50k_BT/nm^2$ shown in figure 2.4, this is seen by comparing the blue curve for $a = 10nm$, which will remain completely unwrapped to the green curve for $a = 30nm$, which will be completely wrapped due to the greater adhesion energy from the great contact area with the larger particle. As the size of the particle is further increased from , e.g. $a = 50nm$ to $a = 80nm$, the

stretching energy due to the area change necessary to fully encapsulate the particle causes the free energy of the fully wrapped state to become large and a minimum forms in the free energy at an intermediate wrapping angle. The equilibrium configuration of the complex is partially wrapped. Previous work by Deserno and Gelbart has mapped the phase diagram for differing vesicle/bead sizes[60] and differing stretching and adhesion energies[61].

2.3.2 Kinetics of Wrapping

We use free energy profiles such as those show in figures 2.2 to 2.3 to compute uptake rates from equation (2.16). Figure 2.5 shows the effect of vesicle size and stretching modulus on the uptake rate of particles. The uptake rate is non-zero only within a range of particle sizes, defining a range of selectivity of the vesicle. As an illustrative example, at a particle size of $a = 10nm$, the uptake rate shown in figure 2.5a is zero for all vesicle sizes. For a vesicle size of $1\mu m$, this corresponds to the blue curve in figure 2.4, which monotonically increases and shows a minimum at $\phi = 0$, giving a completely unwrapped equilibrium configuration. Choosing now $a = 50nm$, figure 2.5 shows an uptake rate of $1/k\tau \approx 100$. This uptake rate corresponds to the red free energy profile shown in figure 2.4 for $a = 50nm$. Further increase in the size

of the particle leads to a sharp dropoff in the uptake rate to zero, corresponding to the appearance of a partially wrapped minimum in the free energy profile of figure 2.4. The sharpness of this dropoff is a function of the large values of the free energy involved, on the order of $10^5 k_B T$. Thus, the depth of the free energy minimum increases beyond $1 k_B T$ very quickly with further increases in the size of the particle. The sharpness of the dropoff means that the range of allowed particle sizes that will become fully wrapped corresponds closely to those particle sizes previously computed by Deserno and Gelbart[60]. As expected from the above discussion of the free energy landscapes, we see that only the upper limit of this allowed range is controlled by these two features of the complex. This arises because the stretching contribution to the free energy enters primarily for large particle sizes. The wrapping for small particles is controlled primarily by the balance between bending and adhesion energies, and is therefore not affected by the vesicle size or the stretching modulus.

The uptake rates in figure 2.5 show a maximum at a particle size which we define as a^* with a corresponding uptake rate $1/\tau^*$. The optimum particle size lies close to the upper cutoff particle size, and therefore is largely controlled by this boundary. As discussed above, this implies that it is largely controlled by the onset of the

intermediate minimum in the free energy profile due to an increase in the stretching penalty for wrapping larger particles. In figure 2.6a we show this optimal particle size as a function of vesicle size. We find a^* grows linearly with R_0, with a slope controlled by the strength of the attractive energy. For $w = .125$ we find $a^* = .038 * R_0$, $w = .25$ gives $a^* = .053 * R_0$, and $w = .5$ gives $a^* = .072 * R_0$. The competition between stretching and adhesive energies can be characterized by the ratio of the adhesive energy and the stretching modulus[65] as discussed above. We find that increasing the vesicle size increases the optimal particle size with a slope roughly given by $\sqrt{\zeta} = \sqrt{w/\lambda}$ so that $a^* \sim \sqrt{\zeta} * R_0$. This is a direct consequence of a^* being determined primarily by the stretching penalty and the sharp cutoff in the uptake rate in figure 2.5 and was previously reported by Deserno and Gelbart[60] with reference to the maximum allowable particle size. It is important to emphasize that in principle the maximum allowable size for encapsulation and the optimum size can in principle be quite different, as is the case for some biological model of endocytosis emphasizing diffusion of membrane receptors[73]. This picture is also consonent with the behavior of a^* as λ is increased. Figure 2.6b shows a^* falling off $\sim 1/\sqrt{\lambda}$, in keeping with this relationship.

The presence of an optimal particle size corresponds with a maximal uptake rate for particles of that size, which we have defined to be $1/\tau^*$. In figures 2.6b and 2.6d we have plotted this maximal uptake rate as a function of vesicle size and stretching modulus, respectively. As an example, we take $w = .25k_BT$ in figure 2.6a and see that the vesicle will preferentially uptake particles with a radius of $\sim 75nm$. This corresponds in figure 2.6b to a maximal uptake rate of $1/\tau^* \approx 175$ in units of the rate constant, k. It is important to realize that each data point in figure 2.6b (and figures 2.6d, 2.8b, and 2.8d) are computed for a different size of the particle, and therefore has a unique free energy landscape associated with it. For this reason, analytical results are not available. From this free energy landscape (chosen to maximize the uptake rate), we have computed $1/\tau^*$ via equation (2.16).

Figure 2.6b shows that below a certain minimum size of the vesicle, all uptake of particles is inhibited; i.e. for $w = .25k_BT$ this is near $R_0 = 250nm$. This lower limit on vesicle size arises because of an interplay between the attractive energy and stretching energy. As has been previously discussed, the attractive energy driving wrapping is proportional to the area of contact between the particle and the vesicle so that in order for the particle to be wrapped by the membrane, it must be large enough that the

attractive energy creates a negative slope in the free energy. However, small vesicles have a great sensitivity to increasing particle size, as even small increases in particle size necessitate large stretching energies to wrap. At some minimum initial size of the vesicle, the particle size necessary to drive the downhill attractive force creates a stretching penalty too large to allow full wrapping, and the uptake rate falls to zero. Increasing R_0 above this minimum vesicle size initially leads to a rapid increase in uptake rate. As the vesicle size is further increased, the uptake rate ceases to be signifcantly affected by the stretching penalty and further increases in the vesicle size do not increase the maximal uptake rate.

When the stretching modulus is increased it has the inverse effect to that of increasing the vesicle size, as was previously seen through the relation $a^* \sim \sqrt{\zeta} R_0$. Thus, increasing $1/\sqrt{\lambda}$ has the same effect as increasing R_0. This is seen in figure 2.6d, where decreasing the stretching modulus decreases the stretching penalty for wrapping, increasing the uptake rate in an analogous way to that discussed above for increasing vesicle size. At a sufficiently large stretching modulus, the uptake rate would drop to zero. However, we have not included these points as these values are beyond those seen in typical experimental systems.

In figure 2.7 we have plotted uptake rates as a function of particle size for various attractive energies and bending moduli of the membrane. In contrast to the uptake rate curves shown in figure 2.5, manipulation of the bending modulus of the membrane controls size selectivity by moving the lower particle size limit towards larger particles, shown in figure 2.7a. Thus, a vesicle with bending modulus $\kappa = 5k_BT$ has a minimum particle radius of near $6nm$, in agreement with the estimate $1.52l_c = 6.79nm$ provided by Deserno and Gelbart[60]. Changing the bending modulus to $\kappa = 60k_BT$ gives a minimum particle size of $29nm$ against $1.52l_c = 23.5nm$ and $\kappa = 90k_BT$ gives a minimum particle size of $40nm$ against a corresponding estimate of $1.52l_c = 29nm$. This difference between the estimate of minimum particle size from the phase diagram and that predicted by the uptake kinetics serves to emphasize that the selectivity of particle sizes predicted by the uptake kinetics are not identical with the phase diagram boundaries. Although significantly smaller particles are predicted to bind to the vesicle in equilibrium, the rate of uptake will be vanishingly slow. Nonetheless, the general feature in figure 2.7a is that the selectivity is controlled through the bending modulus mainly by excluding smaller particles from uptake and different bending moduli will have little effect on the upper size limit of particles that can be

wrapped. As with uptake curves shown in figure 2.5, the uptake curves for different bending moduli shown in figure 2.7a a sharp dropoff near the maximum particle size, originating from the same formation of an intermediate minimum in the free energy landscapes of figure 2.4 as discussed above. The position of the optimum particle size (corresponding to the maximum in uptake rate) is quite close to this maximal particle size.

Figure 2.7b shows the uptake rate as a function of particle size for a fixed vesicle size at varying values of the adhesion energy. The adhesion energy is the driving force for wrapping of both small and large particles, characterized by $l_c = \sqrt{\kappa/w}$ and $\zeta = w/\lambda$, respectively. In keeping with this observation, we see that both the upper and lower limit on particle size is controlled by changes in the adhesion energy. Again examining the lower bound on particle size for $w = .125 k_B T/nm^2$ we see that the uptake rate will vanish for $a \approx 10nm$, against an estimate of $1.52 l_c = 19.2nm$. Likewise, for $w = .375 k_B T/nm^2$, the uptake rate vanishes below $a = 17nm$ while $1.52 l_c = 11.1nm$. At maximal particle sizes the estimate provided by $\sqrt{\zeta} R_0$ follows the trend of increasing with increasing w as well. The uptake curves again show the sharp dropoff after the optimal particle as a consequence of the onset of a intermediate

minimum with increasing particle size, as shown in figure 2.4 and discussed above. We note that the adhesion energy is unique in controlling the selectivity of particle size by excluding *both* upper and lower allowable particle sizes, whereas all other features of the system - i.e. vesicle size, bending modulus, and stretching modulus - control either the upper or lower limit alone.

The uptake rates plotted in figure 2.7 show a maximum with increasing particle size, which we defined above to be a^*, with a corresponding maximal uptake rate, which is defined as $1/\tau*$. Figure 2.8 shows these optimal particle sizes and maximal uptake rates as functions of the bending modulus and adhesion strength. In figure 2.8a the optimal particle size is plotted against the bending modulus. As previously observed, the optimal particle size follows the trend of the maximum allowable particle size due to the extremely sharp dropoff in the uptake rate as an intermediate minimum is formed in the free energy. Because the bending modulus has only a minimal effect on the uptake of a large particle, the change in the optimal particle size is correspondingly weak. However, the maximal uptake rate in figure 2.8b shows a marked dependence on the bending modulus, falling off smoothly to zero with increasing bending modulus. For sufficiently large κ, all uptake will be prohibited. This occurs for a $.5\mu m$ vesicle

at a bending stiffness of $60k_BT$, for example. This behavior can be rationalized from the plot of uptake kinetics in figure 2.7a. As the bending modulus increases, the lower allowed particle size increases in a manner roughly proportional to $l_c = \sqrt{\kappa/w}$, while the maximal allowed particle size does not change, not being controlled by the bending modulus. Eventually, the bending modulus can be made stiff enough that l_c is of the same order of $\sqrt{\zeta}R_0$ (the quantity controlling the upper cutoff), and the range of allowed particle sizes goes to zero. It is noteworthy that the Fokker-Planck formalism predicts that this falloff occurs smoothly and is not simply a sudden dropoff. This allows for the possibility to tune the properties of a membrane in order to optimize particle size selectivity and uptake rate over a range of rates, and not simply tune the system to wrap or not wrap a particle in a binary way.

Figure 2.8c shows the optimal particle size as a function of the adhesion energy. In keeping with the above discussion, the optimal particle size follows closely with the maximal allowed particle size, which increases like $\sqrt{\zeta}R_0 \sim \sqrt{w}R_0$. The corresponding maximal uptake rate as a function adhesion energy is shown in figure 2.8d. Clearly, as expected, below some value of the adhesion energy, no uptake will occur. Increasing the adhesion energy initially leads to a rapid increase in uptake rate, which

tapers off at larger and larger values of w. At large values of the adhesion energy, the wrapping process occurs so quickly that the incremental increase in adhesion energy does not proportionally increase the speed of the wrapping process.

2.4 Conclusion

We have used a minimal model based on geometric considerations to compute the kinetics of wrapping a particle by a vesicle. The wrapping process is controlled by the interplay between adhesion energy of the particle to the vesicle and the bending and stretching penalties from changing the geometry. On the basis of these competing factors, the material properties of the membrane dictate a range of particle size which can be wrapped by the membrane. Particles with sizes outside this range will not be wrapped. The lower particle size limit is controlled by the adhesion between the particle and the membrane and the bending stiffness of the membrane and is independent of the stretching modulus or size of the vesicle. An upper limit on the particle size is controlled by the stretching modulus of the membrane(or, equivilently, the size of the vesicle). Within the range of allowed particle sizes we have found an optimum particle size, which we have called a^* at which the uptake rate is maximized. The maximum

uptake rate can be manipulated via changing the properties of the membrane such as bending stiffness, stretching modulus, size of the vesicle and adhesion energy between the vesicle and particle. We find that increase of the stretch modulus or bending stiffness slows down the rate of uptake smoothly to zero. Increasing adhesion energy or the vesicle size increases uptake rate smoothly only up to a point, beyond which additional increases in these parameters have a diminishing effect.

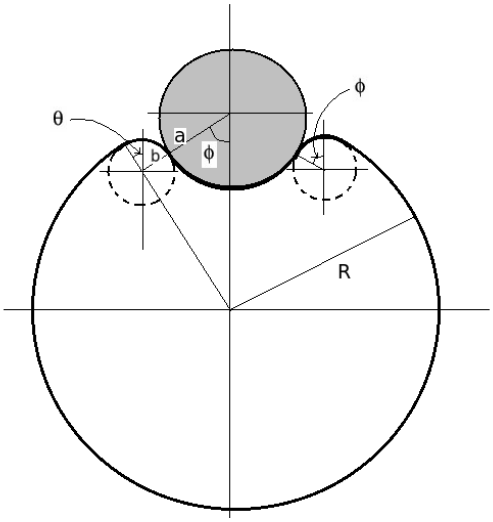

Figure 2.1: Assumed bead vesicle complex geometry.

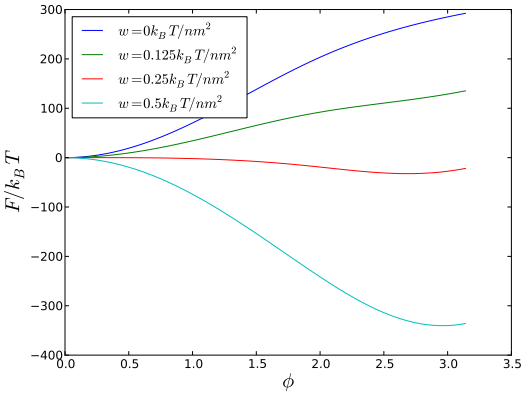

(a) $R_0 = 1\mu m$, $\kappa = 20k_BT$, $\lambda = 50k_BT$.

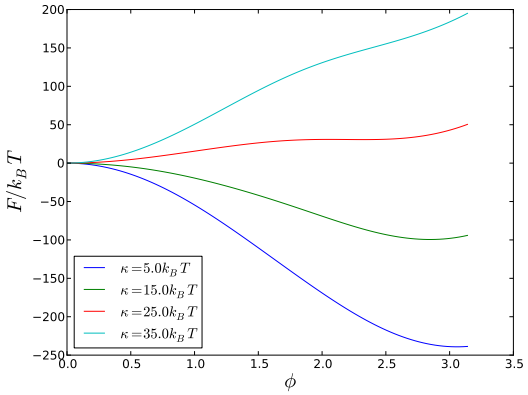

(b) $R_0 = 1\mu m$, $w = .25k_BT/nm^2$, $\lambda = 50k_BT/nm^2$.

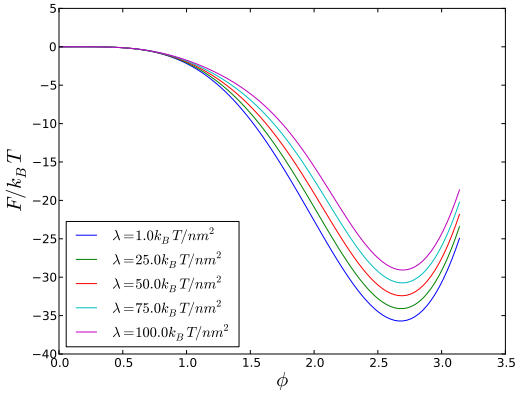

(c) $R_0 = 1\mu m$, $w = .25k_BT/nm^2$, $\kappa = 20k_BT$.

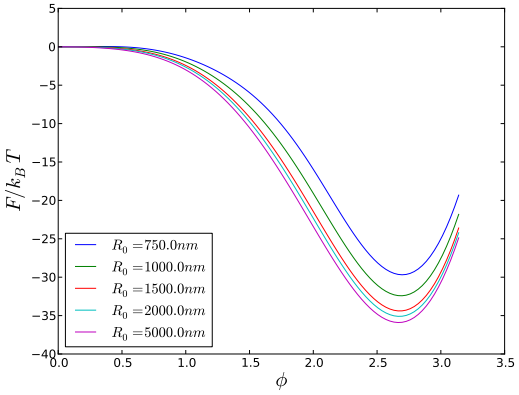

(d) $w = .25k_BT/nm^2$, $\kappa = 20k_BT$, $\lambda = 50k_BT/nm^2$.

Figure 2.2: Free energy landscapes for a small particle, $a = 10nm$.

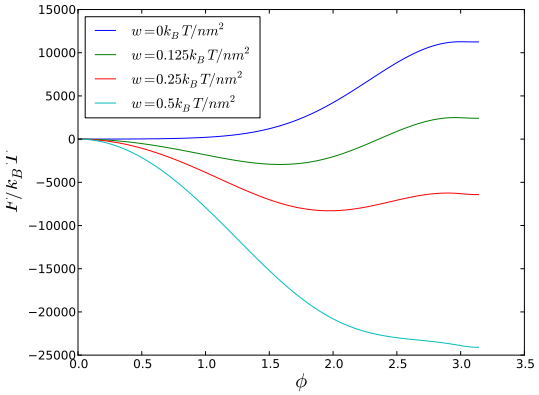

(a) $R_0 = 1\mu m$, $\kappa = 20k_BT$, $\lambda = 50k_BT/nm^2$.

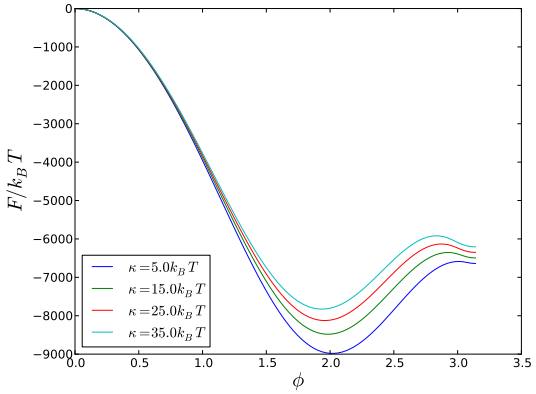

(b) $R_0 = 1\mu m$, $w = .25k_BT/nm^2$, $\lambda = 50k_BT/nm^2$.

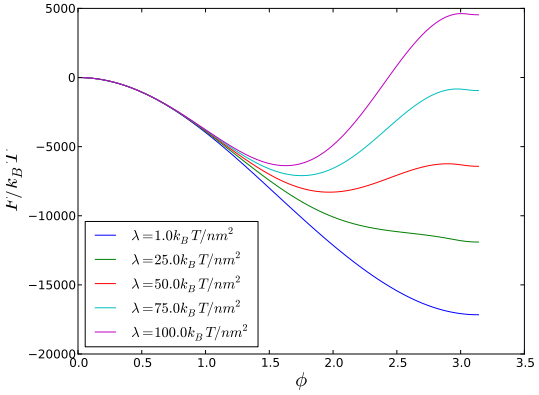

(c) $R_0 = 1\mu m$, $w = .25k_BT/nm^2$, $\kappa = 20k_BT$.

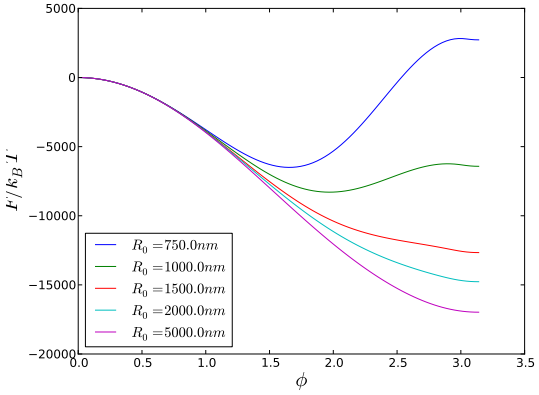

(d) $w = .25k_BT/nm^2$, $\kappa = 20k_BT$, $\lambda = 50k_BT/nm^2$.

Figure 2.3: Free energy landscapes for a large particle, $a = 75nm$.

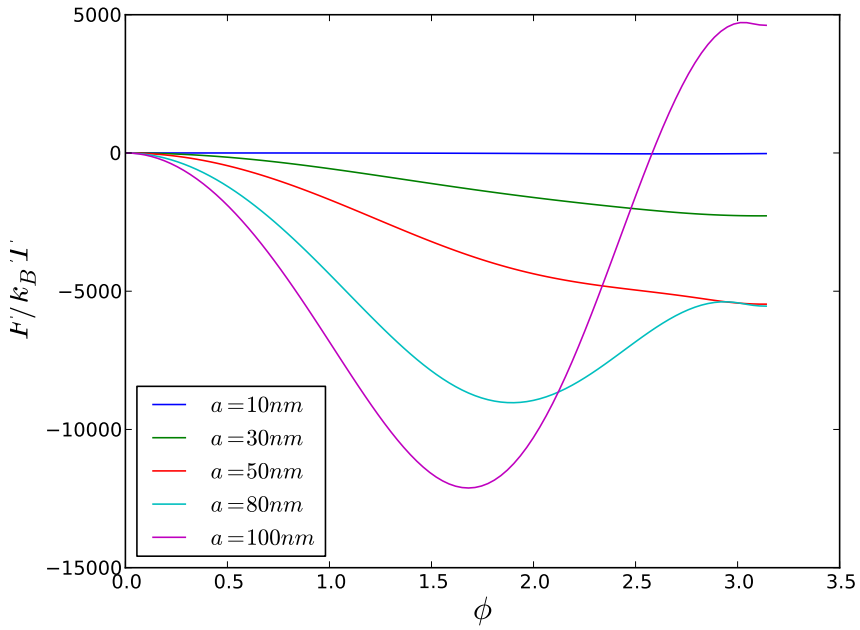

Figure 2.4: Free energy landscape with $R_0 = 1\mu m$, $w = .25k_BT/nm^2$, $\kappa = 20k_BT$, $\lambda = 50k_BT/nm^2$.

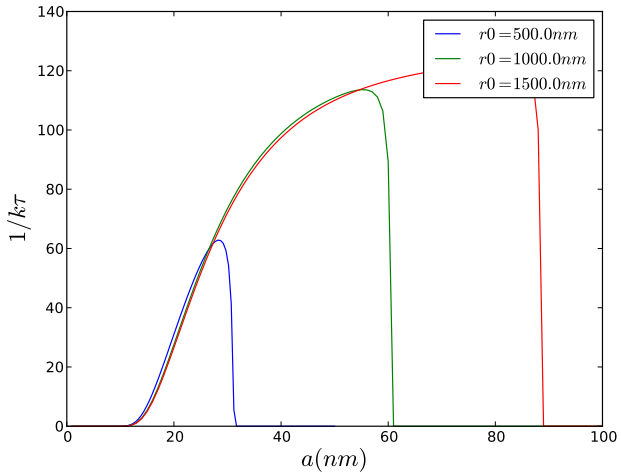

(a) Uptake rate for various values of the vesicle size, R_0 with $w = .25k_BT/nm^2$, $\kappa = 20k_BT$, $\lambda = 50k_BT/nm^2$.

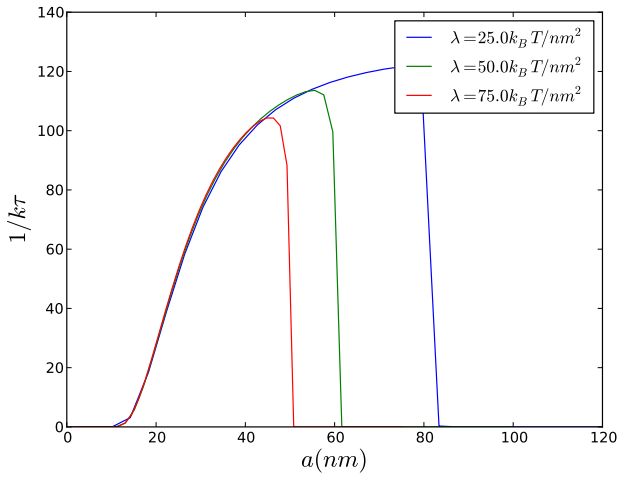

(b) Uptake rate for various values of the stretching modulus, $R_0 = 1\mu m$, $w = .25k_BT/nm^2$, $\kappa = 20k_BT$.

Figure 2.5: Uptake rate for changing vesicle size and stretching modulus.

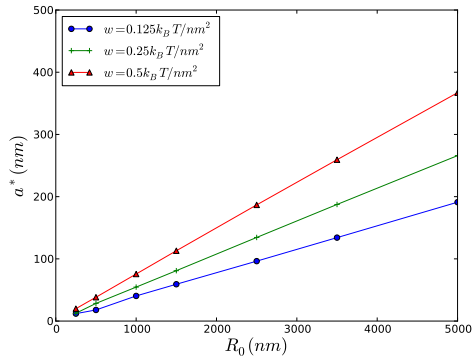

(a) Optimal particle size as a function of vesicle size for various attractive energies with $\kappa = 20k_BT$, $\lambda = 50k_BT/nm^2$.

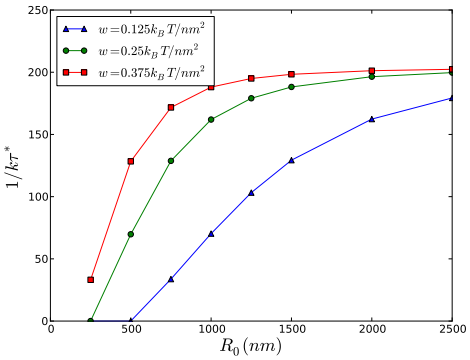

(b) Maximal uptake rate as a function of vesicle size for various attractive energies with $\kappa = 20k_BT$, $\lambda = 50k_BT/nm^2$.

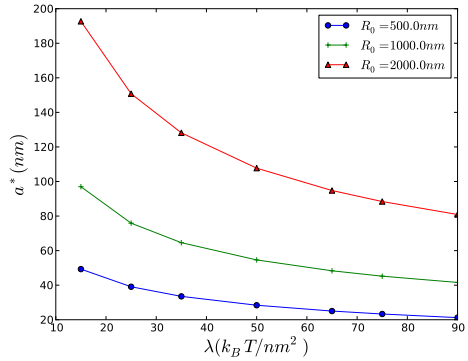

(c) Optimal particle size as a function of stretching modulus at various initial vesicle sizes with $w = .25k_BT/nm^2$, $\kappa = 20k_BT$.

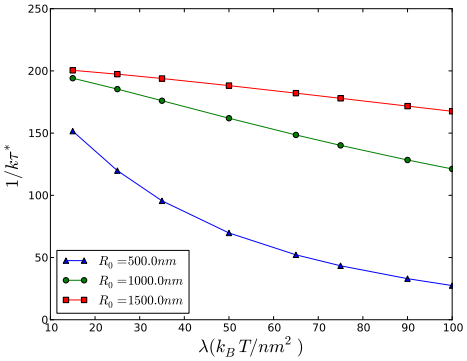

(d) Maximal uptake rate as a function of stretching modulus at various initial vesicle sizes with $w = .25k_BT/nm^2$, $\kappa = 20k_BT$.

Figure 2.6: Optimal particle sizes and associated maximal uptake rates as a function of vesicle size and stretching modulus.

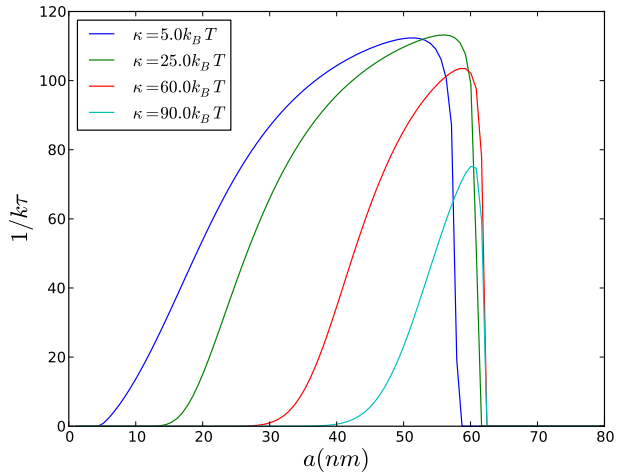

(a) Uptake rate for various values of the bending modulus, $R_0 = 1\mu m$, $w = .25 k_B T/nm^2$, $\lambda = 50 k_B T/nm^2$.

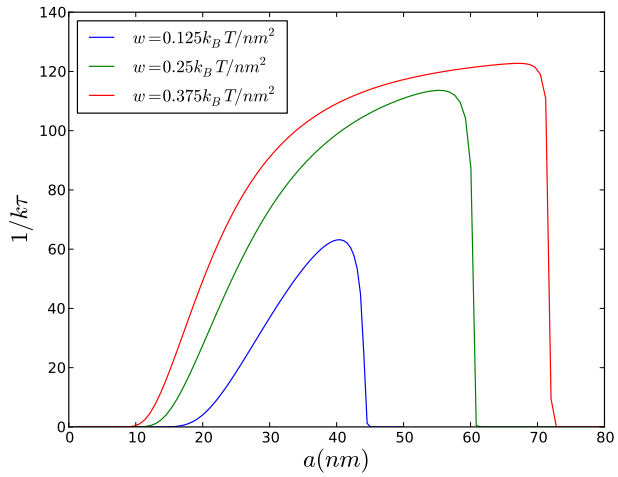

(b) Uptake rate for various values of the attractive energy, $R_0 = 1\mu m$, $\kappa = 20 k_B T$, $\lambda = 50 k_B T/nm^2$.

Figure 2.7: Uptake rate for changing vesicle size and stretching modulus.

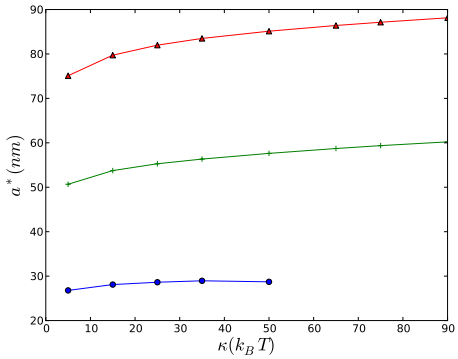

(a) Optimal particle size as a function of the bending modulus with $w = .25k_BT/nm^2$, $\lambda = 50k_BT/nm^2$. $R_0 = .5\mu m$ (blue circles), $1\mu m$ (green crosses), $1.5\mu m$ (red triangles).

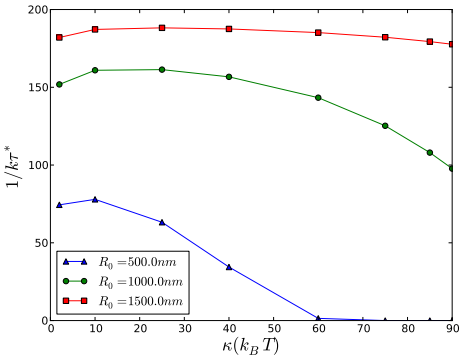

(b) Maximal uptake rate as a function of the bending modulus with $w = .25k_BT/nm^2$, $\lambda = 50k_BT/nm^2$.

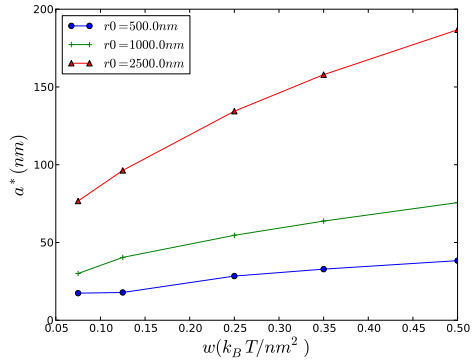

(c) Optimal particle size as a function of the attractive energy with $\kappa = 20k_BT$, $\lambda = 50k_BT/nm^2$.

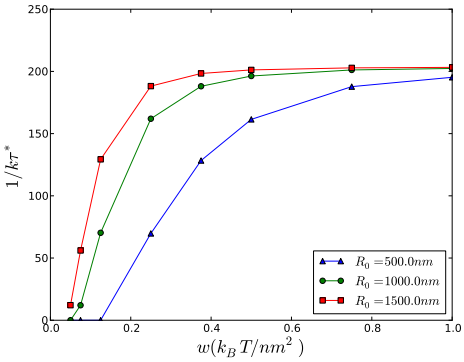

(d) Maximal uptake rate as a function of the attractive energy for various initial vesicle sizes with $\kappa = 20k_BT$, $\lambda = 50k_BT/nm^2$.

Figure 2.8: Optimal particle radius and associated maximal uptake rates for various vesicle sizes as a function of the bending modulus and attractive energy.

CHAPTER 3

DYNAMICS OF INCLUSIONS IN A VISCOELASTIC GEL

3.1 Introduction

The use of a probe particle to explore material properties is a well documented phenomena with a rich history of investigation dating back to the earliest work of Robert Brown observing the motion pollen grains on the surface of water. The underlying physics waited nearly a hundred years for the genius of Einstein to uncover. His discovery of the fluctuation-dissipation theorem connected Brown's observations of the particle motion with the material properties of the fluid. In following work, Einstein showed that the presence of inclusions not only provides information about the material properties, but also modifies the effective material properties, given in his famous formula for the reduced viscosity in the dilute limit: $[\eta] = \frac{5}{2}\phi$, where ϕ is the volume fraction of the particles. The use of microscopic probes to explore the properties of more complex fluids goes back to at least the

1920's[95, 96, 97, 98, 99, 100] and has more recently been widely developed in a more sophisticated way[101, 102, 103, 104, 105, 106].

Mason and Weitz introduced[106] introduced in a phenomenological way the generalized Stokes-Einstein relation(GSER), a time dependent generalization of the classic result. This subsequently motivated Levine and Lubensky to examine the theoretical underpinnings of the GSER[107] in the context of a two fluid model for the gel. They found that the GSER had a frequency range of validity, below which the elastic effects of compressibility became important, and above which the inertial effects of the interstitial fluid dominate the dynamics.

There is a sizable literature related to viscoelastic polymer melts in the context of nanocomposites[108, 109, 110, 111, 112, 113, 114] and a diverse array of biologically relevent systems[115, 116]. Classic work by Hashin and Shtrikman[117, 118] and Mori and Tanaka[119] on elastic composites have been extended to the viscoelastic regime with some success[120]. We employ a single fluid constitutive equation used by Tanaka, et al.[121] to describe the motion of the gel and compute the modification of the material properties up to arbitrary loading fraction for ghost particles. In the zero frequency limit, our model reduces to that of an elastic solid[122], making

it suitable for describing a permanently crosslinked gel. Because the motion of the interstitial fluid is not explicitly accounted for, we expect our results to be valid only for frequencies below the upper limit of the GSER given by Levine and Lubensky.

3.2 Model

We begin with the equation of motion for a viscoelastic gel[121] in the presence of inclusions

$$\rho\ddot{\mathbf{u}}(\mathbf{r},t)-\mu\nabla^2\mathbf{u}(\mathbf{r},t)-(\lambda+\mu)\,\nabla\nabla\cdot\mathbf{u}(\mathbf{r},t)=\mathbf{F}(\mathbf{r},t)-f\dot{\mathbf{u}}(\mathbf{r},t)+\sum_i\int d\mathbf{r}\,\tau_i(\mathbf{r},t) \quad (3.1)$$

Here μ and λ are the usual Lamé constants of a rubber, while f gives the viscous damping due to the presence of solvent and ρ is the density of the medium. On the right hand side, F is an externally applied force field, while τ_i is the force applied to the medium by the i^{th} inclusion. Naturally, this force will be applied only at the surface of the inclusion and, in the case of spherical inclusions with which we are primarily concerned in this paper, we may write $\int d\mathbf{r}\tau_i(\mathbf{r},t) = \int d\Omega_i\tau(\mathbf{R}_i)$ where $\mathbf{R}_i$ is the position of a point on the surface of the bead and Ω_i is the corresponding solid angle with reference to the center of the bead. The solution of this equation is given

by

$$\mathbf{u}(\mathbf{r},t) = \int d\mathbf{r}'dt'\,\mathbb{G}(\mathbf{r}-\mathbf{r}',t-t')\cdot\mathbf{F}(\mathbf{r}',t') + \int d\Omega dt'\mathbb{G}(\mathbf{r}-\Omega',t-t')\tau_i(\Omega,t') + \sum_{j\neq i}\int d\Omega' dt'\mathbb{G}(\mathbf{r}-\Omega',t-t')\tau_j(\Omega',t') \quad (3.2)$$

with $\mathbb{G}(\mathbf{r},t)$ given by

$$\mathbb{G}(\mathbf{r},t) = \int \frac{d^3\mathbf{k}}{(2\pi)^3}\frac{d\omega}{2\pi}\exp(i\mathbf{k}\cdot\mathbf{r})\exp(i\omega t)\mathbb{G}(\mathbf{k},\omega) \quad (3.3)$$

where

$$\mathbb{G}(\mathbf{k},\omega) = \frac{\mathbb{I}-\hat{\mathbf{k}}\hat{\mathbf{k}}}{-\rho\omega^2 - i\omega f + \mu k^2} + \frac{\hat{\mathbf{k}}\hat{\mathbf{k}}}{-\rho\omega^2 - i\omega f + (\lambda+2\mu)k^2} \quad (3.4)$$

and $\hat{\mathbf{k}}$ is a unit vector in the $\mathbf{k}$ direction.

The form of equation (3.2) has the following intuitive interpretation: a force impinging on the medium at a point $\mathbf{r}'$ at time t' is communicated by the tensor $\mathbb{G}$ to the point $\mathbf{r}$ resulting in a displacement $\mathbf{u}$ at time t. When inclusions are present, the imposed force will also result in a displacement field at the boundary of the particle. This displacement of the embedding matrix is communicated to the particle itself via boundary conditions, resulting in a force on the bead. This force gives rise to a displacement of the points on the beads surface which is then communicated to a force

on the matrix, which is then communicated to the ultimate point $\mathbf{r}$ via $\mathbb{G}$ contributing to the resulting displacement at time t. Thus there are two contributions to the ultimate displacement: one directly communicated via $\mathbb{G}$ and a second contribution coming from *scattering* off of the inclusion. The scattering off of a single particle is communicated via the scattering tensor, which we will name $\mathbb{T}$ and which we shall explore presently. Of course, in the presence of multiple inclusions we must include not only single scattering events, but scattering from two particles, three particles and so on to all orders, giving rise to a series in powers of $\mathbb{T}$.

In order to calculate the scattering operator, we recall the displacement of the bead is controlled by the displacement of the gel at the surface of the bead and the boundary condition. In general at the boundary of the i^{th} particle we will have

$$\mathbf{u}(\mathbf{R}_i, t) = \mathbb{A} \cdot \mathbf{x}_i(\Omega, t) \tag{3.5}$$

For the present we limit our considerations to stick boundary conditions, for which the tensor $\mathbb{A}$ is simply the identity. $\mathbf{x}$ is the displacement of a point on the surface of the bead. Solving equation (3.1) utilizing equation (3.29) at the surface of the bead and plugging in equation (3.5) we obtain

$$\mathbf{x}(\Omega,t) = \int d\mathbf{r}'dt'\,\mathbb{G}(\mathbf{R}(\Omega)-\mathbf{r}',t-t')\cdot\mathbf{F}(\mathbf{r}',t') + \int d\Omega'dt'\,\mathbb{G}(\mathbf{R}(\Omega)-\mathbf{R}(\Omega'))\cdot\tau_i(\Omega',t') + \sum_{j\neq i}\int d\Omega'dt'\mathbb{G}(\mathbf{R}_i(\Omega)-\mathbf{R}_j(\Omega'),t-t')\cdot\tau_j(\Omega',t') \quad (3.6)$$

In order to solve for $\tau_i(\Omega,t)$ we define the inverse Green's function on the surface of the i^{th} bead by

$$\int d\Omega''dt''\,\mathbb{G}^{-1}(\mathbf{R}_i(\Omega)-\mathbf{R}_i(\Omega''),t-t'')\cdot\mathbb{G}(\mathbf{R}_i(\Omega'')-\mathbf{R}_i(\Omega'),t''-t') = \delta(\mathbf{R}_i(\Omega)-\mathbf{R}_i(\Omega'))\delta(t-t') \quad (3.7)$$

Applying equation (3.7) to equation (3.6) we find

$$\tau_i(\Omega,t) = \int d\Omega'dt'\,\mathbb{G}^{-1}_{\Omega,\Omega'}(t-t')\cdot\mathbf{x}_i(\Omega',t') - \int d\Omega'd\mathbf{r}''dt'dt''\,\mathbb{G}^{-1}_{\Omega,\Omega'}(t-t')\cdot\mathbb{G}(\mathbf{R}(\Omega')-\mathbf{r}'',t'-t'')\cdot\mathbf{F}(\mathbf{r}'',t'') - \sum_{j\neq i}\int d\Omega'd\Omega''dt'dt''\mathbb{G}^{-1}_{\Omega,\Omega'}\cdot\mathbb{G}(\mathbf{R}_i(\Omega')-\mathbf{R}_j(\Omega''),t'-t'')\cdot\tau_j(\Omega'',t'') \quad (3.8)$$

We must now solve for the position of the bead $\mathbf{x}_i(\Omega,t)$ using the equation of motion of the bead, given by Newton's second law

$$m\ddot{\mathbf{x}}_i^0(t) = -\int d\Omega\, \tau_i(\Omega, t) - \mathbf{F}_{ext,i}(t) \tag{3.9a}$$

$$I\ddot{\theta}_i(t) = -\int d\Omega\, \mathbf{a}_i(\Omega) \times \tau_i(\Omega, t) - N_{ext,i} \tag{3.9b}$$

$\mathbf{x}_i^0(t)$ is the displacement of the center of the bead and $\theta_i(\Omega, t)$ is the angular displacement, while $\mathbf{a}_i(\Omega)$ is the vector from the center to a point on the surface, so that the total displacement of a point on the surface is $\mathbf{x}_i(\Omega, t) = \mathbf{x}_i^0(t) + \theta_i \times \mathbf{a}_i(\Omega, t)$. $\mathbf{F}_{ext,i}$ and $\mathbf{N}_{ext,i}$ are the externally applied force and torque to the bead by, e.g., laser tweezers or a magnetic pulse. Now applying equations (3.9a) and (3.9b) to equation (3.8) and ignoring the inertia of the bead we obtain

$$\begin{aligned}\int \zeta_{TT}(t-t') \cdot \mathbf{x}_i^0(t') + \int \zeta_{TR}(t-t') \cdot \theta_i(t') \\ = \int \mathbb{G}^{-1}_{\Omega,\Omega'}(t-t') \cdot \mathbb{G}(\mathbf{R}_i(\Omega') - \mathbf{r}'', t'-t'') \cdot \mathbf{F}(\mathbf{r}'', t'') - \mathbf{F}_{ext,i}\end{aligned} \tag{3.10}$$

$$\begin{aligned}\int \zeta_{RT}(t-t') \cdot \mathbf{x}_i^0(t') + \int \zeta_{RR}(t-t') \cdot \theta_i(t') \\ = \int \mathbf{a}_{\Omega,i} \times \mathbb{G}^{-1}_{\Omega,\Omega'}(t-t') \cdot \mathbb{G}(\mathbf{R}_i(\Omega) - \mathbf{r}'', t'-t'') \cdot \mathbf{F}(\mathbf{r}'', t'') - \mathbf{N}_{ext,i}\end{aligned} \tag{3.11}$$

The variables over which the integration occurs should be evident and we have dropped them for clarity. The ζ coefficients are defined by

$$\zeta_{TT}(t-t') = \int d\Omega d\Omega' \, \mathbb{G}^{-1}_{\Omega,\Omega'}(t-t') \tag{3.12a}$$

$$\zeta_{TR}(t-t') = \int d\Omega d\Omega' \, \mathbb{G}^{-1}_{\Omega,\Omega'}(t-t') \times \mathbf{a}(\Omega') \tag{3.12b}$$

$$\zeta_{RT}(t-t') = \int d\Omega d\Omega' \, \mathbf{a}(\Omega) \times \mathbb{G}^{-1}_{\Omega,\Omega'} \tag{3.12c}$$

$$\zeta_{RR}(t-t') = \int d\Omega d\Omega' \, \mathbf{a}(\Omega) \times \mathbb{G}^{-1}_{\Omega,\Omega'} \times \mathbf{a}(\Omega') \tag{3.12d}$$

For spherical inclusions $\zeta_{TR} = \zeta_{RT} = 0$ by symmetry. In the absence of a force field applied to the gel($\mathbf{F}(\mathbf{r},t) = 0$) we see that ζ_{TT} is the response function of a single bead to an externally applied force. Solving equations (3.10) for $\mathbf{x}_i^0$ and θ_i we may replace $\mathbf{x}_i$ in equation (3.8)to obtain

$$\begin{aligned}\tau_i(\Omega,t) = -\int \Big\{ &\mathbb{G}^{-1}_{\Omega,\Omega'}(t-t') - \int d\Omega_p d\Omega_q \mathbb{G}^{-1}_{\Omega,\Omega_p}(t-t')\zeta^{-1}_{TT}(t'-t'')\mathbb{G}^{-1}_{\Omega_q,\Omega'}(t''-t''') \\ &- \int d\Omega_p d\Omega_q \mathbb{G}^{-1}_{\Omega,\Omega_p}(t-t'') \times \mathbf{a}(\Omega_p) \cdot \zeta^{-1}_{RR}(t''-t''') \cdot \mathbf{a}(\Omega_q) \times \mathbb{G}^{-1}_{\Omega_q,\Omega'}(t'''-t') \Big\} \\ &\cdot \int \mathbb{G}(\mathbf{R}(\Omega') - \mathbf{r}_p, t'-t_p) \cdot \mathbf{F}(\mathbf{r}_p,t_p) \\ &- \sum_{j\neq i} \int \mathbb{G}^{-1}_{\Omega_i,\Omega_i'} \cdot \mathbb{G}_{\Omega_i',\Omega_j}(t'-t'') \cdot \tau_j(\Omega_j,t'')\end{aligned} \tag{3.13}$$

Integrations that are not specified are taken over all repeated arguments. By using the boundary conditions and the equation of motion for the bead, we have now obtained an expression for τ in terms of the force field imposed on gel, the Green's function and

it's inverse. When we plug this into equation (3.29) we obtain a solution to equation (3.1) in the presence of inclusions.

$$\begin{aligned}\mathbf{u}(\mathbf{r},t) = &\int \mathbb{G}(\mathbf{r}-\mathbf{r}',t-t')\cdot\mathbf{F}(\mathbf{r}',t') \\ &+ \int \mathbb{G}(\mathbf{r}-\mathbf{r}',t-t')\cdot\mathbb{T}_i(\mathbf{r}'-\mathbf{r}'',t'-t'')\cdot\mathbb{G}(\mathbf{r}''-\mathbf{r}''',t''-t''')\cdot\mathbf{F}(\mathbf{r}''',t''') \\ &- \sum_{j\neq i}\mathbb{G}^{-1}_{\Omega_i,\Omega_i'}(t-t')\cdot\mathbb{G}_{\Omega_i',\Omega_j}(t'-t'')\cdot\tau_j(\Omega_j,t'') \quad (3.14)\end{aligned}$$

The scattering operator is defined by

$$\mathbb{T}_i(\mathbf{r}-\mathbf{r}',t-t') = -\int \delta[\mathbf{r}-\mathbf{R}(\Omega)]\mathbb{T}_i(\Omega_i,\Omega_i';t-t')\delta[\mathbf{r}-\mathbf{R}(\Omega')] \quad (3.15)$$

and

$$\begin{aligned}\mathbb{T}_i(\Omega_i,\Omega_i';t-t') = \mathbb{G}^{-1}_{\Omega_i,\Omega_i'}(t-t') - &\int d\Omega_i^{(p)}d\Omega_i^{(q)}\mathbb{G}^{-1}_{\Omega_i,\Omega_i^{(p)}}(t-t'')\cdot\zeta^{-1}_{TT}(t''-t''')\cdot\mathbb{G}^{-1}_{\Omega_i^{(q)},\Omega_i'}(t'''-t') \\ - \int d\Omega_i^{(p)}d\Omega_i^{(q)}\mathbb{G}^{-1}_{\Omega_i,\Omega_i^{(p)}}(t-t'')\times\mathbf{a}(\Omega_i^{(p)})\cdot\zeta^{-1}_{RR}(t''-t''')\cdot\mathbf{a}(\Omega_i^{(q)})\times\mathbb{G}_{\Omega_i^{(q)},\Omega_i'}(t'''-t') \\ &(3.16)\end{aligned}$$

By iterating this procedure for all the τ_j the solution of equation (3.14) is written as a scattering sequence

$$\langle\mathbf{u}(\mathbf{r},t)\rangle = \int \mathbb{G}\left[\mathbb{I}+\sum_i\langle\mathbb{T}_i\rangle+\sum_{i,j\neq i}\langle\mathbb{T}_i\mathbb{G}\mathbb{T}_j\rangle+\sum_{i,j\neq i,k\neq j}\langle\mathbb{T}_i\mathbb{G}\mathbb{T}_j\mathbb{G}\mathbb{T}_k\rangle+...\right]\mathbb{G}\mathbf{F} \quad (3.17)$$

We have dropped all variables in order to highlight the character of the scattering sequence. The angular brackets denote an average taken over the positions of the inclusions since it is an ensemble average displacement field which we are interested in. Thus we see that the displacement field involves the correlations of all the particles to all orders of concentration.

3.2.1 Self Energy

3.2.1.1 Material Properties

In order to calculate the modification of material properties due to the presence of inclusions, we return to equation (3.1). Averaging over the positions of all the inclusions, we define the self energy tensor Σ by

$$\int d\mathbf{r}'dt'\,\Sigma(\mathbf{r}-\mathbf{r}',t-t')\cdot\langle\mathbf{u}(\mathbf{r}',t')\rangle = \left\langle\sum_i\int d\mathbf{r}\,\delta(\mathbf{r}-\mathbf{R}_i)\tau(\mathbf{r},t)\right\rangle \tag{3.18}$$

The averaged equation of motion then becomes

$$\rho\langle\ddot{\mathbf{u}}\rangle + f\langle\dot{\mathbf{u}}\rangle - \mu\nabla^2\cdot\langle\mathbf{u}\rangle - (\lambda+\mu)\nabla\nabla\cdot\langle\mathbf{u}\rangle = \mathbf{F} + \Sigma * \langle\mathbf{u}\rangle \tag{3.19}$$

Where the $*$ represents the appropriate convolution integral and we have dropped function arguments for the sake of clarity. Translating into Fourier space and fre-

quency we have

$$-\rho\omega^2\langle\tilde{\mathbf{u}}\rangle - i\omega f\langle\tilde{\mathbf{u}}\rangle + \mu k^2\mathbb{I}\cdot\langle\tilde{\mathbf{u}}\rangle + (\lambda+\mu)k^2\,\hat{\mathbf{k}}\hat{\mathbf{k}}\cdot\langle\tilde{\mathbf{u}}\rangle - \tilde{\Sigma}\cdot\langle\tilde{\mathbf{u}}\rangle = \tilde{\mathbf{F}} \tag{3.20}$$

A tilde simply denotes the Fourier transform in space and time, given by equation (3.3). We rewrite the equation as the superposition of terms parallel and perpendicular to $\mathbf{k}$

$$(-\rho\omega^2 - i\omega f + \mu k^2 - \Sigma_\perp)(\mathbb{I} - \hat{\mathbf{k}}\hat{\mathbf{k}})\cdot\tilde{\mathbf{u}} + (-\rho\omega^2 - i\omega f + (\lambda+2\mu)k^2 - \Sigma_\parallel)\,\hat{\mathbf{k}}\hat{\mathbf{k}}\cdot\tilde{\mathbf{u}} = \tilde{\mathbf{F}} \tag{3.21}$$

Expanding $\Sigma(\mathbf{k},\omega)$ in powers of $\mathbf{k}$ we see that in the limit $k \to 0$ the corrections to the moduli of the gel will be given by the k^2 term in the series.

$$\mu - \mu(\omega) = \lim_{k\to 0}\frac{d}{dk^2}\Sigma_\perp(\mathbf{k},\omega) \tag{3.22a}$$

$$\lambda - \lambda(\omega) = \lim_{k\to 0}\frac{d}{dk^2}[\Sigma_\parallel(\mathbf{k},\omega) - 2\Sigma_\perp(\mathbf{k},\omega)] \tag{3.22b}$$

3.2.1.2 Computation of the Self Energy

The solution to equation (3.21) is given by

$$\langle\mathbf{u}(\mathbf{r},t)\rangle = \int \mathbb{G} * \mathbf{F}(\mathbf{r}',t') + \int \mathbb{G} * \Sigma * \mathbf{u} \tag{3.23}$$

By iterating this equation we obtain a different scattering solution for $\langle \mathbf{u} \rangle$

$$\langle \mathbf{u} \rangle = [\mathbb{I} + \mathbb{G} * \Sigma + \mathbb{G} * \Sigma * \mathbb{G} * \Sigma + ...] * \mathbb{G} * \mathbf{F} \tag{3.24}$$

Thus we obtain a "top down" scattering series for the averaged displacement field in the gel. We wish to compare this solution with the "bottom up" solution arrived at in equation (3.17) in order to make a connection between the self energy and the scattering operator. To do this, we note that the self energy tensor will include contributions from all scattering orders, inviting us to write it as the sum of these contributions

$$\Sigma = \sum_p a_p \tag{3.25}$$

Where a_p is the contribution due to p scattering events. In equation (3.17) each $\mathbb{T}$ operator represents one scattering event, and so the number of scattering events is simply given by the number of operators in each term. By inserting equation (3.25) into equation (3.24) and comparing terms with the same number of scattering events we obtain

$$
\begin{aligned}
a_1 &= \sum_i \langle \mathbb{T}_i \rangle \\
a_2 &= \sum_i \sum_{j \neq i} \langle \mathbb{T}_i \mathbb{G} \mathbb{T}_j \rangle - \langle \mathbb{T}_i \rangle \mathbb{G} \langle \mathbb{T}_j \rangle \\
a_3 &= \sum_i \sum_{j \neq i} \sum_{k \neq j} \langle \mathbb{T}_i \mathbb{G} \mathbb{T}_j \mathbb{G} \mathbb{T}_k \rangle - \langle \mathbb{T}_i \rangle \mathbb{G} \langle \mathbb{T}_j \mathbb{G} \mathbb{T}_k \rangle - \langle \mathbb{T}_i \mathbb{G} \mathbb{T}_j \rangle \mathbb{G} \langle \mathbb{T}_k \rangle + \langle \mathbb{T}_i \rangle \mathbb{G} \langle \mathbb{T}_j \rangle \mathbb{G} \langle \mathbb{T}_k \rangle \\
&\vdots
\end{aligned}
\tag{3.26}
$$

In the dilute limit, which will be important later, $\Sigma \approx a_1 = \sum_i \langle \mathbb{T}_i \rangle = N \langle \mathbb{T}_i \rangle$, where the last step is true for identical particles.

In order compute the modulus at higher concentrations we must expand the self energy in a virial series of the form

$$
\Sigma = b_0 + b_1 c + b_2 c^2 + ... \tag{3.27}
$$

Examining the a_i's in equation (3.26) it is clear that the first virial coefficient(scattering from a single particle) will simply be $b_1 = a_1$. The second order virial coefficient will contain terms from all a_i with $i > 1$ involving only two particles, the third order term all a_i involving three particles and so on, so that for example

$$b_2 = \sum_{\alpha} \sum_{\beta \neq \alpha} \langle \mathbb{T}_\alpha \mathbb{G} \mathbb{T}_\beta \rangle - \langle \mathbb{T}_\alpha \rangle \mathbb{G} \langle \mathbb{T}_\beta \rangle + \langle \mathbb{T}_\alpha \mathbb{G} \mathbb{T}_\beta \mathbb{G} \mathbb{T}_\alpha \rangle - \langle \mathbb{T}_\alpha \mathbb{G} \mathbb{T}_\beta \rangle \mathbb{G} \langle \mathbb{T}_\alpha \rangle - ... \quad (3.28)$$

We may compute the contribution to the self energy of arbitrarily large orders in concentration by performing the indicated cluster integrals in equation (3.28) and summing the infinite series. In practice, this is laborious. We will introduce a further assumption later to extend our results to arbitrary filling fraction. We begin by further examining the scattering operator $\mathbb{T}$.

3.2.2 Scattering Operator

For the present we consider only one particle so that the solution to (3.1) is

$$\mathbf{u}(\mathbf{r}, t) = \int d\mathbf{r}' dt' \, \mathbb{G}(\mathbf{r} - \mathbf{r}', t - t') \cdot \mathbf{F}(\mathbf{r}', t') + \int d\Omega dt' \, \mathbb{G}(\mathbf{r} - \mathbf{R}(\Omega)) \cdot \tau(\Omega, t') \quad (3.29)$$

Performing the mathematical manipulations of the first section and explicitly writing the average over particle positions while going to Fourier space, we find from equation (3.16)

$$\mathbb{T}(\mathbf{k},\omega) = -\int d(\mathbf{r}-\mathbf{r}')d(t-t')\left\{\frac{1}{V}\int d\mathbf{R}^0\int d\Omega d\Omega'\delta[\mathbf{r}-(\mathbf{R}^0+\mathbf{a}(\Omega))]\right.$$
$$\left.\times\,\mathbb{T}(\Omega,\Omega';t-t')\delta[\mathbf{r}'-(\mathbf{R}^0+\mathbf{a}(\Omega'))]\right\} \tag{3.30}$$
$$\times\exp[i\mathbf{k}\cdot(\mathbf{r}-\mathbf{r}')]\exp[i\omega(t-t')]$$
$$= -\frac{1}{V}\int d\Omega d\Omega'\exp[i\mathbf{k}\cdot(\mathbf{a}(\Omega)-\mathbf{a}(\Omega'))]\mathbb{T}(\Omega,\Omega';\omega)$$

We may now expand the two parts of this integrand in terms of the surface harmonics ofthe inclusion, in our case spherical harmonics and spherical bessel functions[123]. We use the expansions

$$\exp[i\mathbf{k}\cdot\mathbf{a}(\Omega)] = 4\pi\sum_{pq} i^p j_p(ka)Y^*_{pq}(\Omega)Y_{pq}(\Omega_k) \tag{3.31}$$

and

$$\mathbb{T}(\Omega,\Omega';\omega) = \sum_{l,l'=0}^{\infty}\sum_{\substack{m=-l\\m'=-l'}}^{l,l'} Y_{lm}(\Omega)Y^*_{l'm'}(\Omega')\mathbb{T}_{lm;l'm'}(\omega) \tag{3.32}$$

Inserting these expansions into equation (3.30) gives

$$\mathbb{T}(\mathbf{k},\omega) = -\frac{(4\pi)^2}{V}\sum_{lm;l'm'}(-1)^{l'}i^{l+l'}j_l(ka)j_{l'}(ka)\mathbb{T}_{lm;l'm'}(\omega)Y_{lm}(\Omega_k)Y_{l'm'}(\Omega_k) \tag{3.33}$$

The spherical symmetry of the problem allows us to choose $\mathbf{k} = k\hat{z}$ in an isotropic medium so that we are concerned only with the $m = m' = 0$ coefficients[123]. A

further simplification is realized by recalling that we are interested only in the k^2 term and so only terms with $l + l' \leq 2$ contribute due to the spherical bessel functions. Accounting for numerical factors we find up to order k^2

$$\begin{aligned}\mathbb{T}(k,\omega) = -\frac{4\pi}{V}\Big\{ & j_0^2(ka)\mathbb{T}_{00;00}(\omega) - i\sqrt{3}j_0(ka)j_1(ka)\mathbb{T}_{00;10}(\omega) \\ & - \sqrt{5}j_0(ka)j_2(ka)\mathbb{T}_{00;20}(\omega) + 3j_1^2(ka)\mathbb{T}_{10;10}(\omega) \\ & + i\sqrt{3}j_1(ka)j_0(ka)\mathbb{T}_{10;00}(\omega) - \sqrt{5}j_2(ka)j_0(ka)\mathbb{T}_{20;00}(\omega)\Big\} \end{aligned} \quad (3.34)$$

We must now compute these coefficients. Expanding $\mathbb{G}(\mathbf{k},\omega)$ as in equation (3.32) and recalling the definition of $\mathbb{T}$ we find that

$$\begin{aligned}\mathbb{T}_{lm;l'm'}(\omega) = & \mathbb{G}^{-1}_{lm;l'm'}(\omega) - \mathbb{G}^{-1}_{lm;00}(\omega)\cdot\zeta^{-1}_{TT}(\omega)\cdot\mathbb{G}^{-1}_{00;l'm'}(\omega) \\ & + \sum_{\mu,\mu'\geq -1}^{1}\left(\mathbb{G}^{-1}_{lm;1\mu}(\omega)\times\mathcal{Y}^*_{\mu}\right)\cdot\zeta^{-1}_{TT}(\omega)\cdot\left(\mathcal{Y}_{\mu'}\times\mathbb{G}^{-1}_{1\mu';l'm'}\right) \end{aligned} \quad (3.35)$$

where $\mathcal{Y}_{lm}$ is defined by

$$\begin{aligned}\mathcal{Y}_{lm} &= \int d\Omega\, \mathbf{a}(\Omega)Y_{lm}(\Omega) \\ &= \sqrt{\frac{2\pi}{3}}a\delta_{l1}\left[(\delta_{m,-1}-\delta_{m1})\hat{\mathbf{x}} - i(\delta_{m,-1}+\delta_{m1})\hat{\mathbf{y}} + \sqrt{2}\delta_{m0}\hat{\mathbf{z}}\right] \\ &\equiv \delta_{1l}\mathcal{Y}_m \end{aligned} \quad (3.36)$$

In order to compute the necessary coefficients in equation (3.34) we must compute the expansion coefficients of $\mathbb{G}$ and then invert these tensor quantities and insert them into equation (3.35) to obtain the frequency dependent moduli of the gel via equation (3.22). We also note that the response function of the inclusion to an external force or torque is given by the inverses of

$$\zeta_{TT}(\omega) = 4\pi \mathbb{G}^{-1}_{00;00}(\omega) \tag{3.37}$$

and

$$\zeta_{RR}(\omega) = \sum_{\mu,\mu' \geq -1}^{1} \mathcal{Y}_{\mu} \times \mathbb{G}^{-1}_{1\mu;1\mu'}(\omega) \times \mathcal{Y}^{*}_{\mu'} \tag{3.38}$$

3.2.2.1 Computation of the coefficients

Expanding $\mathbb{G}$ on the surface of the inclusion as in equation (3.32), the coefficients are given by

$$\mathbb{G}_{lm;l'm'}(\omega) = \int d\Omega d\Omega' \mathbb{G}(\mathbf{R}(\Omega) - \mathbf{R}(\Omega'); \omega) Y^{*}_{lm}(\Omega) Y_{l'm'}(\Omega') \tag{3.39}$$

Inserting equation (3.31) into equations (3.4) and (3.3) this becomes

$$\mathbb{G}_{lm;l'm'}(\omega) = (-1)^{l'} i^{l+l'} \frac{2}{\pi} \int dk d\Omega_k \, k^2 \mathbb{G}(k, \omega) j_l(ka) j_{l'}(ka) Y^{*}_{lm}(\Omega_k) Y_{l'm'}(\Omega_k) \tag{3.40}$$

Inserting $\mathbb{G}(\mathbf{k},\omega)$ from equation (3.4) and expanding the tensor $\hat{\mathbf{k}}\hat{\mathbf{k}} = \frac{1}{3}\mathbb{I} + \sum_{p=-2}^{2} \mathbb{I}_p Y_{2p}(\Omega_k)$ gives

$$\mathbb{G}_{lm;l'm'}(\omega) = \frac{1}{\mu a}[\alpha_{ll'}(\omega) + \frac{1}{3}\beta_{ll'}(\omega)]\delta_{ll'}\delta_{mm'}\mathbb{I} + \frac{1}{\mu a}\beta_{ll'}(\omega)\sum_{p=-2}^{2}\mathbb{I}_p \int d\Omega_k Y_{2p}(\Omega_k) Y^*_{lm}(\Omega_k) Y_{l'm'}(\Omega_k) \tag{3.41}$$

The angular integral over the triple spherical harmonics imposes the constraint that $|l - l'| \leq 2$ and that $m - m' = p$. The tensors $\mathbb{I}_p$ are defined by[124]

$$\begin{aligned}
\mathbb{I}_0 &= -\frac{2}{3}\sqrt{\frac{\pi}{5}}\begin{pmatrix} 1 & 0 & 0 \\ 0 & 1 & 0 \\ 0 & 0 & -2 \end{pmatrix} \\
\mathbb{I}_1 &= -\sqrt{\frac{2\pi}{15}}\begin{pmatrix} 0 & 0 & 1 \\ 0 & 0 & -i \\ 1 & -i & 0 \end{pmatrix} \\
\mathbb{I}_2 &= -\sqrt{\frac{2\pi}{15}}\begin{pmatrix} -1 & i & 0 \\ i & 1 & 0 \\ 0 & 0 & 0 \end{pmatrix}
\end{aligned} \tag{3.42}$$

and $\mathbb{I}_{-p} = (-1)^p \mathbb{I}^*_p$. The functions $\alpha_{ll'}(\omega)$ and $\beta_{ll'}(\omega)$ are given by

$$\alpha_{ll'}(\omega) = \mu a(-1)^{l'} i^{l+l'} \int_0^\infty dk\, j_l(ka) j_{l'}(ka) \frac{k^2}{-\rho\omega^2 - i\omega f + \mu k^2} \tag{3.43}$$

$$\approx (-1)^{l'} i^{l+l'} \int_0^\infty dx\, j_l(x) j_{l'}(x) \frac{x^2}{-i\omega\tau + x^2} \tag{3.44}$$

$$\beta_{ll'}(\omega) = \mu a(-1)^{l'} i^{l+l'} \int_0^\infty dk\, j_l(ka) j_{l'}(ka) \frac{(\lambda+\mu)k^4}{(-\rho\omega^2 - i\omega f + \mu k^2)(-\rho\omega^2 - i\omega f + (\lambda+2\mu)k^2)} \tag{3.45}$$

$$\approx (-1)^{l'} i^{l+l'} \frac{\lambda+\mu}{\lambda+2\mu} \int_0^\infty dx\, j_l(x) j_{l'}(x) \frac{x^4}{(-i\omega\tau + x^2)(-i\omega\tau' + x^2)} \tag{3.46}$$

The modes of the system are given by the poles of the integrands in equations (3.43). These are given by $\omega = \frac{-if \mp \sqrt{-f^2 + Gk^2\rho}}{2\rho}$ where G is the appropriate modulus. The system will be overdamped when $f > \sqrt{Gk^2\rho}$. Dropping the inertial terms amounts to assuming that the system is overdamped. For typical experimental systems $\rho \approx$ 20mg/mL, $\mu \approx$ 1Pa, and $k \approx 1/a \approx .5\mu$m[125] so that our approximation will be valid for $f < 9 \times 10^6 \text{kg/m}^3\text{s}$. In practice f is difficult to measure but we note that the characteristic frequency multiplying the inertial term is $\sqrt{\frac{\mu}{\rho a^2}}$, which is minimally on the order of hundreds of KHz, a full order of magnitude beyond what is currently probed experimentally in microrheological experiments[125, 106]. Macrorheological measurements occurs at lower frequencies still. In the above equation $\tau = \frac{fa^2}{\mu}$ and $\tau' = \frac{fa^2}{\lambda+2\mu} = \frac{\mu}{\lambda+2\mu}\tau$ are the time scales associated with the dissipative modes and will

dominated the behavior in the over damped system. The relationship between the shear and compressive time scales can be rewritten in terms of the zero frequency Poisson ratio of the material using the relation $\frac{\lambda}{\mu} = \frac{2\nu}{1-2\nu}$.

Computation of the translational response function via equation (3.37) is now straightforward. The integral over triple spherical harmonics in equation (3.41) can be expressed in terms of the Wigner 3j symbols, familiar from quantum mechanical angular momentum coupling. This integral is identically 0 for $l = l' = 0$ and so equation (3.37) gives

$$\zeta_{TT}^{-1} = \frac{4\pi}{\mu a}[\alpha_{00}(\omega) + \frac{1}{3}\beta_{00}(\omega)]\mathbb{I} \tag{3.47}$$

It is straightforward to calculate $\alpha_{00} = I_{\frac{1}{2}}(\omega\tau)K_{\frac{1}{2}}(\omega\tau)$, where $I_\nu(z)$ and $K_\nu(z)$ are the special bessel functions, but the function $\beta_{00}(\omega)$ is more complicated. We show the response function plotted in figure 3.1.

The computation of the rotational response function involves higher order coefficients of the inverse of $\mathbb{G}$. Working out equation (3.7) we see that these are given by

$$\sum_{l''=-\infty}^{\infty} \sum_{m''=-l''}^{l''} \mathbb{G}^{-1}_{lm;l''m''} \cdot \mathbb{G}_{l''m'';l'm'} = \delta_{ll'}\delta_{mm'}\mathbb{I} \tag{3.48}$$

Because $\mathbb{G}_{lm;l'm'}$ contains off-diagonal terms where $l \neq l'$ the inverse $\mathbb{G}^{-1}_{lm;l'm'}$ in equation (3.38) will have contributions from all orders in 1. Instead of calculating $\mathbb{G}$ to all orders of l we make the following approximation, following Muthukumar and Freed[126, 127]. Any matrix may be decomposed into its diagonal and off-diagonal parts as $G = G_D + G_{OD}$. Multiplying from the right by G^{-1} and from the left by G_D^{-1} and rearranging we get $G^{-1} = G_D^{-1} - G_D^{-1} G_{OD} G^{-1}$. We use this result to make the approximation $G^{-1}_{1m;1m'} \approx (G_{1m;1m'})^{-1}$. Equation (3.41) can then be used to compute the elements of $\mathbb{G}_{1m;1m'}$. The result is shown in table3.1. Each component of table 3.1 is a 3x3 matrix. In order to facilitate the inversion, it is convenient to take a coordinate transform from x, y, z to the spherical coordinate basis $x+iy$, $x-iy$, z. $\mathbb{G}_{1m;1m'}$ can then be put into a block diagonal form wherein the inversion is straightforward(in contrast to the Stokes problem in a viscous fluid, there are no 0 eigenvalues due to the compressiblity of the gel). Returning to cartesian coordinates, the resulting inverse is given in tables 3.2, 3.3, 3.4, 3.5, 3.6, and 3.7.

The shorthand $D(x) = \alpha_{11} + x\beta_{11}$ simply denotes linear combinations of the α and β functions. The remaining components are given by $\mathbb{G}_{1m;1m'} = \mathbb{G}^*_{1m';1m}$, the complex conjugate. Computing the rotational response function from equation (3.38) we find

Table 3.1: $\mu a\mathbb{G}_{1m;1m'}$

	m' = 1	m' = 0	m' = -1
m = 1	$D(\frac{1}{3}\mathbb{I} - \sqrt{\frac{1}{20\pi}}\beta_{11}\mathbb{I}_0$	$\sqrt{\frac{3}{20\pi}}\beta_{11}\mathbb{I}_1$	$-\sqrt{\frac{3}{10\pi}}\beta_{11}\mathbb{I}_2$
m = 0	$\sqrt{\frac{3}{20\pi}}\beta_{11}\mathbb{I}_1^*$	$D(\frac{1}{3})\mathbb{I} + \sqrt{\frac{1}{5\pi}}\beta_{11}\mathbb{I}_0$	$-\sqrt{\frac{3}{20\pi}}\beta_{11}\mathbb{I}_1$
m = -1	$-\sqrt{\frac{3}{10\pi}}\beta_{11}\mathbb{I}_2^*$	$-\sqrt{\frac{3}{20\pi}}\beta_{11}\mathbb{I}_1^*$	$D(\frac{1}{3})\mathbb{I} - \sqrt{\frac{1}{20\pi}}\beta_{11}\mathbb{I}_0$

Table 3.2: $\mu a\mathbb{G}_{11;11}(\omega)$

	x	y	z
x	$\frac{1}{2}\frac{D(\frac{3}{5})D(\frac{2}{5})-\frac{1}{25}\beta_{11}^2}{\alpha_{11}[\mathrm{D}(\frac{3}{5})\mathrm{D}(\frac{4}{5})\text{-}\frac{2}{25}\beta_{11}^2]} + \frac{1}{D(\frac{2}{5})}$	$-\frac{i}{2}\frac{D(\frac{3}{5})D(\frac{2}{5})-\frac{1}{25}\beta_{11}^2}{\alpha_{11}[\mathrm{D}(\frac{3}{5})\mathrm{D}(\frac{4}{5})\text{-}\frac{2}{25}\beta_{11}^2]} - \frac{1}{D(\frac{2}{5})}$	0
y	$-\frac{i}{2}\frac{D(\frac{3}{5})D(\frac{2}{5})-\frac{1}{25}\beta_{11}^2}{\alpha_{11}[\mathrm{D}(\frac{3}{5})\mathrm{D}(\frac{4}{5})\text{-}\frac{2}{25}\beta_{11}^2]} - \frac{1}{D(\frac{2}{5})}$	$\frac{1}{2}\frac{D(\frac{3}{5})D(\frac{2}{5})-\frac{1}{25}\beta_{11}^2}{\alpha_{11}[\mathrm{D}(\frac{3}{5})\mathrm{D}(\frac{4}{5})\text{-}\frac{2}{25}\beta_{11}^2]} + \frac{1}{D(\frac{2}{5})}$	0
z	0	0	$\frac{D(\frac{1}{5})}{D(\frac{1}{5})^2-\frac{1}{25}\beta_{11}^2}$

Table 3.3: $\mu a\mathbb{G}_{11;10}$

	x	y	z
x	0	0	$\frac{1}{\sqrt{2}}\frac{1}{5}\frac{\alpha_{11}\beta_{11}}{\alpha_{11}[\mathrm{D}(\frac{3}{5})\mathrm{D}(\frac{4}{5})\text{-}\frac{2}{25}\beta_{11}^2]}$
y	0	0	$-\frac{i}{\sqrt{2}}\frac{\frac{1}{5}\alpha_{11}\beta_{11}}{\alpha_{11}[\mathrm{D}(\frac{3}{5})\mathrm{D}(\frac{4}{5})\text{-}\frac{2}{25}\beta_{11}^2]}$
z	$\frac{1}{\sqrt{2}}\frac{1}{5}\frac{\alpha_{11}\beta_{11}}{\alpha_{11}[\mathrm{D}(\frac{3}{5})\mathrm{D}(\frac{4}{5})\text{-}\frac{2}{25}\beta_{11}^2]}$	$-\frac{i}{\sqrt{2}}\frac{1}{5}\frac{\alpha_{11}\beta_{11}}{\alpha_{11}[\mathrm{D}(\frac{3}{5})\mathrm{D}(\frac{4}{5})\text{-}\frac{2}{25}\beta_{11}^2]}$	0

Table 3.4: $\mu a\mathbb{G}_{11;1-1}$

	x	y	z
x	$\frac{\frac{1}{5}\beta_{11}D(\frac{1}{2})}{\alpha_{11}[\mathrm{D}(\frac{3}{5})\mathrm{D}(\frac{4}{5})\text{-}\frac{2}{25}\beta_{11}^2]}$	$-i\frac{\frac{1}{5}\beta_{11}D(\frac{1}{2})}{\alpha_{11}[\mathrm{D}(\frac{3}{5})\mathrm{D}(\frac{4}{5})\text{-}\frac{2}{25}\beta_{11}^2]}$	0
y	$-i\frac{\frac{1}{5}\beta_{11}D(\frac{1}{2})}{\alpha_{11}[\mathrm{D}(\frac{3}{5})\mathrm{D}(\frac{4}{5})\text{-}\frac{2}{25}\beta_{11}^2]}$	$\frac{\frac{1}{5}\beta_{11}D(\frac{1}{2})}{\alpha_{11}[\mathrm{D}(\frac{3}{5})\mathrm{D}(\frac{4}{5})\text{-}\frac{2}{25}\beta_{11}^2]}$	0
z	0	0	0

Table 3.5: $\mu a\mathbb{G}_{10;10}$

	x	y	z
x	$\frac{D(\frac{1}{5})}{D(\frac{1}{5})^2-\frac{1}{25}\beta_{11}^2}$	0	0
y	0	$\frac{D(\frac{1}{5})}{D(\frac{1}{5})^2-\frac{1}{25}\beta_{11}^2}$	0
z	0	0	$\frac{D(\frac{4}{5})}{D(\frac{3}{5})D(\frac{4}{5})-\frac{2}{25}\beta_{11}^2}$

Table 3.6: $\mu a\mathbb{G}_{10;1-1}$

	x	y	z
x	0	0	$-\frac{1}{5\sqrt{2}}\frac{\beta_{11}}{D(\frac{1}{5})^2-\frac{1}{25}\beta_{11}^2}$
y	0	0	$\frac{i}{5\sqrt{2}}\frac{\beta_{11}}{D(\frac{1}{5})^2-\frac{1}{25}\beta_{11}^2}$
z	$-\frac{1}{5\sqrt{2}}\frac{\alpha_{11}\beta_{11}}{\alpha_{11}[\mathrm{D}(\frac{3}{5})\mathrm{D}(\frac{4}{5})\text{-}\frac{2}{25}\beta_{11}^2]}$	$\frac{i}{5\sqrt{2}}\frac{\alpha_{11}\beta_{11}}{\alpha_{11}[\mathrm{D}(\frac{3}{5})\mathrm{D}(\frac{4}{5})\text{-}\frac{2}{25}\beta_{11}^2]}$	0

Table 3.7: $\mu a\mathbb{G}^{-1}_{1-1;1-1}$

	x	y	z
x	$\frac{1}{2}\frac{D(\frac{3}{5})D(\frac{2}{5})-\frac{1}{25}\beta_{11}^2}{\alpha_{11}[\mathrm{D}(\frac{3}{5})\mathrm{D}(\frac{4}{5})\text{-}\frac{2}{25}\beta_{11}^2]}+\frac{\alpha_{11}[\mathrm{D}(\frac{3}{5})\mathrm{D}(\frac{4}{5})\text{-}\frac{2}{25}\beta_{11}^2]}{2}$	$-\frac{i}{2}\frac{D(\frac{3}{5})D(\frac{2}{5})-\frac{1}{25}\beta_{11}^2}{\alpha_{11}[\mathrm{D}(\frac{3}{5})\mathrm{D}(\frac{4}{5})\text{-}\frac{2}{25}\beta_{11}^2]}-\frac{i\,\alpha_{11}[\mathrm{D}(\frac{3}{5})\mathrm{D}(\frac{4}{5})\text{-}\frac{2}{25}\beta_{11}^2]}{2}$	0
y	$-\frac{i}{2}\frac{D(\frac{3}{5})D(\frac{2}{5})-\frac{1}{25}\beta_{11}^2}{\alpha_{11}[\mathrm{D}(\frac{3}{5})\mathrm{D}(\frac{4}{5})\text{-}\frac{2}{25}\beta_{11}^2]}-\frac{i\,\alpha_{11}[\mathrm{D}(\frac{3}{5})\mathrm{D}(\frac{4}{5})\text{-}\frac{2}{25}\beta_{11}^2]}{2}$	$\frac{1}{2}\frac{D(\frac{3}{5})D(\frac{2}{5})-\frac{1}{25}\beta_{11}^2}{\alpha_{11}[\mathrm{D}(\frac{3}{5})\mathrm{D}(\frac{4}{5})\text{-}\frac{2}{25}\beta_{11}^2]}+\frac{\alpha_{11}[\mathrm{D}(\frac{3}{5})\mathrm{D}(\frac{4}{5})\text{-}\frac{2}{25}\beta_{11}^2]}{2}$	0
z	0	0	$\frac{D(\frac{1}{5})}{D(\frac{1}{5})^2-\frac{1}{25}\beta_{1}^2}$

$$\zeta_{RR}^{-1} = -\frac{3}{8\pi a^2}\alpha_{11}(\omega) \tag{3.49}$$

Finally, we wish to compute the frequency dependent moduli that the bead experiences. Equation (3.34) demands that we calculate $\mathbb{T}_{00;00}$, $\mathbb{T}_{10;00}$, $\mathbb{T}_{20;00}$, $\mathbb{T}_{10;10}$, $\mathbb{T}_{00;10}$ and $\mathbb{T}_{00;20}$. Examining equation (3.35) shows that $\mathbb{T}_{20;00} = \mathbb{T}_{00;20} = 0$ and within the diagonal approximation for $\mathbb{G}$ made above $\mathbb{T}_{00;00} = \mathbb{T}_{10;00} = \mathbb{T}_{00;10} = 0$. Thus we are left to calculate only $\mathbb{T}_{10;10}(\omega)$ in order to find $\mathbb{T}(\mathbf{k},\omega)$ to order k^2. This is straightfoward to do using the results of tables 3.2-3.7 and equation (3.35). Substituting $j_1(ka) \approx \frac{1}{3}(ka)^2$ in equation (3.34) we find

$$\mathbb{T}(\mathbf{k},\omega) = -\frac{4\pi a^3}{3V}\mu\left[\frac{1}{D(\frac{2}{5})}(\mathbb{I} - \hat{\mathbf{k}}\hat{\mathbf{k}}) + \frac{D(\frac{4}{5})}{D(\frac{3}{5})D(\frac{4}{5}) - \frac{2}{25}\beta_{11}^2}(\hat{\mathbf{k}}\hat{\mathbf{k}})\right] \tag{3.50}$$

Thus, recalling equation (3.22) we see that

$$1 - \frac{\mu(\omega)}{\mu} = \rho\frac{1}{D(\frac{2}{5})} \tag{3.51}$$

and

$$1 - \frac{\lambda(\omega)}{\lambda} = \rho\frac{\mu}{\lambda}\left\{\left[\frac{D(\frac{4}{5})}{D(\frac{3}{5})D(\frac{4}{5}) - \frac{2}{25}\beta_{11}^2}\right] - \frac{2}{D(\frac{2}{5})}\right\} \tag{3.52}$$

Results for the shear modulus are shown in figure 3.2

3.3 Self-consistent approximation

As we have stated before, the effects of higher volume fractions of inclusions can be considered by computing the cluster integrals indicated in equation (3.28) up to an arbitrary order of concentration. In practice this is laborious and we instead introduce the self consistent medium approximation in the following way. Returning to equation (3.1), we introduce an approximation to the total self energy, which we will call $\mathcal{W}$. This approximate term gives the contributions to the self energy of all the particles except for one, leading to an equation which now has the appearance of (3.19) with an extra force term, representing the presence of a single(dilute) inclusion.

$$\rho\langle\ddot{\mathbf{u}}\rangle + f\langle\dot{\mathbf{u}}\rangle - \mu\nabla^2\cdot\langle\mathbf{u}\rangle - (\lambda+\mu)\nabla\nabla\cdot\langle\mathbf{u}\rangle = \mathbf{F} + \mathcal{W}*\langle\mathbf{u}\rangle + \int d\Omega\tau(\Omega) \qquad (3.53)$$

Bringing $\mathcal{W}$ over to the left hand side of the equation and separating the transverse and parallel components as in equation (3.4) leads to an *effective* propagator

$$\mathcal{G}(\mathbf{k},\omega) = \frac{\mathbb{I}-\hat{\mathbf{k}}\hat{\mathbf{k}}}{-\rho\omega^2 - i\omega f + \mu k^2 - \mathcal{W}_\perp(\mathbf{k},\omega)} + \frac{\hat{\mathbf{k}}\hat{\mathbf{k}}}{-\rho\omega^2 - i\omega f + (\lambda+\mu)k^2 - \mathcal{W}_\parallel(\mathbf{k},\omega)} \qquad (3.54)$$

Utilizing this propagator, we may impose the boundary conditions and the equation of motion on the particle in exactly the same way as before, obtaining a scattering

operator $\mathcal{T}$ which now depends on the self energy of the effective medium $\mathcal{W}$. We again make the dilute solution approximation, only now our scattering operator depends on $\mathcal{W}$ so that we have a self consistent equation which can be solved for the self energy of the medium.

$$\langle \mathcal{W} - \mathcal{T}[\mathcal{W}] \rangle = 0 \tag{3.55}$$

As we are only interested in $\mathcal{W}$ to order k^2, we may write $\mathcal{W} \approx W_0 + W_1(ka)^2$. At length scales smaller than the diameter of the particle, a, the self energy must be a constant and so $W_1 = 0, ka > 1/2$, while at large distances, we expect the effects of screening in the effective medium to be negligible, so that $W_0 = 0$. At $ka = 1/2$ we demand $\mathcal{W}$ be continuous, leading to the boundary condition $W_1 = 4W_0 \equiv 4W$. Thus we find

$$\mathcal{G} = \begin{cases} \frac{\mathbb{I} - \hat{\mathbf{k}}\hat{\mathbf{k}}}{-i\omega f + \mu k^2 + 4W_\perp (ka)^2} + \frac{\hat{\mathbf{k}}\hat{\mathbf{k}}}{-i\omega f + \mu k^2 + 4W_\parallel (ka)^2} & , ka < \frac{1}{2} \\ \frac{\mathbb{I} - \hat{\mathbf{k}}\hat{\mathbf{k}}}{-i\omega f + \mu k^2 + W_\perp} + \frac{\hat{\mathbf{k}}\hat{\mathbf{k}}}{-i\omega f + \mu k^2 + W_\parallel} & , ka > \frac{1}{2} \end{cases} \tag{3.56}$$

Using this ansatz for the self energy leads to new functions α and β in equation (3.43)

$$\alpha_{ll'} = \alpha_{ll'}^{in} + \alpha_{ll'}^{out} \tag{3.57}$$

$$\approx (-1)^{l'} i^{l+l'} \left[\int_{1/2}^{\infty} dx\, j_l(x) j_{l'}(x) \frac{x^2}{-i\omega\tau + x^2 + \frac{g_\perp}{4}} + \int_0^{1/2} \frac{x^2}{-i\omega\tau + (1+g_\perp)x^2} \right]$$

$$\tag{3.58}$$

$$\beta_{ll'}(\omega) = \beta_{ll'}^{in} + \beta_{ll'}^{out} \tag{3.59}$$

$$\approx (-1)^{l'} i^{l+l'} \frac{\mu}{\lambda+\mu} \left[\int_{1/2}^{\infty} dx\, j_l(x) j_{l'}(x) \frac{x^2}{-i\omega\tau' + x^2 + \frac{g_\parallel}{4}} + \int_0^{1/2} \frac{x^2}{-i\omega\tau' + (1+g_\parallel)x^2} \right] - \alpha_{ll'}$$

$$\tag{3.60}$$

Here τ and τ' carry the same significance as before. We have defined $g_\perp \equiv \frac{4Wa^2}{\mu}$ and $g_\parallel \equiv \frac{4Wa^2}{\mu+\lambda}$. The form of the self energy in equation (3.16) is exactly the same, yielding four equations for the real and imaginary part of the parallel and perpendicular components with these new functions α and β.

$$g_\perp - \rho \frac{1}{2} \frac{1}{\alpha_{11} + \frac{2}{5}\beta_{11}} = 0 \tag{3.61}$$

$$g_\parallel - \rho \frac{\mu}{\lambda+\mu} \frac{\alpha_{11} + \frac{4}{5}\beta_{11}}{(\alpha_{11} + \frac{3}{5}\beta_{11})(\alpha_{11} + \beta_{11})} = 0 \tag{3.62}$$

This set of equations can be solved for the real and imaginary components of $g_\perp$ and $g_\parallel$ using a nonlinear numerical solver of choice. We have used MINPACK's hybrd and hybrj algorithm implemented through the `fsolve` routine available in the Scipy

package of Python. Having obtained the value of $g_\perp$ and $g_\parallel$ we may plug them back into equations (3.37) and (3.38) via the α and β functions contained therein in order to obtain the modified response of the particles. Modification to the real and imaginary parts of the response function are plotted in figures 3.4 and 3.5.

The shear modulus of the gel as a function of particle loading density is shown in figure 3.6. Within the effective medium approximation, the dependence appears to be essentially linear. This arises from the nature of the approximation made in equation (3.53), but does not seem to describe experimental results well[128, 111]. The nature of the approximation made in equation (3.53) can be better understood by returning to equation (3.28). Taking the correlations between particles to be 0, the series for Σ is a geometric series in $\langle \mathbb{T} \rangle$ which can be explicitly summed. This is the random phase approximation. Summing the series we find

$$\Sigma = \frac{\mathbb{I}}{\mathbb{I} - \mathbb{G}\langle \mathbb{T} \rangle} \tag{3.63}$$

Taking the effective composite to be dilute in particle concentration, as in equation (3.55), and assuming the particles are uncorrelated, the self energy for N particles reduces to a multiple of the self energy for a single particle in the effective medium so

that $\Sigma_N(\mathbf{k},\omega) = \frac{N-1}{V}\Sigma_1(\mathbf{k},\omega)$, where Σ_1 is the self energy due to one particle and Σ_N is the self energy of the entire composite from N particles. Here, Σ_1 is a functional of the effective medium propagator, as shown in equation (3.63). This self consistent relation leads to equation (3.61). When equation (3.61) is solved we find that the contribution of this leading multiplier in the concentration of particles dominates over corrections due to higher order terms contained in the self-consistent Σ_N and we obtain a nearly linear dependence over the range of inclusion volume fractions.

Significant work has been done to incorporate the effects of inclusion correlations on bulk properties of elastic composites[129, 130, 131, 132] as well as in composites with viscoelastic matrices or inclusions[133, 7, 134, 120]. Nanocomposites have additionally shown a rich dependence on the conditions of particle loading to the exact microstructure and resulting effective macroscopic properties[111, 112, 128, 113, 114, 135, 136]. Understanding the relationship between this microstructure (captured by correlations among the inclusions) and the macrorheological and elastic properties of these composites remains a significant challenge. In light of the above calculations, however, we see that incorporation of these effects into the multiple scattering picture is crucial to capture experimentally observed behavior.

3.4 Conclusion

We have calculated the response of a spherical inclusion in a permanently crosslinked gel at arbitrary loading fractions of particles. Further we have found that the dependence of the measured modulus of the gel on loading fraction follows an approximately linear law up to the percolation limit of the inclusions. In calculating up to arbitrary volume fractions we have ignored correlations between particles. We have instead replaced the complicated problem of accounting for the scattering off all particles to all orders of scattering with the much simpler problem of a dilute composite in an effective medium. The effective medium properties are chosen in such a way as to account for the scattering of all higher orders in a mean field way.

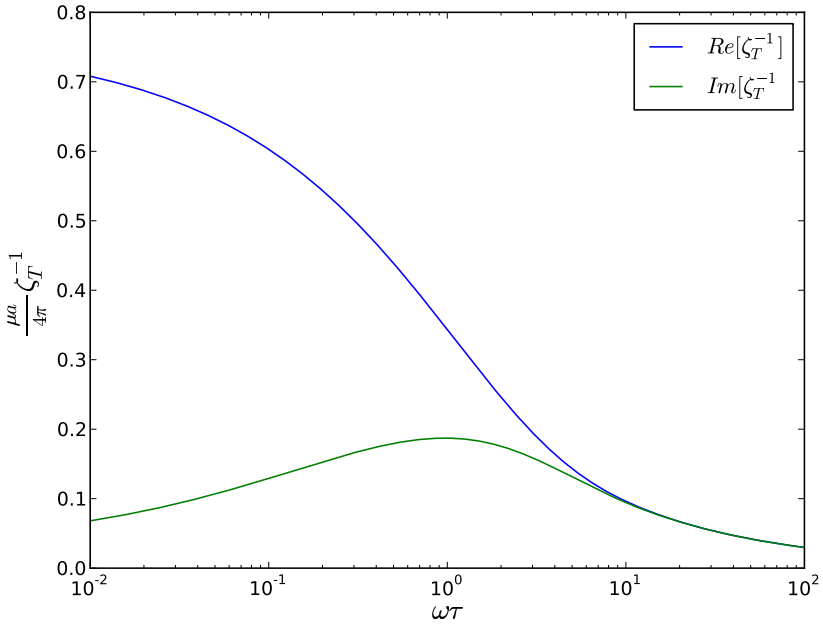

Figure 3.1: Response function of the bead.

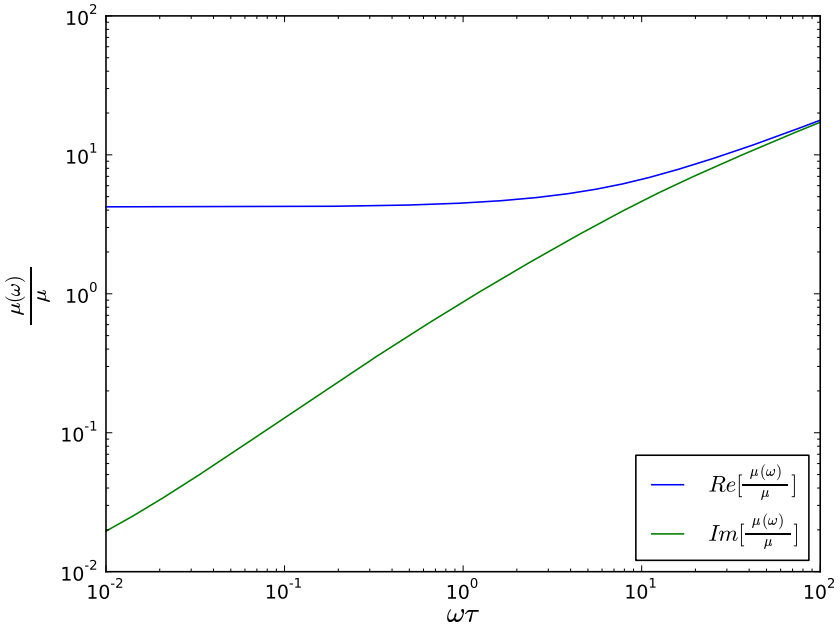

Figure 3.2: Freqency dependent shear modulus.

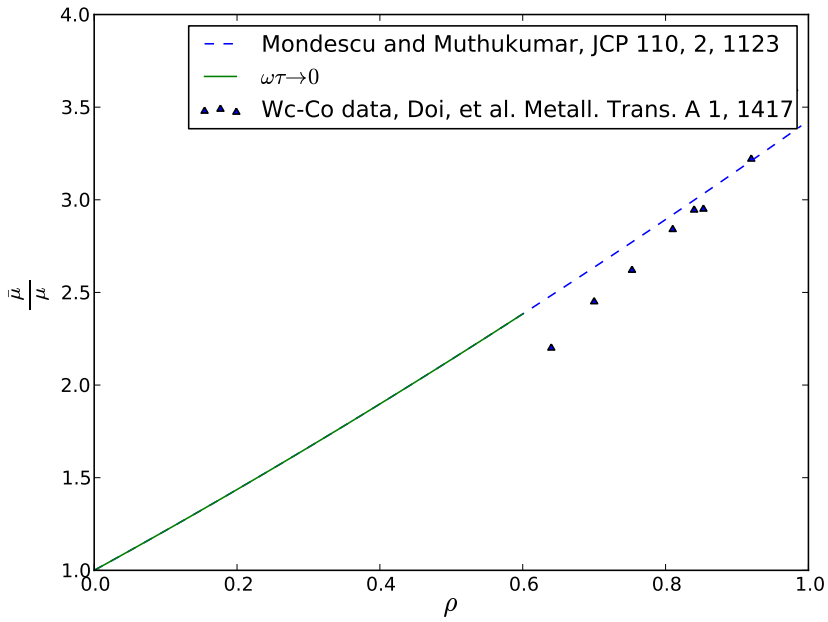

Figure 3.3: Zero-frequency limit agrees with experimental data for elastomer composites.

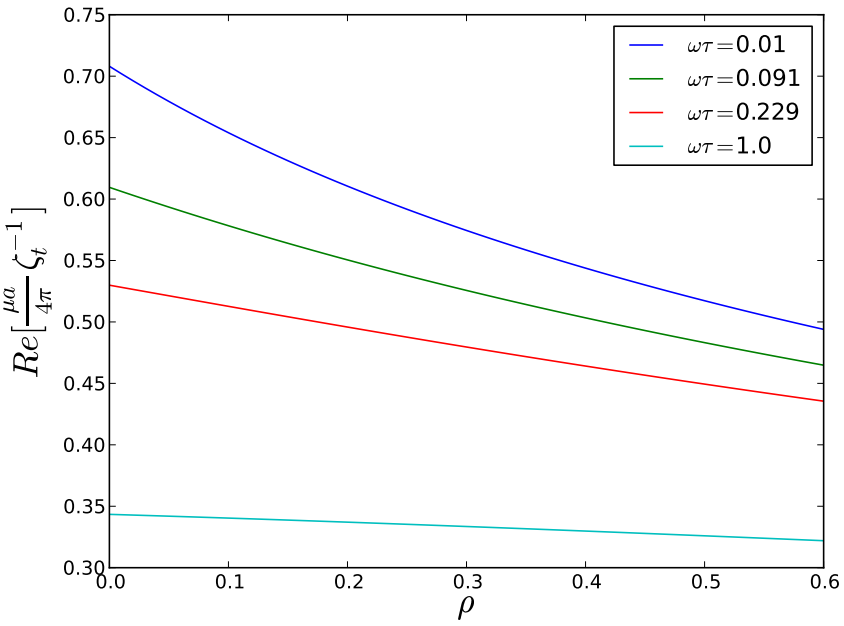

Figure 3.4: Modification of the storage response function of the bead at different frequencies.

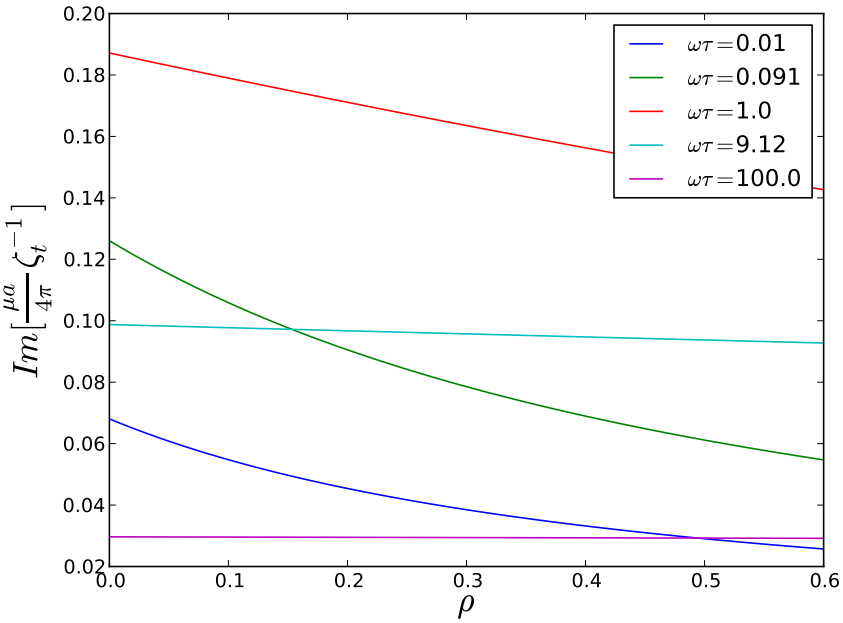

Figure 3.5: Modification of the loss response function of the bead.

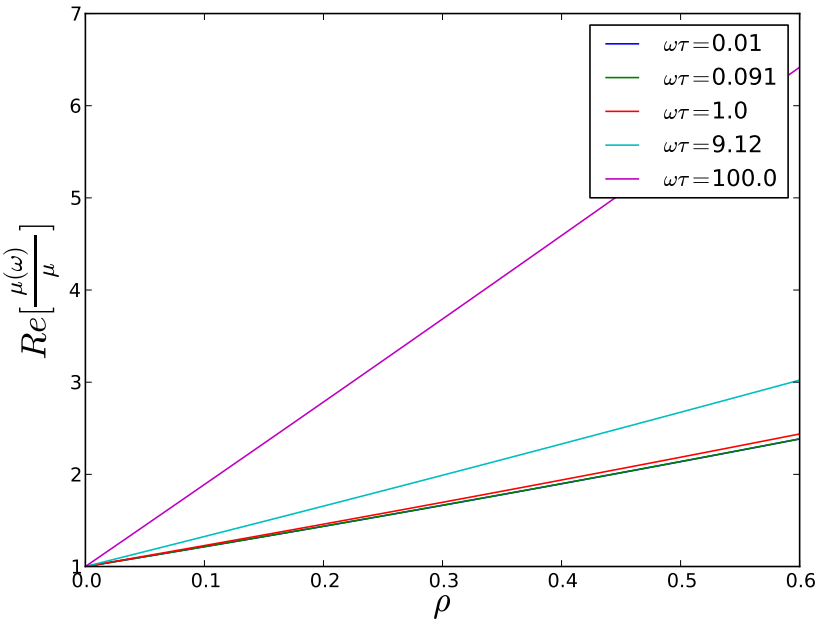

Figure 3.6: Modification of the storage modulus at different frequencies.

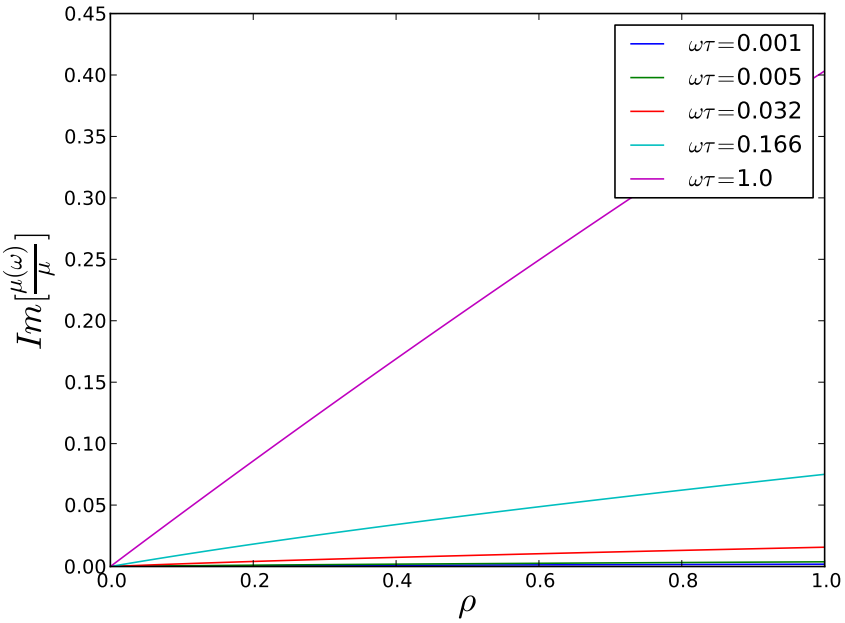

Figure 3.7: Modification of the loss modulus at different frequencies.

APPENDIX A

EXPRESSIONS FOR MEAN FIRST PASSAGE TIME AND SUCCESS RATES OF TRANSLOCATION

A.1 Reflecting/Absorbing Boundary Condition

For reflecting/absorbing boundary conditions, we consider a chain of length N broken into i_{max} blocks, the i^{th} block being of length l_i and having monomers which experience a chemical potential difference μ_i across the pore and friction coefficient k_i. Using Eqs. (1.6) and (1.7) we obtain for $m_0 < l_1$

$$\tau(m_0) = \frac{1}{\mu_1 k_1}\left[(f-m_0) - \frac{1}{\mu_1}\left(e^{-\mu_1 m_0} - e^{\mu_1 l_1}\right)\right] + \sum_{i=2}^{i_{max}} \frac{1}{\mu_i k_i}\left[l_i - \frac{1}{\mu_i}\left(1-e^{-\mu_i l_i}\right)\right] + \sum_{i=1}^{i_{max}-1}\sum_{j=i+1}^{i_{max}} \frac{1}{\mu_i \mu_j k_i}\left[\left(1-e^{-\mu_i l_i}\right) e^{-\sum_{k=i+1}^{j-1}\mu_k l_k}\left(1-e^{-\mu_j l_j}\right)\right]. \quad \text{(A.1)}$$

For a diblock copolymer with $m_0 \to 0$, $\mu_1 \to \mu$, and $\mu_2 \to 0$, this reduces to Eq. (1.8).

A.2 Absorbing/Absorbing Boundary Condition

In order to compute τ_+ and τ from Eqs. (1.14) and (1.12) for a diblock copolymer with the first block of length f and the second block of length $N-f$ experiencing driving potentials across the pore of μ_1 and μ_2 and friction coefficients k_1 and k_2 we require the functions $\Psi(x,y)$ and $\phi_+(x,y)$ in three regimes: $x<y<f$, $x<f<y$ and $f<x<y$. For a diblock copolymer $\Psi(x,y)$ is given by evaluating Eq. (1.10) as

$$\Psi(x,y)=\begin{cases} \frac{1}{\mu_1}\left(e^{-\mu_1 x}-e^{-\mu_1 y}\right) & x<y<f \\ \frac{1}{\mu_1}\left(e^{-\mu_1 x}-e^{-\mu_1 f}\right)+\frac{1}{\mu_2}e^{-\mu_1 f}\left(1-e^{-\mu_2(y-f)}\right) & x<f<y \\ \frac{1}{\mu_2}e^{(\mu_2-\mu_1)f}\left(e^{-\mu_2 x}-e^{-\mu_2 y}\right) & f<x<y, \end{cases} \tag{A.2}$$

The limit $\mu_2 \to 0$ discussed in the text is straightforward.

Likewise, computing the integrals in Eq. (1.13) for a diblock copolymer gives for $x<y<f$

$$\phi_+(x,y)=\frac{1}{\mu_1^2 k_1}\left[(y-x)+\frac{2}{\mu_1}\left(e^{-\mu_1 y}-e^{-\mu_1 x}\right)+\left(ye^{-\mu_1 y}-xe^{-\mu_1 x}\right)\right]. \tag{A.3}$$

For $x<f<y$, we obtain

$$\phi_+(x,y) = \frac{1}{\mu_1^2 k_1}\left[(f-x) - \frac{2}{\mu_1}\left(e^{-\mu_1 x} - e^{-\mu_1 f}\right) - \left(xe^{-\mu_1 x} - fe^{-\mu_1 f}\right)\right]$$
$$+ \frac{1}{\mu_1\mu_2 k_1} e^{-\mu_1 f}\left(1 - e^{-\mu_2(y-f)}\right)\left[\frac{1}{\mu_1}\left(e^{\mu_1 f} - 1\right) - f\right]$$
$$+ \frac{1}{\mu_1\mu_2 k_2}\left(1 - e^{-\mu_1 f}\right)\left[(y-f) - \frac{1}{\mu_2}\left(1 - e^{-\mu_2(y-f)}\right)\right]$$
$$+ \frac{1}{\mu_2^2 k_2} e^{-\mu_1 f}\left[(y-f) - \frac{2}{\mu_2}\left(1 - e^{-\mu_2(y-f)}\right) + (y-f)e^{-\mu_2(y-f)}\right]. \tag{A.4}$$

Finally, for $f < x < y$ we have

$$\phi_+(x,y) = \frac{1}{\mu_1\mu_2 k_1} e^{-\mu_1 f} e^{\mu_2 f}\left(e^{-\mu_2 x} - e^{-\mu_2 y}\right)\left[\frac{1}{\mu_1}\left(e^{\mu_1 f} - 1\right) - f\right]$$
$$+ \frac{1}{\mu_1\mu_2 k_2}\left[(y-x) - \frac{1}{\mu_2} e^{\mu_2 f}\left(e^{-\mu_2 x} - e^{\mu_2 y}\right)\right]\left(1 - e^{-\mu_1 f}\right) + \frac{y-x}{\mu_2^2 k_2} e^{-\mu_1 f} e^{\mu_2 f}$$
$$+ \frac{1}{\mu_2^2 k_2} e^{-\mu_1 f} e^{\mu_2 f}\left[f\left(e^{-\mu_2 x} - e^{-\mu_2 y}\right) - \frac{2}{\mu_2}\left(e^{-\mu_2 x} - e^{-\mu_2 y}\right) - \left(xe^{-\mu_2 x} - ye^{-\mu_2 y}\right)\right]. \tag{A.5}$$

In the limit $\mu_2 \to 0$, $\phi_+(x,y)$ becomes

$$\phi_+(x,y) \to \begin{cases} \frac{1}{\mu_1^2 k_1}\left[(y-x)+\frac{2}{\mu_1}\left(e^{-\mu_1 y}-e^{-\mu_1 x}\right)+\left(ye^{-\mu_1 y}-xe^{-\mu_1 x}\right)\right] & x<y<f \\ \frac{1}{\mu_1^2 k_1}\left[(f-x)-\frac{2}{\mu_1}\left(e^{-\mu_1 x}-e^{-\mu_1 f}\right)-\left(xe^{-\mu_1 x}-fe^{-\mu_1 f}\right)\right] & \\ \quad -\frac{y-f}{\mu_1 k_1}\left[fe^{-\mu_1 f}-\frac{1}{\mu_1}\left(1-e^{-\mu_1 f}\right)\right] & x<f<y \\ \quad +\frac{(y-f)^2}{2\mu_1 k_2}\left(1-e^{-\mu_1 f}\right)+\frac{(y-f)^3}{6k_2}e^{-\mu_1 f} & \\ \frac{(y-x)}{\mu_1 k_1}e^{-\mu_1 f}\left[\frac{1}{\mu_1}\left(e^{\mu_1 f}-1\right)-f\right] & \\ \quad +\frac{(y^2-x^2)}{2\mu_1 k_2}\left(1-e^{-\mu_1 f}\right)-\frac{y-x}{\mu_1 k_1}f\left(1-e^{-\mu_1 f}\right) & f<x<y. \\ \quad +\frac{(y^3-x^3)}{6k_2}e^{-\mu_1 f}-\frac{y^2-x^2}{2k_2}fe^{-\mu_1 f}+\frac{y-x}{2k_2}f^2e^{-\mu_1 f} & \end{cases} \tag{A.6}$$

In order to compute the mean dwell times five separate integrals are required in Eq. (1.14). We use the definitions of $H(y)$ and $\psi(y)$ given in Eqs. (1.15) and (1.7), respectively. For $m_0 < f$, the required integrals are

$$I_1 \equiv \int_{m_0}^{N} dy\, \frac{1}{\psi(y)} = \frac{1}{\mu_1}\left(e^{-\mu_1 m_0} - e^{-\mu_1 f}\right) + \frac{1}{\mu_2} e^{-\mu_1 f}\left(1 - e^{-\mu_2 (N-f)}\right) \tag{A.7a}$$

$$I_2 \equiv \int_{0}^{m_0} dy\, \frac{H(y)}{\psi(y)} = \frac{1}{\mu_1 k_1}\left[\frac{1}{\mu_1}\left(1 - e^{-\mu_1 m_0}\right) - m_0\right] \tag{A.7b}$$

$$I_3 \equiv \int_{0}^{m_0} dy\, \frac{1}{\psi(y)} = \frac{1}{\mu_1}\left(1 - e^{-\mu_1 m_0}\right) \tag{A.7c}$$

$$\begin{aligned} I_4 \equiv \int_{m_0}^{N} dy\, \frac{H(y)}{\psi(y)} &= 1\mu_1 k_1 \left[\frac{1}{\mu_1}\left(e^{-\mu_1 m_0} - e^{-\mu_1 f}\right) - (f - m_0)\right] \\ &\quad + \frac{1}{\mu_1 \mu_2 k_1} e^{\mu_2 f}\left(1 - e^{-\mu_1 f}\right)\left(e^{-\mu_2 N} - e^{-\mu_2 f}\right) \\ &\quad + \frac{1}{\mu_2 k_2}\left[\frac{1}{\mu_2}\left(1 - e^{-\mu_2 (N-f)}\right) - (N - f)\right] \end{aligned} \tag{A.7d}$$

$$I_5 \equiv \int_{0}^{N} dy\, \frac{1}{\psi(y)} = \frac{1}{\mu_1}\left(1 - e^{-\mu_1 f}\right) + \frac{1}{\mu_2} e^{-\mu_1 f}\left(1 - e^{-\mu_2 (N-f)}\right). \tag{A.7e}$$

For $m_0 > f$, they are

$$I_1 \equiv \int_{m_0}^{N} dy\, \frac{1}{\psi(y)} = \frac{1}{\mu_2} e^{-\mu_1 f} \left(e^{-\mu_2 (m_0 - f)} - e^{-\mu_2 (N-f)} \right) \tag{A.8a}$$

$$\begin{aligned} I_2 \equiv \int_{0}^{m_0} dy\, \frac{H(y)}{\psi(y)} = & \frac{1}{\mu_1 k_1} \left[\frac{1}{\mu_1} \left(1 - e^{-\mu_1 f} \right) - f \right] \\ & - \frac{1}{\mu_1 \mu_2 k_1} \left(1 - e^{-\mu_1 f} \right) \left(1 - e^{-\mu_2 (m_0 - f)} \right) \\ & - \frac{1}{\mu_2 k_2} \left[(m_0 - f) - \frac{1}{\mu_2} \left(1 - e^{-\mu_2 (m_0 - f)} \right) \right] \end{aligned} \tag{A.8b}$$

$$I_3 \equiv \int_{0}^{m_0} dy\, \frac{1}{\psi(y)} = \frac{1}{\mu_1} \left(1 - e^{-\mu_1 f} \right) + \frac{1}{\mu_2} e^{-\mu_1 f} \left(1 - e^{\mu_2 (m_0 - f)} \right) \tag{A.8c}$$

$$\begin{aligned} I_4 \equiv \int_{m_0}^{N} dy\, \frac{H(y)}{\psi(y)} = & \frac{1}{\mu_1 \mu_2 k_1} \left(1 - e^{-\mu_1 f} \right) \left(e^{-\mu_2 (N-f)} - e^{-\mu_2 (m_0 - f)} \right) \\ & - \frac{1}{\mu_2 k_2} \left[(N - m_0) - \frac{1}{\mu_2} \left(e^{-\mu_2 (m_0 - f)} - e^{-\mu_2 (N-f)} \right) \right] \end{aligned} \tag{A.8d}$$

$$I_5 \equiv \int_{0}^{N} dy\, \frac{1}{\psi(y)} = \frac{1}{\mu_1} \left(1 - e^{-\mu_1 f} \right) + \frac{1}{\mu_2} e^{-\mu_1 f} \left(1 - e^{-\mu_2 (N-f)} \right). \tag{A.8e}$$

From Eq. (1.14) the mean first passage time for absorbing/absorbing boundary conditions is given by

$$\tau = \frac{I_1 I_2 - I_3 I_4}{I_5}, \tag{A.9}$$

APPENDIX B

DISTRIBUTION OF MEAN TRANSLOCATION TIMES

The full probability distribution for the position of the diblock chain in the pore at any time t given that at time $t = 0$ the chain is at the m_0^{th} monomer is obtained by solving the Fokker-Planck equation, Eq. (1.3), subject to the boundary conditions of interest. The solution can be written as a sum of eigenfunctions

$$P(m, t; m_0, t_0) = \sum_{\lambda} A_\lambda(m_0) P_\lambda(m) exp[-\lambda(t - t_0)], \tag{B.1}$$

with $P_\lambda(x)$ satisfying the equation

$$\partial_m[Q(m)P_\lambda(m)] + \partial_m^2 [k_m P_\lambda(m)] = -\lambda P_\lambda(m), \tag{B.2}$$

where for a diblock with a charged block of length f, $Q(m)$ is given by

$$Q(m) = \begin{cases} -k\mu & m < f \\ 0 & m > f. \end{cases} \tag{B.3}$$

B.1 Absorbing/Absorbing Boundary Conditions

For absorbing boundary conditions at both ends of the chain $P_\lambda(m)$ is given by

$$P_\lambda(m) = \begin{cases} e^{\frac{\mu}{2}m}\sin[\beta_\lambda m] & m < f \\ \\ e^{\frac{\mu}{2}f}\frac{\sin[\beta_\lambda f]}{\sin[\gamma_\lambda(f-N)]}\sin\left[\gamma_\lambda(m-N)\right] & m > f, \end{cases} \tag{B.4}$$

where $\gamma_\lambda^2 \equiv \lambda/k$ and $\beta_\lambda^2 \equiv \gamma_\lambda^2 - \left(\frac{\mu}{2}\right)^2$ for convenience. The allowed modes are determined by the condition at f on the discontinuity in the derivative

$$\Delta\partial_m P_\lambda|_f = -\mu P_\lambda|_f\,. \tag{B.5}$$

This gives

$$\left[\gamma_\lambda + \frac{\mu}{2}\tan\left[\gamma_\lambda(f-N)\right]\right]\tan\left(\beta_\lambda f\right) = \beta_\lambda \tan\left[\gamma_\lambda(f-N)\right]. \tag{B.6}$$

It can be shown generally[52] that enforcing the initial condition $P(m,t;m_0,t_0) = \delta(m-m_0)$ gives $A_\lambda(m_0) = [p_s(m_0)]^{-1}P_\lambda(m_0)$, where p_s is the steady state solution to the equation with reflecting boundary conditions. It is given by

$$p_s(m_0) = \begin{cases} e^{\mu m_0} & m_0 < f \\ \\ e^{\mu f} & m_0 > f. \end{cases} \tag{B.7}$$

This gives

$$A_\lambda(m_0) = \begin{cases} e^{-\frac{\mu}{2}m_0}\sin[\gamma_\lambda m_0] & m_0 < f \\ \\ e^{-\frac{\mu}{2}f}\frac{\sin\left[\sqrt{\gamma^2-(\frac{\mu}{2})^2}f\right]}{\sin[\gamma_\lambda(f-N)]}\sin\left[\gamma_\lambda(m_0-N)\right] & m_0 > f. \end{cases} \tag{B.8}$$

Combining Eqs. (B.8) and (B.4) into Eq. (B.1) and summing over solutions to Eq. (B.6) gives the solution to Eq. (1.3).

The distribution of exit times from either end of the pore is given by the flux at that boundary, where $J(m,t;m_0,t_0) = Q(m)P(m,t;m_0,t_0) + \partial_m[k_m P(m,t;m_0,t_0)]$. Evaluating this at the boundary $m = N$ gives the expected distribution of successful passage times as

$$g_+(m_0,t) = \sum_\lambda k\gamma_\lambda A_\lambda(m_0)e^{\frac{\mu}{2}f}\frac{\sin\left[\beta_\lambda f\right]}{\sin\left[\gamma_\lambda(f-N)\right]}e^{-\lambda(t-t_0)}, \tag{B.9}$$

with $A_\lambda(m_0)$ given by Eq. (B.8). This distribution is plotted in Fig. 2.8. A similar calculation accounting for exit at both ends of the chain gives the distribution of dwell times plotted in Fig. 1.9:

$$g(m_0,t) = \sum_\lambda A_\lambda(m_0)\lambda\left\{\frac{4\beta_\lambda}{\gamma_\lambda^2}\left[1-e^{\frac{\mu}{2}f}\cos(\beta_\lambda f)\right] + e^{\frac{\mu}{2}f}\frac{\sin[\beta_\lambda f]}{\tan[\gamma_\lambda(f-N)]}\right\}e^{-\lambda t}. \tag{B.10}$$

As alluded to in the text discussion of absorbing/absorbing boundary conditions, for small values of f increasing the length of the charged block leads to an increase in the number of diffusion dominated long time events in the far right tails of the distributions, counterintuitively moving the experimentally measured first moment of the distribution towards longer times. As the length of the charged block is increased further(and the length of the uncharged block decreased), the overall translocation process become progressively more drift dominated and the tails of the distribution shrink once again, with a coincident decrease in the translocation time.

B.2 Reflecting/Absorbing Boundaries

Following the same procedure as above, we impose a reflecting boundary condition at $m = 0$ in equation by requiring the flux evaluated there to be zero: $J|_{m=0} = -k\mu P_\lambda + k\partial_m P_\lambda = 0$. We obtain

$$P_\lambda(m) = \begin{cases} \sin[\alpha_\lambda m] + \frac{\alpha_\lambda}{\mu - \gamma_\lambda^2}\cos[\alpha_\lambda m] & m < f \\ (\sin[\gamma_\lambda m] - \tan[\gamma_\lambda N]\cos[\gamma_\lambda m])\,\frac{\sin[\alpha_\lambda f] + \frac{\alpha_\lambda}{\mu-\gamma_\lambda^2}\cos[\alpha_\lambda f]}{\sin[\gamma_\lambda f] - \tan[\gamma_\lambda N]\cos[\gamma_\lambda f]} & m > f, \end{cases} \tag{B.11}$$

where we have defined $\gamma_\lambda^2 \equiv \frac{\lambda}{k}$ for convenience as above. Using the same relation for A_λ as for absorbing/absorbing boundaries we obtain

$$A_\lambda(m_0) = \begin{cases} e^{-\mu m_0}\left(\sin[\alpha_\lambda m_0] + \frac{\alpha_\lambda}{\mu-\gamma_\lambda^2}\cos[\alpha_\lambda m_0]\right) & m_0 < f \\ e^{-\mu f}\left(\sin[\gamma_\lambda m_0] - \tan[\gamma_\lambda N]\cos[\gamma_\lambda m_0]\right)\frac{\sin[\alpha_\lambda f]+\frac{\alpha_\lambda}{\mu-\gamma_\lambda^2}\cos[\alpha_\lambda f]}{\sin[\gamma_\lambda f]-\tan[\gamma_\lambda N]\cos[\gamma_\lambda f]} & m_0 > f. \end{cases} \tag{B.12}$$

α_λ is given by solutions to the equation

$$\begin{aligned} \gamma_\lambda\left[(1+\tan[\gamma_\lambda N]\tan[\gamma_\lambda f]) + \mu\left(\tan[\gamma_\lambda f] - \tan[\gamma_\lambda N]\right)\right]\left[\tan[\alpha_\lambda f] + \frac{\alpha_\lambda}{\mu-\gamma_\lambda^2}\right] \\ = \alpha_\lambda\left(1 - \frac{\alpha_\lambda}{\mu-\gamma_\lambda^2}\tan[\alpha_\lambda f]\right)\left(\tan[\gamma_\lambda f] - \tan[\gamma_\lambda N]\right). \end{aligned} \tag{B.13}$$

Solving Eq. (B.13) gives α_λ for each $\lambda = 0, 1, 2...$ and combining Eqs. (B.12) and (B.11) in Eq. (B.1) then summing over $\lambda = 0, 1, 2...$ gives the full probability distribution. The unnormalized distribution of exit times is given by the flux at the absorbing boundary, $m = N$:

$$\begin{aligned} g(m_0, t) = \sum_\lambda k\gamma_\lambda A_\lambda(m_0)\left(\cos[\gamma_\lambda N] + \tan[\gamma_\lambda N]\sin[\gamma_\lambda N]\right) \\ \times\frac{\sin[\alpha_\lambda f] + \frac{\alpha_\lambda}{\mu-\gamma_\lambda^2}\cos[\alpha_\lambda f]}{\sin[\gamma_\lambda f] - \tan[\gamma_\lambda N]\cos[\gamma_\lambda f]}e^{-\lambda t}. \end{aligned} \tag{B.14}$$

This equation is plotted in Fig. 1.9.

BIBLIOGRAPHY

[1] Mirigian, Stephen, Wang, Yanbo, and Muthukumar, Murugappan. Translocation of a heterogeneous polymer. *submitted to Journal of Chemical Physics*.

[2] Kasianowicz, John J., Brandin, Eric, Branton, Daniel, and Deamer, David W. Characterization of individual polynucleotide molecules using a membrane channel. *Proceedings of the National Academy of Science 93* (1996), 13770–13773.

[3] Bezrukov, Sergey M., Vodyanoy, Igor, Brutyan, Rafik A., and Kasianowicz, John J. Dynamics and free energy of polymers partioning into a nanoscale pore. *Macromolecules 26* (1996), 8517–8522.

[4] Meller, Amit, Nivon, Lucas, Brandin, Eric, Golovchenko, Jene, and Branton, Daniel. Rapid nanopore discrimination between single polynucleotide molecules. *Proceedings of the National Academy of Sciences 97* (2000), 1079–1084.

[5] Akeson, Mark, Branton, Daniel, Kasianowicz, John J., Brandin, Eric, and Deamer, David W. Microsecond time-scale discrimination among polycytidylic acid, polyadenylic acid, and polyuridylic acid as homopolymers or as segments within single rna molecules. *Biophysical Journal 77* (1999), 3227–3233.

[6] Meller, Amit. Dynamics of polynucleotide transport through nanometre-scale pores. *Journal of Physics: Condensed Matter 15* (2003), R581–R607.

[7] Wang, Hui, Dunning, James E., Huang, Albert P.H., Nyamwanda, Jacqueline A., and Branton, Daniel. DNA heterogeneity and phosphorylation unveiled by single-molecule electrophoresis. *Proceedings of the National Academy of Science 101*, 37 (2004), 13472–13477.

[8] Butler, Tom Z., Gundlach, Jens H., and Troll, Mark A. Determination of RNA orientation during translocation through a biological nanopore. *Biophysical Journal 90* (2006), 190–199.

[9] Wong, Chiu Tai Andrew, and Muthukumar, M. Polymer translocation through a cylindrical channel. *Journal of Chemical Physics 128* (2008), 154903.

[10] Wong, Chiu Tai Andrew, and Muthukumar, Murugappan. Polymer translocation through α-hemolysin pore with tunable polymer electrostatic interaction. *Journal of Chemical Physics 133* (2010), 045101.

[11] Li, Jiali, Gershow, Marc, Stein, Derek, Brandin, Eric, and Golovchenko, J. A. Dna molecules and configurations in a solid state nanopore microscope. *Nature: Materials 2* (2003), 611–615.

[12] Chen, Peng, Gu, Jiajun, Brandin, Eric, Kim, Young-Rok, Wang, Qiao, and Branton, Daniel. Probing single DNA molecule transport using fabricated nanopores. *Nanoletters 4*, 11 (2004), 2293–2298.

[13] Fologea, Daniel, Uplinger, James, Thomas, Brian, McNabb, David S., and Li, Jiali. Slowing DNA translocation in a solid-state nanopore. *Nanoletters 5*, 9 (2005), 1734–1737.

[14] Fologea, Daniel, Gershow, Marc, Ledden, Bradley, McNabb, David S., Golovchenko, Jene A., and Li, Jiali. Detecting single stranded DNA with a solid state nanopore. *Nanoletters 5*, 10 (2005), 1905–1909.

[15] Storm, Arnold J., Storm, Cornelis, Chen, Jianghua, Zandbergen, Henny, Joanny, Jean-Francois, and Dekker, Cees. Fast DNA translocation through a solid-state nanopore. *Nanoletters 5*, 7 (2005), 1193–1197.

[16] Storm, Arnold J., Chen, J.H., Zandbergen, H.W., and Dekker, C. Translocation of double-strand DNA through a silicon oxide nanopore. *Physical Review E 71* (2005), 051903.

[17] Purnell, Robert F., Mehta, Kunal K., and Schmidt, Jacob J. Nucleotide identification and orientation discrimination of DNA homopolymers immobilized in a protein nanopore. *Nanoletters 8*, 9 (2008), 3029–3034.

[18] Oukhaled, Abdelghani, Cressiot, Benjamin, Bacri, Laurent, Pastoriza-Gallego, Manuela, Betton, Jean-Michel, Bourhis, Eric, Jede, Ralk, Gierak, Jacques, Auvray, Lo$\acute{}$ic, and Pelta, Juan. Dynamics of completely unfolded and native proteins through solid-state nanopores as a function of electric driving force. *ACS: Nano 5*, 5 (2011), 3628–3638.

[19] Wolfe, A.J., Mohammad, M.M., Cheley, S., Bayley, H., and Movileanu, L. Catalyzing the translocation of polypeptides through attractive interactions. *J. Am. Chem. Soc. 129*, 45 (2007), 14034–14341.

[20] Cockroft, Scott L., Chu, John, Amorin, Manuel, and Ghadiri, M. Reza. A single-molecule nanopore device detects DNA polymerase activity with single-nucleotide resolution. *J. Am. Chem. Soc. 130*, 3 (2008), 818–820.

[21] Mathe, Jerome, Aksimentiev, Aleksei, Nelson, David R., Schulten, Klaus, and Meller, Amit. Orientation discrimination of single-stranded DNA inside the α-hemolysin membrane channel. *Proceedings of the National Academy of Science 102*, 35 (2005), 12377–12382.

[22] Smeets, Ralph M. M., Keyser, Ulrich F., Krapf, Diego, Wu, Meng-Yue, Dekker, Nynke H., and Dekker, Cees. Salt dependence of ion transport and DNA translocation through solid-state nanopores. *Nanoletters 6*, 1 (2006), 89–95.

[23] Kowalczyk, Stefan W., Wells, David B., Aksimentiev, Aleksi, and Deeker, Cees. Slowing down DNA translocation through a nanopore in lithium chloride. *Nanoletters 12* (2012), 1038–1044.

[24] Misakian, M., and Kasianowicz, J.J. Electrostatic influence on ion transport through the αHL channel. *J.Membrane Biol. 195* (2003), 137–146.

[25] Muthukumar, Murugappan. *Polymer Translocation*. CRC Press, 2011.

[26] Sung, W., and Park, P.J. Polymer translocation through a pore in a membrane. *Physical Review Letters 77*, 4 (1996), 783–786.

[27] DiMarzio, E.A., and Mandell, A.J. Phase transition behavior of a linear macromolecule threading a membrane. *Journal of Chemical Physics 107* (1997), 5510.

[28] Muthukumar, Murugappan. Polymer translocation through a hole. *Journal of Chemical Physics 111*, 22 (1999), 10371–10374.

[29] Lubensky, David K., and Nelson, David R. Driven polymer translocation through a narrow pore. *Biophysical Journal 77* (1999), 1824 – 1838.

[30] Panja, D., Barkema, G.T., and Ball, R.C. Anomalous dynamics of unbiased polymer translocation through a nanopore. *Journal of Physics: Condensed Matter 19* (2007), 432202.

[31] Sakaue, T. Nonequilibrium dynamics of polymer translocation and straightening. *Physical Review E 76* (2007), 021803.

[32] Muthukumar, M. Polymer escape through a nanopore. *Journal of Chemical Physics 118*, 11 (2003), 5174–5183.

[33] Ambjörnsson, T., Apell, S.P., Konkoli, Z., Di Marzio, E.A., and Kasianowicz, J.J. Charged polymer membrane translocation. *Journal of Chemical Physics 117*, 8 (2002), 4063.

[34] Slutsky, Michael, Kardar, Mehran, and Mirny, Leonid A. Diffusion in correlated random potentials, with applications to DNA. *Physical Review E 69* (2004), 061903.

[35] Milchev, Andrey, Binder, Kurt, and Bhattacharya, Aniket. Polymer translocation through a nanopore induced by adsorption: Monte carlo simulation of a coarse-grained model. *Journal of Chemical Physics 121*, 12 (2004), 6042.

[36] Muthukumar, Murugappan. Theory of sequence effects on DNA translocation through proteins and nanopores. *Electrophoresis 23* (2002), 1417–1420.

[37] Mohan, Aruna, Kolomeisky, Anatoly B., and Pasquali, Matteo. Effect of charge distribution on the translocation of an inhomogeneously charged polymer through a nanopore. *Journal of Chemical Physics 128*, 12 (2008), 125104.

[38] Kafri, Yariv, Lubensky, David K., and Nelson, David R. Dynamics of molecular motors and polymer translocation with sequence heterogeneity. *Biophysical Journal 86* (2004), 3373–3391.

[39] Luo, Kaifu, Ala-Nissila, Tapio, Ying, See-Chen, and Bhattacharya, Aniket. Sequence dependence of DNA translocation through a nanopore. *Physical Review Letters 100*, 5 (2008), 058101.

[40] Gauthier, Michael G., and Slater, Gary W. A monte carlo algorithm to study polymer translocation through nanopores. i. theory and numerical approach. *Journal of Chemical Physics 128* (2008), 065103.

[41] Gauthier, Michael G., and Slater, Gary W. A monte carlo algorithm to study polymer translocation through nanopores. ii. scaling laws. *Journal of Chemical Physics 128* (2008), 205103.

[42] Gauthier, Michael G., and Slater, Gary W. Sequence effects on the forced translocation of heteropolymers through a small channel. *Journal of Chemical Physics 128* (2008), 175103.

[43] Keyser, Ulrich F. Controlling molecular transport through nanopores. *Journal of the Royal Society: Interface 8*, 63 (2011), 1369–1378.

[44] Wanunu, Meni, and Meller, Amit. Chemically modified solid-state nanopores. *Nanoletters 7*, 6 (2007), 1580–1585.

[45] Iqbal, Samir M., Akin, Demir, and Bashir, Rashid. Solid-state nanopore channels with DNA selectivity. *Nature Nanotechnology 2* (2007), 243–248.

[46] Kasianowicz, John J., Robertson, Joseph W.F., Chan, Elaine R., Reiner, Joseph E., and Stanford, Vincent M. Nanoscopic porous sensors. *Annual Review Analytic Chemistry 1* (2008), 737–766.

[47] Sanchez-Quesada, Jorge, Saghatelian, Alan, Cheley, Stephen, Bayley, Hagan, and Ghadiri, M. Reza. Single DNA rotaxanes of a transmembrane pore protein. *Angewante Chemie 43* (2004), 3063 – 3067.

[48] Dudko, Olga K., Mathe, Jerome, Szabo, Attila, Meller, Amit, and Hummer, Gerhard. Extracting kinetics from single-molecule force spectroscopy: Nanopore unzipping of DNA hairpins. *Biophysical Journal 92*, 12 (2007), 4188–4195.

[49] Mathe, Jerome, Visram, Hasina, Viasnoff, Virgile, Rabin, Yitzhak, and Meller, Amit. Nanopore unzipping of individual DNA hairpin molecules. *Biophysical Journal 87* (2004), 3205–3212.

[50] Muthukumar, M. Translocation of a confined polymer through a hole. *Physical Review Letters 86*, 14 (2001).

[51] Eisenriegler, Erich. *Polymers Near Surfaces*. World Scientific, 1993.

[52] Gardiner, Crispin W. *Handbook of Stochastic Methods*. Springer-Verlag, 1983.

[53] Henrickson, Sarah E., Misakian, Martin, Robertson, Baldwin, and Kasianowicz, John J. Driven DNA transport into an asymmetric nanometer-scale pore. *Physical Review Letters 85*, 14 (2000), 3057–3060.

[54] Lectures, Nobel. *Physiology or Medicine, 1901-1921*. Elsevier Publishing Company, Amsterdam, 1967.

[55] Marsh, Mark, Ed. *Endocytosis*. Oxford University Press, 2001.

[56] Pastan, I., and Willingham, M.C., Eds. *Endocytosis*. Plenum Press, New York, N.Y., 1985.

[57] Alberts, B. *Molecular Biology of the Cell*. Garland Science, New York, N.Y., 2008.

[58] Marsh, Mark. The entry of enveloped viruses into cells by endocytosis. *Biochemical Journal 218* (1984), 1–10.

[59] Smith, Alicia E., and Helenius, Ari. How viruses enter animal cells. *Science 304* (2004), 237–242.

[60] Deserno, Markus, and Gelbart, William M. Adhesion and wrapping in colloid-vesicle complexes. *Journal of Physical Chemistry B 106* (2002), 5543–5552.

[61] Deserno, Markus. Elastic deformation of a fluid membrane upon colloid binding. *Physical Review E 69* (2004), 031903.

[62] Herant, Marc, Heinrich, Volkmar, and Dembo, Micah. Mechanics of neutrophil phagocytosis: behavior of the cortical tension. *Journal of Cell Science 118* (2005).

[63] Herant, Mar, Heinrich, Volkmar, and Dembo, Micah. Mechanics of neutrophil phagocytosis: experiments and quantitative models. *Journal of Cell Science 119* (2006), 1903–1913.

[64] Gao, Huajian, Shi, Wendong, and Freund, Lambert B. Mechanics of receptor-mediated endocytosis. *Proceedings of the National Academy of Science 102*, 27 (2005), 9469–9474.

[65] Dietrich, Christian, Angelova, Miglena, and Pouligny, Bernard. Adhesion of latex spheres to giant phospholipid vesicles. *Journal de Physique II France 7*, 11 (1997), 1651–1682.

[66] Li, Xinlei, and Xing, Da. A simple method to evaluate the optimal size of nanoparticles for endocytosis based on kinetic diffusion of receptors. *Applied Physics Letters 97* (2010), 153704.

[67] Shan, Yuping, Ma, Suyong, Nie, Liya, Shang, Xin, and Hao, Xian. Size-dependent endocytosis of single gold nanoparticles. *Chemical Communications 47* (2011), 8091–8093.

[68] Chithrani, B. Devika, and Chan, Warren C.W. Elucidating the mechanism of cellular uptake and removal of protein-coated gold nanoparticles of different sizes and shapes. *Nanoletters 7*, 6 (2007), 1542–1550.

[69] Chithrani, Devika B., Dunne, Michael, Steward, James, Allen, Christine, and Jaffray, David A. Cellular uptake and transport of gold nanoparticles incorporated in a liposomal carrier. *Nanomedicine: NBM 6* (2010), 161–169.

[70] Yuan, Hongyan, Li, Ju, Bao, Gang, and Zhang, Sulin. Variable nanoparticle-cell adhesion strength regulates cellular uptake. *Physical Review Letters 105* (2010), 138101.

[71] Bareford, L.M., and Swaan, P.W. Endocytotic mechanisms for targeted drug delivery. *Advanced Drug Delivery Reviews 59*, 8 (2007), 748–758.

[72] Quian, Z.M., Li, H., Sun, H., and Ho, K. Targeted drug delivery via transferrin-receptor mediated pathway. *Pharmocological Review 54*, 4 (2002), 561–587.

[73] Zhang, Sulin, Li, Ju, Lykotrafitis, George, Bao, Gang, and Suresh, Subra. Size-dependent endocytosis of nanoparticles. *Advanced Materials 21* (2009), 419–424.

[74] Ziello, J., Huang, Y., and Jovin, I.S. Cellular endocytosis and gene delivery. *Molecular Medicine 16* (2010), 22–29.

[75] Korobko, A.V., Backendorf, c., and van der Maarel, J.R.C. Plasmid DNA encapsulation within cationic diblock copolymer vesicles for gene delivery. *Journal of Physical Chemistry B 110* (2006), 14550–14556.

[76] Korobko, A.V., Jesse, W., and van der Maarl, J.R.C. Encapsulation of DNA by cationic diblock copolymer vesicles. *Langmuir 21* (2005), 34–42.

[77] Smith, Kurt A., Jasnow, David, and Balazs, Anna C. Designing synthetic vesicles that engulf nanoscopic particles. *Journal of Chemical Physics 127* (2007), 084703.

[78] Peyratout, Claire S., and D$'$ahne, Lars. Tailor-made polyelectrolyte microcapsules: from multilayers to smart containers. *Angewante Chemie 43* (2004), 3762–3783.

[79] Gao, Changyou, Leporatti, Stefano, Moya, Sergio, Donath, Edwin, and Ḿohwald. Stability and mechanical properties of polyelectrolyte capsules obtained by stepwise assembly of poly(styrenesulfonate sodium salt) and poly(diallyldimethyl ammonium) chloride onto melamine resin particles. *Langmuir 17* (2001), 3491–3495.

[80] Antipov, Alexei A., and Sukhorukov, Gleb B. Polyelectrolyte multilayer capsules as vehicles with tunable permeability. *Advances in Colloid and Interface Science 111* (2004), 49–61.

[81] Gómez-Hens, Agustina, and Fernández-Romero, Juan Manuel. The role of liposomes in analytical processes. *Trends in Analytical Chemistry 24*, 1 (2005), 9–19.

[82] Vreeland, Wyatt N., and Locascio, Laurie E. Using bioinspired thermally triggered liposomes for high-efficiency mixing and reagent delivery in microfluidic devices. *Analytical Chemistry 75* (2003), 6906–6911.

[83] Karlsson, Anders, Karlsson, Mattias, Karlsson, Roger, Kristin, Sott, Lundqvist, Anders, Tokarz, Michal, and Orwar, Owe. Nanofluidic networks based on surfactant membrane technology. *Analytical Chemistry 75* (2003), 2529–2537.

[84] Hong, Jong Wook, and Quake, Stephen R. Integrated nanoliter systems. *Nature: Biotechnology 21*, 10 (2003), 1179–1183.

[85] Tan, Yung-Chieh, Hettiarachchi, Kanaka, Siu, Maria, Pan, Yen-Ru, and Lee, Abraham Phillip. Controlled microfluidic encapsulation of cells, proteins, and microbeads in lipid vesicles. *Journal of the American Chemical Society 128* (2006), 5656–5658.

[86] Lee, Eunice S., Robinson, David, Rognlien, Judith L., Harnett, Cindy K., Simmons, Blake A., Ellis, C.R. Bowe, and Davalos, Rafael V. Microfluidic electroporation of robust 10-μm vesicles for manipulation of picoliter volumes. *Bioelectrochemistry 69* (2006), 117–125.

[87] Jin, Hong, Heller, Daniel A., and Strano, Michael S. Single-particle tracking of endocytosis and exocytosis of single-walled carbon nanotubes in NIH-3T3 cells. *Nanoletters 8*, 6 (2008), 1577–1585.

[88] Wang, Jiafang, and Muthukumar, Murugappan. Encapsulation of a polyelectrolyte chain by an oppositely charged spherical surface. *Journal of Chemical Physics 135* (2011), 194901.

[89] Seifert, Udo. Configurations of fluid membranes and vesicles. *Advances in Physics 46*, 1 (1997), 13–137.

[90] Helfrich, W. Elastic properties of lipid bilayers: Theory and possible experiments. *Zeitschrift fur Naturforschung 28* (1973), 693–703.

[91] Willmore, T.J. *An Introduction to Differential Geometry.* Oxford University Press, New York, N.Y., 1959.

[92] Tu, Z.C., and Ou-Yang, Z.C. A geometric theory on the elasticity of biomembranes. *Journal of Physics A: Mathematical and General 37* (2004), 11407–11429.

[93] Lifshitz, E.M., and Pitaevskii, L.P. *Physical Kinetics.* Pergamon, 1989.

[94] Marsh, Derek. Elastic curvature constants of lipid monolayers and bilayers. *Chemistry and Physics of Lipids 144* (2006), 146–159.

[95] Freundlich, H., and Seifriz, W. Ueber die elastizitt von solen und gelen. *Zeitschrift furphysikalische chemie 104* (1922), 233.

[96] Heilbronn, A. Eine neue methode zur bestimmung der viskositt lebenderprotoplasten. *Jahrbuch der Wissenschaftlichen Botanik 61* (1922), 284–338.

[97] Crick, F., and Hughes, A. The physical properties of the cytoplasm. *Experimental Cell Research 1* (1950), 37–80.

[98] Yagi, K. The mechanical and colloidal properties of amoeba protoplasm and their relations to the mechanism of amoeboid movement. *Comparative Biochemistry and Physiology 3* (1961), 73–91.

[99] Hiramoto, Y. Mechanical properties of the protoplasm of the sea urchin egg. *Experimental Cell Research 56* (1971), 201–218.

[100] King, M., and Macklam, P.T. Rheological properties of microliter quantities of normal mucus. *Journal of Applied Physiology 42* (1977), 797–802.

[101] Waigh, T. A. Microrheology of complex fluids. *Reports on Progress in Physics 68* (2005), 685–742.

[102] Helfer, E., Harlepp, S., Bourdieu, L., Robert, J., MacKintosh, F. C., and Chatenay, D. Microrheology of biopolymer-membrane complexes. *Physical Review Letters 85*, 2 (2000), 457–460.

[103] Gittes, F., and MacKintosh, F. C. Dynamic shear modulus of a semiflexible polymer network. *Physical Review E 58*, 2 (1998), R1241 – R1244.

[104] Bausch, Andreas R., Möller, Winfried, and Sackmann, Erich. Measurement of local viscoelasticity and forces in living cells by magnetic tweezers. *Biophysical Journal 76* (1999), 573–576.

[105] MacKintosh, F. C., and Schmidt, C. F. Microrheology. *Current Opinion in Colloid & Interface Science 4* (1999), 300–307.

[106] Mason, T. G., and Weitz, D. A. Optical measurements of frequency-dependent linear viscoelastic moduli of complex fluids. *Physical Review Letters 74*, 7 (1995), 1250–1253.

[107] Levine, Alex J., and Lubensky, T. C. Response function of a sphere in a viscoelastic two-fluid medium. *Physical Review E 63* (2001), 041510.

[108] Giannelis, Emmanuel P. Polymer layered silicate nanocomposites. *Advanced Materials 8*, 1 (1996), 29–35.

[109] Alexandre, Michael, and Dubois, Philippe. Polymer-layered silicate nanocomposites: preparation, properties and uses of a new class of materials. *Materials Science and Engineering: R:Reports 28*, 1-2 (2000), 1–63.

[110] Thanpitcha, Tuspon, Li, Zheng, Rujiravanit, Ratana, Sirivat, Anuvat, and Jamieson, Alexander M. Anomalous rheology of polypyrrole nanoparticle/alginate suspensions: effect of solids volume fraction, particle size and electronic state. *Rheologica Acta 50*, 9-10 (2011), 809–823.

[111] Anderson, Benjamin J., and Zukoski, Charles F. Rheology and microstructure of entangled polymer nanocomposite melts. *Macromolecules 42* (2009), 8370–8384.

[112] Anderson, Benjamin J., and Zukoski, Charles F. Rheology and microstructure of polymer nanocomposite melts: variation of polymer segment-surface interaction. *Langmuir 26*, 11 (2010), 8709–8720.

[113] Hooper, Justin B., and Schweizer, Kenneth S. Contact aggregation, bridging, and steric stabilization in dense polymer-particle mixtures. *Macromolecules 38* (2005), 8858–8869.

[114] Hooper, J.B., and Schweizer, K.S. Structure, surface excess and effective interactions in polymer nanocomposite melts and concentrated solutions. *Journal of Chemical Physics 121*, 14 (2004), 6986–6997.

[115] Lakes, R.S., Katz, J.L., and Sternstein, S.S. Viscoelastic properties of wet cortical bone: Part i, torsional and biaxial studies. *Journal of Biomechanics 12* (1979), 657–678.

[116] Lakes, R.S., and Katz, J.L. Viscoelastic properties of wet cortical bone: Part ii, relaxation mechanisms. *Journal of Biomechanics 12* (1979), 679–687.

[117] Hashin, Z., and Shtrikman, S. On some variational principles in anisotropic and nonhomogeneous elasticity. *Journal of Mechanics and Physics of Solids 10* (1995), 335.

[118] Hashin, Z., and Shtrikman, S. A variational approach to the theory of the elastic behaviour of multiphase materials. *Journal of Mechanics and Physics of Solids 11* (1963), 127.

[119] Mori, T., and Tanaka, K. Average stress in matrix and average elastic energy of materials with misfitting inclusions. *Acta Metallurgica 21* (1973), 571.

[120] Brinson, L.C., and Lin, W.S. Comparison of micromechanics methods for effective properties of multiphase viscoelastic composites. *Composite Structures 41* (1998), 353–367.

[121] Tanaka, Toyoichi, Hocker, Lon O., and Benedek, George B. Spectrum of light scattered from a viscoelastic gel. *Journal of Chemical Physics 59*, 9 (1973), 5151–5159.

[122] Mondescu, Radu, and Muthukumar, M. Dynamics of diblock copolymers in dilute solutions. *Macromolecules 30*, 20 (1997), 6358–6368.

[123] Jackson, John David. *Classical Electrodynamics.* John Wiley & Sons, Inc., 1999.

[124] Mondescu, R. P., and Muthukumar, M. Effective elastic moduli of a composite containing rigid spheres at nondilute concentrations: A multiple scattering approach. *Journal of Chemical Physics 110*, 2 (1999), 1123–1137.

[125] Schnurr, B., Gittes, F., MacKintosh, F. C., and Schmidt, C. F. Determining microscopic viscoelasticity in flexible and semiflexible polymer networks from thermal fluctuations. *Macromolecules 30* (1997), 7781–7792.

[126] Freed, Karl F., and Muthukumar, M. Dynamics and hydrodynamics of suspensions of translational-rotational brownian particles at finite concentrations. *Journal of Chemical Physics 69*, 6 (1978), 2657–2671.

[127] Muthukumar, M., and Freed, Karl F. On the stokes problem for a suspension of spheres at nonzero concentrations. ii. calculations for effective medium theory. *Journal of Chemical Physics 70*, 12 (1979), 5875–5887.

[128] Nusser, Klaus, Schneider, Gerald J., Pyckhout-Hintzen, Wim, and Richter, Dieter. Viscosity decrease and reinforcement in polymer-silsesquioxane composites. *Macromolecules 44*, 19 (2011), 7820–7830.

[129] Torquato, S., and Stell, G. Microstructure of two-phase random media. v. the n-point matrix probability functions for impenetrable spheres. *Journal of Chemical Physics 82*, 2 (1985), 980–987.

[130] Quintanilla, J., and Torquato, S. New bounds on the elastic moduli of suspensions of spheres. *Journal of Applied Physics 77*, 9 (1995), 4361–4372.

[131] Torquato, S. Statistical description of microstructures. *Annual Review of Materials Research 32* (2002), 77–111.

[132] Torquato, S. Bulk properties of two-phase disordered media. iii. new bounds on the effective conductivity of dispersions of penetrable spheres. *Journal of Chemical Physics 84*, 11 (1986), 6345–6359.

[133] Gibiansky, L.V., and Lakes, R. Bounds on the complex bulk and shear moduli of a two-dimensional two-phase viscoelastic composite. *Mechanics of Materials 25* (1997), 79–95.

[134] Ricaud, Jean-Marc, and Masson, Renaud. Effective properties of linear viscoelastic heterogeneous media: Internal variables formulation and extension to ageing behaviors. *International Journal of Solids and Structures 46* (2009), 1599–1606.

[135] Kutvonen, Aki, Rossi, Giulia, and Ala-Nissila, Tapio. Correlations between mechanical, structural, and dynamical properties of polymer nanocomposites. *Physical Review E 85* (2012), 041803.

[136] Sternstein, S.S., and un Zhu, Ai-J. Reinforcement mechanism of nanofilled polymer melts as elucidated by nonlinear viscoelastic behavior. *Macromolecules 35* (2002), 7262–7273.